Maria Ana Dias de Almeida Francisco Caranova

Structural connectivity as a potential biomarker in multiple sclerosis using MRI

VOLUME 1

Dissertação no âmbito do Mestrado em Engenharia Biomédica orientada pelo Doutor João Valente Duarte e pelo Professor Doutor Miguel de Sá e Sousa de Castelo Branco e apresentada ao Departamento de Física da Faculdade de Ciências e Tecnologias da Universidade de Coimbra

junho de 2022

Agradecimentos

Em primeiro lugar, gostaria de deixar o meu agradecimento a toda a equipa que me acolheu. Ao Professor Doutor Miguel Castelo Branco, obrigada pela oportunidade e pelo exemplo que demonstrou ser no empenho e rigor; ao Doutor João Duarte, obrigada pela confiança, palavras de incentivo, partilha de conhecimentos, e por todas as oportunidades; à Júlia, obrigada por toda a ajuda, aconselhamento e disponibilidade.

Às minhas amigas: Andreia, obrigada por estares comigo desde sempre, e por ouvires tudo, mesmo quando não percebes nada; Marta, obrigada por todas as *movie* e *game* nights, por todos os jogos de FIFA (que um dia hei de ganhar), e por teres tornado Coimbra uma aventura divertida; Joana, obrigada por todas as conversas sobre livros, por me acompanhares em devaneios e por seres uma companhia constante; Sofia (ou Beatriz), obrigada por teres sido a primeira e me teres feito sentir em casa em Coimbra, por todos os conselhos e gargalhadas.

Ao Samuel, obrigada por acreditares em mim, mesmo quando não sabia que era preciso; o teu apoio e motivação constantes foram imprescindíveis para chegar ao fim deste percurso e ainda querer continuar.

Por fim, não há palavras que cheguem para agradecer a quem impulsionou todo este caminho e que me ensinou (quase) tudo o que sei. Mãe, sempre foste e és um exemplo de resiliência, luta e determinação. Quando for grande quero ser como tu.

"Question everything. Your love, your religion, your passion.

If you don't have questions, you'll never find answers."

Colleen Hoover

Resumo

A Esclerose Múltipla (EM) é a doença mais comum da matéria branca do sistema nervoso central nos humanos. É caracterizada por lesões onde ocorre desmielinização e por um estado inflamatório permanente; estas condições podem estar acompanhadas de atrofia quer da matéria cinzenta, quer da matéria branca. O *gold standard* para o diagnóstico e monitorização da EM é a Imagiologia por Ressonância Magnética estrutural (IRM); no entanto, esta é uma técnica à qual faltam sensibilidade e especificidade para a identificação dos processos patológicos em EM. Portanto, técnicas de IRM não convencionais, como a Imagiologia por Ressonância Magnética de Difusão (IRM de difusão) podem contribuir para a compreensão de alterações a um nível microestrutural.

A Imagiologia por Tensor de Difusão (em inglês, *Diffusion-Tensor Imaging,* ou DTI) é uma técnica que modela dados de IRM de difusão e que já existe há muitos anos. É amplamente usada quer em modelos de investigação quer na prática clínica, tanto pela sua simplicidade como pela sua facilidade de uso. No entanto, a DTI não apresenta uma especificidade suficiente para permitir a distinção de processos patológicos como desmielinização e perda axonal a um nível microestrutural. Assim, ferramentas inovadoras como a Imagiologia por Dispersão da Orientação e Densidade de Neurites (em inglês, *Neurite Orientation Dispersion and Density Imaging,* ou NODDI) foram desenvolvidas para colmatar algumas falhas da DTI. O uso do modelo de NODDI permite a diferenciação entre perda dendrítica e axonal e redução na arborização dendrítica ou aumento dos processos de dispersão, que são mecanismos que integram um único parâmetro em DTI.

Esta tese de mestrado pretende investigar diferenças a nível dos vóxeis (*voxel-wise*) em parâmetros derivados quer de DTI quer de NODDI, em doentes de EM e controlos saudáveis emparelhados demograficamente; para além disto, também foram consideradas médias de métricas de difusão em tecidos de interesse (matéria branca, matéria branca aparentemente normal e lesões, no cérebro) para investigar as diferenças entre grupos. Por fim, foram feitas correlações entre as métricas de DTI e NODDI e testes cognitivos e neuropsicológicos para avaliar o efeito das alterações em métricas de difusão na incapacidade cognitiva e física característica em doentes com EM.

A análise *voxel-wise* em DTI e NODDI mostrou diferenças consideráveis entre doentes e controlos saudáveis; isto também foi observado na análise estatística dos valores médios em tecidos de interesse. Estes resultados suportam a noção de que métricas de difusão estão alteradas, mesmo em fases iniciais de EM, e ajudam a perceber quais os

processos patológicos subjacentes à da evolução da doença. Um resultado interessante foi o aumento da densidade de neurites em lesões, que é algo pouco reportado na literatura. Por fim, as correlações entre métricas de difusão e resultados dos testes cognitivos e neuropsicológicos revelaram que tanto os parâmetros obtidos através de DTI como os obtidos a partir de NODDI podem ajudar a explicar a deficiência cognitiva e física em EM.

Para concluir, este trabalho ajudou a provar que a IRM de difusão é uma ferramenta valiosa na avaliação da EM, e os resultados aqui apresentados foram um passo na direção da compreensão de como é que as métricas de difusão estão relacionadas quer com a evolução da doença, quer com a incapacidade observada em EM.

Palavras-chave

Esclerose Múltipla, Imagiologia por Ressonância Magnética, Imagiologia por Ressonância Magnética de Difusão, Imagiologia por Tensor de Difusão, Imagiologia por Dispersão da Orientação e Densidade de Neurites

Abstract

Multiple Sclerosis (MS) is the most common white matter (WM) disease. It is characterised by demyelinating lesions, and a permanent inflammatory state; these can be accompanied by both grey and white matter atrophy and neurodegeneration. The gold standard in diagnosing and monitoring MS is the structural Magnetic Resonance Imaging (MRI), which has been proven as a technique that lacks specificity and sensitivity for MS pathological processes. Hence, unconventional MRI techniques such as Diffusion-Weighted Imaging (DWI) can aid in giving clues to understand what is happening at a microstructural level.

Diffusion Tensor Imaging (DTI) is a technique used to model DWI data that has been around for many years. It is widely used in both research and clinical routine, due to its simplicity and ease of use. However, DTI is not always adequate to analyse this type of data since it does not have enough specificity to distinguish pathological processes such as demyelination and axonal loss at a microstructural level. Consequently, novel tools such as Neurite Orientation Dispersion and Density Imaging (NODDI) have been developed to tackle DTI's flaws. NODDI allows to distinguish axonal and dendritic loss from reduced dendritic arborisation and increase in sprawling processes, which are mechanisms that are accounted for in a single parameter in DTI.

This master thesis attempts to investigate voxel-wise differences in DTI and NODDI-derived parameters, in MS patients and matched healthy controls; average diffusion metrics in tissues of interest (WM, normal appearing WM and lesions of the brain) were also considered, to further assess differences between groups. DTI and NODDI metrics were then correlated with cognitive and neuropsychological tests, in anatomical regions of interest, to evaluate the effect of alterations in diffusion metrics in cognitive and physical disability in MS patients.

Both DTI and NODDI voxel-wise analysis showed considerable discrepancies between MS patients and healthy controls; this was also seen in the statistical analysis of mean values in tissues of interest. These results support the notion that diffusion metrics are altered, even in early MS, and help to understand its underlying pathological mechanisms. An intriguing result was the increased average neurite density found in lesions, which, to our knowledge, has only been reported in one study. Finally, correlations between diffusion metrics and cognitive and neuropsychological scores showed that both

DTI and NODDI-derived parameters can help to explain cognitive and physical impairment in MS.

In conclusion, this work helped to prove that DWI is a valuable tool in the evaluation of MS, and its results gave a few steps into better understanding how diffusion metrics are related to MS evolution and disability.

Keywords

Multiple Sclerosis, Magnetic Resonance Imaging, Diffusion-Weighted Imaging, Diffusion Tensor Imaging, Neurite Orientation Dispersion and Density Imaging

Contents/Index

List of tables

List of figures

List of equations

Abbreviations

5tt – 5 tissue-type

ACT – Anatomical Constrained Tractography

AD – Axial Diffusivity

ADC – Apparent Diffusion Coefficient

BS - Brain Stem

BVMT – Brief Visuospatial Memory Test

CIS – Clinically Isolated Syndrome

CNS – Central Nervous System

CNT – Healthy Controls

CSF – Cerebrospinal Fluid

CVLIV - Cerebellar Vermal Lobules I-V

CVLT – California Verbal Learning Test

CVLVIVII – Cerebellar Vermal Lobules VI-VII

DT – Diffusion Tensor

DTI – Diffusion Tensor Imaging

DWI – Diffusion-weighted Imaging

EDSS - Expanded Disability Status Scale

EPI – Echo-planar Imaging

FA – Fractional Anisotropy

FDR – False Discovery Rate

FLAIR – Fluid-attenuated inversion-recovery

FOV – Field of View

GM – Grey Matter

HARDI – High Angular Resolution Diffusion Imaging

LACG – Left Anterior Cingulate Gyrus

LAG - Left Angular Gyrus

LAIns – Left Anterior Insula

LAm – Left Amygdala

LC - Left Caudate

LCC - Left Calcarine Cortex

LCE - Left Cerebellum Exterior

LCO - Left Central Operculum

LCumWM - Left Cerebellum White Matter

LCWM – Left Cerebral White Matter

LEA - Left Entorhinal Area

LFG - Left Fusiform Gyrus

LFO - Left Frontal Operculum

LFP - Left Frontal Pole

LGR – Left Gyrus Rectus

LLG – Left Lingual Gyrus

LLOG - Left Lateral Orbital Gyrus

LLV - Left Lateral Ventricle

LMCG – Left Middle Cingulate Gyrus

LMFC - Left Medial Frontal Cortex

LMFG – Left Middle Frontal Gyrus

LMOrG - Left Medial Orbital Gyrus

LMTG – Left Middle Temporal Gyrus

LOPOFIFG – Left Opercular Part OF the Inferior Frontal Gyrus

LOrPOFIFG - Left Orbital Part of the Inferior Frontal Gyrus

LP – Left Pallidum

LPCG - Left Posterior Cingulate Gyrus

LPG - Left Postcentral Gyrus

LPhG - Left Parahippocampal Gyrus

LPIns – Left Posterior Insula

LPOrG - Left Posterior Orbital Gyrus

LPP – Left Planum Polare

LPreG – Left Precentral Gyrus

LPT - Left Planum Temporale

LPu – Left Putamen

LSA - Left Subcallosal Area

LSFGMS – Left Superior Frontal Gyrus Medial Segment

LSMC – Left Supplementary Motor Cortex

LSPL – Left Superior Parietal Lobule

LSTG – Left Superior Frontal Gyrus

LTmP - Left Temporal Pole

LTP - Left Thalamus Proper

LVDC – Left Ventral Diencephalon

MD – Mean Diffusivity

MFIS - Modified Fatigue Impact Scale

MRI – Magnetic Resonance Imaging

MS – Multiple Sclerosis

MSC – Multiple Sclerosis patients

NABT – Normal Appearing Brain Tissue

NAWM – Normal Appearing White Matter

NDI – Neurite Density Index

NMR – Nuclear Magnetic Resonance

NODDI – Neurite Orientation Dispersion and Density Imaging

OC - Optic Chiasm

ODI – Orientation Dispersion Index

PPMS – Primary Progressive Multiple Sclerosis

PRMS – Progressive-Relapsing Multiple Sclerosis

RAA – Right Accumbens Area

RACG – Right Anterior Cingulate Gyrus

RAG – Right Angular Gyrus

RAIns - Right Anterior Insula

RAm – Right Amygdala

RAOG - Right Anterior Orbital Gyrus

RBF - Right Basal Forebrain

RC - Right Caudate

RCE - Right Cerebellum Exterior

RCO - Right Central Operculum

RCumWM - Right Cerebellum White Matter

RCWM – Right Cerebral White Matter

RD – Radial Diffusivity

RF – Radiofrequency

RFG - Right Fusiform Gyrus

RFO – Right Frontal Operculum

RH – Right Hippocampus

RIS – Radiologically Isolated Syndrome

RITG – Right Inferior Temporal Gyrus

RLG - Right Lingual Gyrus

RLV – Right Lateral Ventricle

RME – Reading the Mind in the Eyes

RMFG – Right Middle Frontal Gyrus

RMOG – Right Middle Occipital Gyrus

RMTG – Right Middle Temporal Gyrus

ROFG - Right Occipital Fusiform Gyrus

ROI – Region of Interest

ROPOFIFG – Right Opercular Part OF the Inferior Frontal Gyrus

RP – Right Pallidum

RPG – Right Postcentral Gyrus

RPhG - Right Parahippocampal Gyrus

RPIns - Right Posterior Insula

RPOrG - Right Posterior Orbital Gyrus

RPP - Right Planum Polare

RPreG – Right Precentral Gyrus

RPT - Right Planum Temporale

RPu – Right Putamen

RRMS – Relapsing-Remitting Multiple Sclerosis

RSFG – Right Superior Frontal Gyrus

RSFGMS – Right Superior Frontal Gyrus Medial Segment

RSG – Right Supramarginal Gyrus

RSMC – Right Supplementary Motor Cortex

RSTG - Right Superior Temporal Gyrus

RTP - Right Thalamus Proper

RTTG - Right Transverse Temporal Gyrus

RVDC – Right Ventral Diencephalon

SDMT – Simplified Digit Modalities Test

SIFT - Spherical-deconvolution Information Filtering

SPM – Statistical Parametric Mapping

SPMS – Secondary Progressive Multiple Sclerosis

T1-DWI – T1-image in Diffusion Space

TBSS – Tract-Based Spatial Statistics

TE – Echo Time

TFCE - Threshold-Free Cluster Enhanced

thirdV - Third Ventricle

TIV – Total Intracranial Volume

TR – Repetition Time

WM – White Matter

1. Introduction

1.1. Motivation

Multiple Sclerosis (MS) is an autoimmune, inflammatory, and neurological disease that targets the Central Nervous System (CNS), being characterised by the destruction of both myelin and axons, leading to neurodegeneration and neurologic disability in several domains, such as the visual, motor, and cognitive, with a degree that depends on the disease's phenotype (Enzinger & Fazekas, 2015; Goldenberg, 2012).

MS is one of the world's most common white matter diseases, affecting approximately 2.8 million people in the whole world, with a worldwide prevalence of about 35.9 in 100000 people (2020 data), and women are twice more likely to be diagnosed with MS than men. In fact, it is estimated that a diagnosis of MS is made every five minutes (Walton et al., 2020).

The aetiology of this disease is not well established, but it may be due to genetic susceptibility, and then triggered by environmental factors such as a virus (particularly the Epstein-Barr virus) or others (for example, low vitamin D levels) (Goldenberg, 2012). Most patients are diagnosed in early stages of their life (between 20 and 40 years of age) (Garg & Smith, 2015; Klineova & Lublin, 2018; Oh et al., 2018), when they are usually the most productive and starting families; this will impact their quality of life, their families and society in general. There are treatments that can aid in the reduction of disability and in the increase of life expectancy in MS patients, but a cure is yet to be found, as is its precise aetiology (Walton et al., 2020).

Studies have already shown that a prompt treatment upon diagnosis slows down the progression of the disease, reduces disability, extends lifetime expectancy, which is decreased by approximately ten years in MS (Oh et al., 2018), and overall provides a better quality of life. Magnetic Resonance Imaging (MRI) has become the most important imaging tool when diagnosing and monitoring MS. In clinical environments, conventional MRI such as anatomical T1 and T2-weighted sequences are the most widely used; however, these techniques fail to show the full extent of the processes underlying the establishment and progression of MS and lack specificity. Thus, unconventional techniques such as Diffusion-Weighted Imaging (DWI) have risen to try and overcome these obstacles. Using Diffusion Tensor Imaging (DTI) and Neurite Orientation Dispersion and Density Imaging (NODDI) as ways to model DWI data, it is possible to identify subtle microstructural differences

between both normal appearing brain tissue (NABT) and lesions, and normal brain tissues. It is also possible to establish relationships between variations in meaningful diffusion metrics and cognitive dysfunction and disability progression (Enzinger et al., 2015). Developing such imaging biomarkers is crucial to reliably assess disease progression to better adjust interventions.

1.2. Proposed Approach

This work's focus is to understand how water diffusion properties in the brain are altered in MS patients and interpret them considering their biological meaning and their role in structural connectivity. Hence, the proposed approach is to extract DWI metrics by modelling data with DTI and NODDI, analyse how they differ between early MS patients and age and gender-matched healthy controls, and finally to correlate them with cognitive and neuropsychological assessments.

A 3T MRI system was used to obtain the DWI data, with a multi-shell protocol and three b-values, which allowed the use of both NODDI and DTI models of DWI. Structural data was also acquired on the same session to better localise microstructural diffusion differences and to determine lesions' locations, namely a T1-weighted MP2RAGE and a T2-weighted FLAIR image. Using voxel-wise statistical analysis, the differences between groups were assessed, in tissues of interest such as the normal appearing white matter and MS lesions. Lastly, neuropsychological evaluation of the MS patients provided measures for cognitive and neuropsychological scores that were correlated with NODDI and DTI metrics, in different anatomical regions of the brain and in tissues of interest.

This approach allowed to understand how diffusion is altered even in early MS, and how that could be a clue as to whether this variation is in lesioned tissue or in apparently normal tissue, where there are no visible lesions on standard structural images. Water diffusion properties further provide information on structural connectivity, and how its disruption is linked to microstructural changes.

1.3. Objectives and Original Contributions

Studies in this field often focus on conventional DWI models, such as DTI. NODDI is a relatively recent technique that lately has been receiving attention for its ability to discern microstructural alterations not sensed by DTI. Coupling that with the fact that DTI is an extremely simple model relying on assumptions that often do not correspond to the reality of water displacement in the brain, and that it has serious limitations, it led to the objective

of employing NODDI as a tool to overcome these problems in DWI data processing. Still, DTI remains important, since, as a simple model, is widely used in both research and clinical environments and provides sufficient information for initial suggestions on demyelination and other MS progression processes. Thus, this thesis also set to compare DTI and NODDI metrics extracted from the same data in MS patients. Furthermore, the statistical analysis is usually based on regions of interest and/or tract-based analysis. Few studies report voxel-wise statistical analysis with as much detail as the one presented here (Spano et al., 2018), and not in the same conditions.

Most of the studies reported until today use data from MS patients with a long disease duration or use small cohorts of patients (By et al., 2017; Chen et al., 2021; Collorone et al., 2020; Hagiwara et al., 2019; Mustafi et al., 2019; Schneider et al., 2017; Spano et al., 2018). There is a lack of studies investigating changes in early MS, since even the results reported for shorter disease durations (de Santis et al., 2019; Granberg et al., 2017) still are not for MS patients with a diagnosis as recent as the ones who participated in this work.

Knowing all of what was described above, this thesis' objectives can be summarised in the following: i) extract DTI and NODDI parameters from two different groups (recently diagnosed MS patients and matched healthy controls); ii) analyse voxel-wise differences between groups in tissues of interest and in the whole brain; iii) analyse differences in average values of the parameters in tissues of interest, between groups; iv) correlate the extracted microstructural metrics in regions of interest defined in an anatomical atlas and in tissues of interest (normal appearing white matter (NAWM) and MS lesions) with previously defined neuropsychological and cognitive scores.

This thesis describes my contributions in this work, ranging from data acquisition, to processing and analysing the collected data by using and integrating different softwares into customised processing and analysis pipelines, which were optimised and adapted to the objectives of the thesis, to interpretation and discussion of the results.

This thesis was integrated in the project "Biomuscle", supported by Fundação para a Ciência e Tecnologia, with reference PTDC/MEC-NEU/31973/2017.

1.4. Thesis Outline

This thesis has seven main sections (Introduction, Background and Literature Review, Methods, Results, Discussion, Limitations and Conclusion). The first section is intended to give a brief introduction of the topic and the work. The second has the objective

of explaining the foundations of this work, what has been done so far in this field, and the principles of each technique that was considered of importance for this thesis. The third section presents the methods used in this work (participants, MRI acquisition, analysis of DWI data), whose results are presented in the fourth section. The fifth section is the one where results are discussed and interpreted in the light of was shown in section two, and in this context. The sixth section addresses the limitations underlying this research, which should be taken into consideration when analysing and interpreting the results. Finally, the seventh section concludes this master's thesis, with the take home messages and suggestions for future work. After these main sections, there is a final section, Annexes, which depicts supplementary figures and tables.

1.5. Thesis Outputs

The work from this master thesis resulted in an abstract submitted to the peer-reviewed international conference of the European Committee for Treatment and Research in Multiple Sclerosis 2022 (ECTRIMS), under the topic 27: MRI & PET, cited below.

Maria Caranova, Júlia Freire Soares, Ana Cláudia Lima, Lívia Sousa, Miguel Castelo-Branco, Sónia Batista, João Valente Duarte (2022). ***Probing brain microstructural connectivity in patients with early Multiple Sclerosis using diffusion weighted MRI***. 38th Congress of European Committee for Treatment and Research in Multiple Sclerosis - ECTRIMS 2022.

2. Background and Literature Review

2.1. Multiple Sclerosis

2.1.1. Pathogenesis

Being a multifocal white matter disease, MS is provoked by degeneration in white matter (WM). The pathogenesis of this disease entails an immune attack against CNS antigens, which is mediated through myelin-reactive T-cells and possibly, B-cells; myelin specific T-cells will cause demyelination, and oligodendrocyte and axonal loss. There is some self-tolerance of the CNS and myelin against autoimmune myelin attacks, which is thought to be lost due to environmental factors, such as a viral infection, leading to demyelination (Garg & Smith, 2015). Demyelination consists in the loss of myelin with preservation of axons, due to damage in myelin sheaths. Axons that have been demyelinated tend to atrophy and degenerate, and thus axonal loss and/or injury is also present in later stages of MS, paving the way to the onset of disability (Love, 2006). Axonal damage can be due to demyelination, but it can also be a concurrent process, and not a consequence, namely in grey matter. In fact, axons can maintain their ability to conduct electric impulses, even after demyelination. Still, long term demyelination leads to axonal injury and even atrophy, as mentioned before (Haines et al., 2011). Although the exact mechanisms of myelin and axonal damage are not completely understood, it is known that T-cells play a major role in the pathogenesis of MS. The attack on CNS leads to the persistent activation of peripheral autoreactive T-cells, which migrate across the blood-brain barrier. Once in the CNS, these T-cells can be reactivated, triggering an inflammatory response that leads to myelin damage; this results in a permanent inflammatory state (Garg & Smith, 2015).

Even though it is not considered as an inherited disease, there is a genetic component linked to susceptibility to MS, since there can be more than one case in the same family; this genetic component is further supported by linkage analysis studies, which have shown that loci such as the major histocompatibility complex HLA DR15/DQ6 allele are risk factors for the development of MS (Garg & Smith, 2015).

The pathological hallmark of MS is its lesions, or plaques, which are focal areas of demyelination with variable degrees of inflammation. The inflammatory infiltrates consist of T-lymphocytes, B-cells, activated macrophages and microglia, and plasma cells. These lesions can be divided into active, chronic or remyelinated. Active lesions are more common

in the relapsing-remitting form of the disease and are characterised as having active demyelination and inflammation. Chronic lesions are associated with the progressive stage of MS and are related to an absence of inflammation and a higher degree of myelin injury. Finally, remyelinated plaques are seen within or at the margins of active lesions and contain myelinated axons; these are common to all stages of MS (Dobson & Giovannoni, 2019; Garg & Smith, 2015). Remyelination is often present in early MS and is driven by the reappearance of oligodendrocytes in active lesions, which will lead to a neuroprotective effect on axons. However, this process is thought to be transient and these remyelinated plaques can be a target for another period of demyelination (Patrikios et al., 2006).

In summary, MS presents multifocal demyelination plaques, mainly in periventricular WM, optic nerves, brainstem, cerebellum, and spinal cord. Besides demyelination, MS may also lead to neurologic disability due to gliosis and axonal damage (Costa Sousa, 2015).

2.1.2. Clinical features

There is no single histological difference between different MS phenotypes; while there have been identified different clinical subtypes of the disease, the pathological changes form a continuum. This means that patients can gradually evolve from one form of MS to another over time, typically years (Dobson & Giovannoni, 2019).

Since myelin damage is the main pathological characteristic of MS, the clinical features of this disease are intrinsically related to demyelination. Because myelin becomes compromised, impulse conduction through the axon is either slowed or stops entirely in regions of demyelination (lesions), resulting in clinical symptoms that depend on the lesions' location (Kocsis et al., 2008). Symptoms of MS include spasticity, sensory disturbances, unilateral numbness, trigeminal neuralgia, optic neuritis, incontinence, constipation, fatigue, and sexual dysfunction (Goldenberg, 2012).

There are four main phenotypes of MS (represented in Fig. 1): relapsing-remitting MS (RRMS), primary progressive MS (PPMS), secondary progressive MS (SPMS), and progressive-relapsing MS (PRMS). The distinction between these forms of MS is based on their manifestations: in RRMS, there is a clear exacerbation of symptoms, followed by a remission period with little increase in disability levels; in PPMS, there is a worsening of the disease since its onset, with the absence of relapses and remission periods; in SPMS, there may or may not exist relapses and remission periods, but there is a progressive worsening of the disease from the beginning; in PRMS, there is progression of the disease from the early stages, with intermittent worsening of symptoms, and no remission periods (Goldenberg, 2012). There can also be identified a subtype of relapsing MS, which is known as benign MS, and it leads to the accumulation of little to no disabilities in patients over time (Filippi & Rocca, 2011).

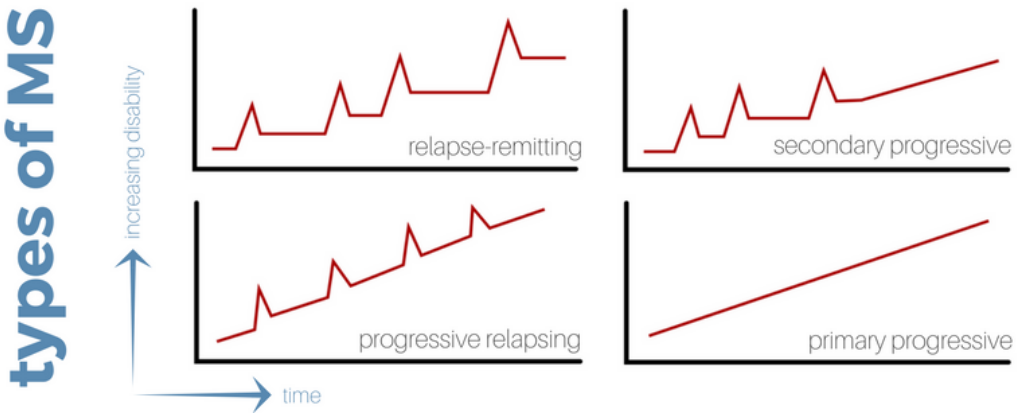

Fig. 1 The four types of MS. Each plateau shows a remission period, while peaks mean outbursts of MS. Note that PPMS shows neither, which is indicative of a progressive disease (Lisa, 2017).

Even though there are well-established MS phenotypes, most of patients with an MS diagnosis present a clinically isolated syndrome (CIS), which can evolve into either RRMS or SPMS, if there is disease progression between relapses. On the other hand, it is also possible to have a radiologically isolated syndrome (RIS), if the patient has lesions on an image but shows no clinical symptoms (Filippi & Rocca, 2011).

The type of MS of a patient must be re-evaluated in the disease time course, since one can evolve into the other; once MS is diagnosed, the phenotype needs to be specified, as well as if the disease is active or not, and progressive or not (Thompson et al., 2018).

2.1.3. Diagnosis

The diagnosis of MS is based on clinical findings, which are supported by magnetic resonance imaging (MRI) of the brain and spinal cord, and laboratory biochemical analysis

of the cerebrospinal fluid (CSF) (Filippi & Rocca, 2011; Goldenberg, 2012). This process can be difficult, mainly due to the heterogeneous clinical and imaging manifestations of MS, and to the fact that there is no single characteristic or a specific diagnostic test that immediately identifies this condition (Thompson et al., 2018).

The McDonald criteria from the International Panel on Diagnosis of Multiple Sclerosis establishes criteria for the diagnosis of MS, offering a trade-off between sensitivity and specificity. These criteria are the space dissemination criterion (dissemination in space - DIS), the time dissemination criterion (dissemination in time - DIT) and the inflammatory criterion. The first establishes that there must be two or more different lesions in the WM of the CNS. The second says that there must be two or more episodes of active disease that must be confirmed by MRI scans, at least three months after the last episodes or MRI scans. The last criterion instals that there needs to be a chronic inflammation of the CNS, which is evaluated by analysing the CSF; this criterion may replace the DIS if it is not met (Goldenberg, 2012). Even though the 2010 McDonald criteria are widely used, they should not be applied in some situations, and were revised in 2017 by Thompson et al., establishing the 2017 McDonald criteria (Thompson et al., 2018). For a full diagnosis of MS, both the DIS and DIT criteria must be fulfilled, there cannot be an alternative diagnosis, and lesions must be identified in MRI scans, on both dual-echo sequences and post-contrast T1-weighted images (Filippi & Rocca, 2011).

Patients with MS, even in the early phases of the disease, might show signs of cognitive impairment in aspects such as memory, attention, verbal fluency, visual perception, and a slowed processing of information (Sousa et al., 2018). There are many clinical tests performed on MS patients to assess their cognitive status and describe both the severity and the progression of MS, and it is possible to correlate them with MRI metrics (Costa Sousa, 2015). Some of them are briefly described below:

- Expanded Disability Status Scale (EDSS) is a scale ranging from 0 (normal neurological status) to 10 (death due to MS) that may change throughout the progression of the disease according to the patient's physical impairment evolution (Kurtzke, 1983; Meyer-Moock et al., 2014);
- Modified Fatigue Impact Scale (MFIS) is a self-reported questionnaire that assesses the impact and severity of fatigue on the daily lives of patients with MS (Fisk et al., 1994; Gomes, 2011); the scores range from 0 to 84, with higher scores meaning more fatigue (Novo et al., 2018);

- Symbol Digit Modalities Test (SDMT) is a written/oral task that measures cognitive processing speed. Since higher scores mean more correct answers to the test's questions, they are linked to higher processing speeds (Sousa et al., 2018);
- California Verbal Learning Test (CVLT) is an oral task that assesses auditory and verbal memory (Sousa et al., 2018). Its evaluation relies on a total recall score, which ranges from 0 to 80; higher scores indicate a better auditory and verbal memory (Stegen et al., 2010);
- Brief Visuospatial Memory Test (BVMT) is a visual and written task that measures visuospatial learning and memory abilities (Sousa et al., 2018); scores range from 0 to 36, with higher scores indicating better test performance by the subject (Benedict et al., 2020).
- Reading the Mind in the Eyes (RME) assesses subtle cognitive (dys)function through identification of the mental state of other people through photographs of their eyes (Baron-Cohen et al., 2001). Scores range from 0 to 36, with higher scores representing higher cognitive ability (Chalah et al., 2017).

Other tests not illustrated here include, for example, the Multiple Sclerosis Functional Composite (MSFC), which assesses the degree of (physical and cognitive) impairment in MS (Meyer-Moock et al., 2014).

2.2. MRI – basic principles

MRI's basic principle is the phenomenon of nuclear magnetic resonance (NMR), which is then applied to the imaging field. NMR is based on the interaction of magnetic fields with nuclei that have a magnetic moment. Some nuclei such as the Hydrogen nucleus have non-zero individual nuclear moments, also known as spins, that precess at a specific frequency that depends on the intensity of the external static magnetic field (de Figueiredo et al., 2011). This relationship is described by the Larmor Equation, where w_0 is the precessing frequency, or Larmor frequency, B_0 is the intensity of the magnetic field, and the proportionality factor is the gyromagnetic constant:

$$w_0 = \gamma B_0 \qquad \text{Equation 1 (Chan et al., 2019)}$$

When there is a static external magnetic field B_0, the spins form a net magnetization vector (Fig. 2 A), which points to the direction of the vector that represents the magnetic field, since most of the spins are aligned with the direction of B_0. If a radiofrequency (RF)

pulse at the Larmor frequency is applied to the system, the spins will absorb this energy and the net magnetization vector will flip by a certain angle in relation to B_0, leaving its equilibrium state (Fig. 2 B). The net magnetization vector can then be divided into two components: the longitudinal and the transverse component; the first one has a direction parallel to B_0, while the second has a direction perpendicular to B_0. Both the components are precessing, according to the precession of the spins and therefore the net magnetization vector, but the MRI signal comes from the precession of the transversal component around the receiver coil. This movement induces current in that coil, according to the Faraday's law of induction, creating an electric signal that can be read by the MRI system's hardware (Fig. 2 C) (de Figueiredo et al., 2011).

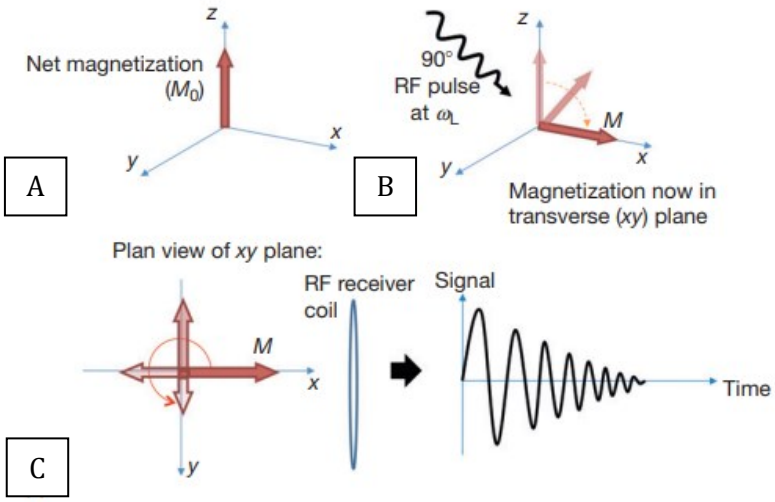

Fig. 2 Schematics of the creation of an MRI signal: A) The net magnetization vector is initially aligned with the direction of the external magnetic field (z axis); B) The net magnetization vector flips to the xy plane when a 90º RF pulse is applied; C) The two components of the magnetization vector precess around the z axis; the movement of the transversal component induces current in the RF receiver coil, creating the signal that decays over time, with the dephasing of spins. Adapted from (Cleary & Guimarães, 2014).

When the RF pulse stops, the tendency is for the net magnetization vector to go back to its equilibrium state, thus decaying the MRI signal (Fig. 2 C). This decay can be due to two main processes: loss of energy to the surrounding media or loss of phase coherence between spins. The first process is a spin-lattice interaction and is characterised by a time constant called T1, being described as a T1 relaxation. In this case, the longitudinal component of the net magnetization vector recovers its full length by growing back along the direction of B_0, via release of energy to the environment. The second process can either happen by spin-spin interactions, and in that case, it is characterised by the time constant T2, being defined as the T2 relaxation, or by inhomogeneities in the external magnetic field, which is characterised by the time constant T2* and considered a T2* relaxation. In both T2 and T2*

relaxations, the transverse component of the net magnetization vector decreases in its magnitude, leading to a decay in the MRI signal (de Figueiredo et al., 2011). These processes are represented by the graphical illustration in Fig. 3.

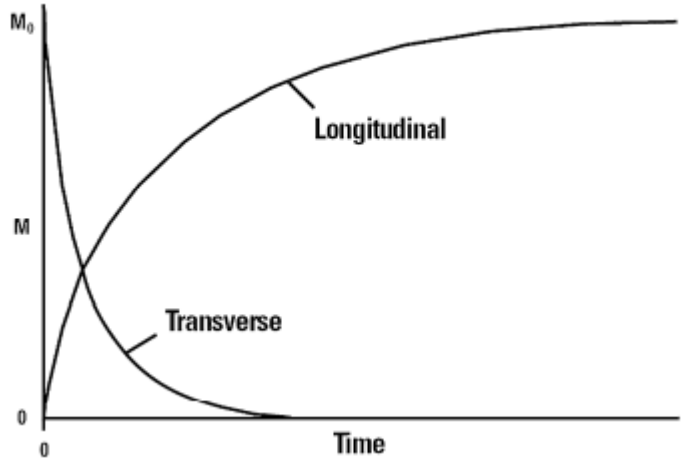

Fig. 3 Representation of the decay of the MRI signal due to T1 effects (recovery of the longitudinal component) and T2/T2* effects (decay in the transverse component). The horizontal axis represents time while the vertical represents the magnitude of the net magnetization vector (de Figueiredo et al., 2011).

The difference between these types of relaxation is what gives the image contrast, and it can be controlled by the MR pulse sequence used. This sequence can be seen as an ensemble of sequences of RF pulses, magnetic field gradient pulses, signal sampling, and time periods between pulses. The RF pulses are responsible for the excitation of the spins, as described above. The magnetic field gradients can spatially encode the MRI signal, by using frequency and phase information, and allow the selection of a slice and single voxels within a slice to be imaged (de Figueiredo et al., 2011).

In the human body, the abundance of Hydrogen and its proper gyromagnetic constant make the Hydrogen nucleus the most used for MRI (de Figueiredo et al., 2011).

2.2.1. Use of Conventional MRI in MS

Since conventional MRI is widely used for the diagnosis of MS, it is important to know how lesions present themselves on a scan. The most common areas of WM lesions in MS are periventricular, juxtacortical and infratentorial, and the corpus callosum (Filippi & Agosta, 2010). The presentation of this damage on an image will depend on the kind of sequence and weighting used (Ceccarelli et al., 2012; Filippi & Agosta, 2010; Filippi & Rocca, 2011), and can either be focal or diffuse, and be found on the WM and the grey matter (GM)

(Pagani et al., 2020). Contrarily to WM injury, GM damage is present in later stages of the disease and is due to axonal damage (Jehna et al., 2013).

MS lesions are found as heterogeneous, varying in the composition of the inflammatory infiltrate, the substrate that is damaged, and the degree of injury; this variation has been observed intra- and inter-individually, in different lesions, and at different stages of MS (Rahmanzadeh et al., 2021). Even though normal appearing brain tissue (NABT), such as normal appearing white matter (NAWM), which is apparently normal in imaging yet can show signs of microstructural damage, presents normal intensity in MRI scans such as T2-weighted images, it is relevant to investigate its properties in the monitoring of MS, since it can be related to development of lesions (Costa Sousa, 2015).

In a dual-echo fluid-attenuated inversion-recovery (FLAIR) sequence (T2-weighted images), WM lesions appear as focal areas of hyperintensity (Fig. 4 A), compared to the normal brain tissue; however, this hyperintensity lacks specificity, i.e., it is not possible to distinguish demyelination from inflammation (for example) solely by looking at these images. On the other hand, findings in T1-weighted images without contrast agents show very hypointense WM lesions (Fig. 4 B) which are commonly called “black holes” and are related to more serious tissue damage (Ceccarelli et al., 2012) and often chronic lesions (Costa Sousa, 2015). If a contrast agent such as Gadolinium is used on a T1-weighted image (Fig. 4 C), active and inactive WM lesions can be distinguished, since this agent only enters cells when the blood-brain barrier is compromised, i.e., it has an increase in permeability; this means that enhanced lesions represent areas of ongoing inflammation (Ceccarelli et al., 2012). Furthermore, the demyelination present in acute MS lesions can lead to axonal injury and later axonal degeneration, which will reflect in an atrophy in WM (Gajamange et al., 2018).

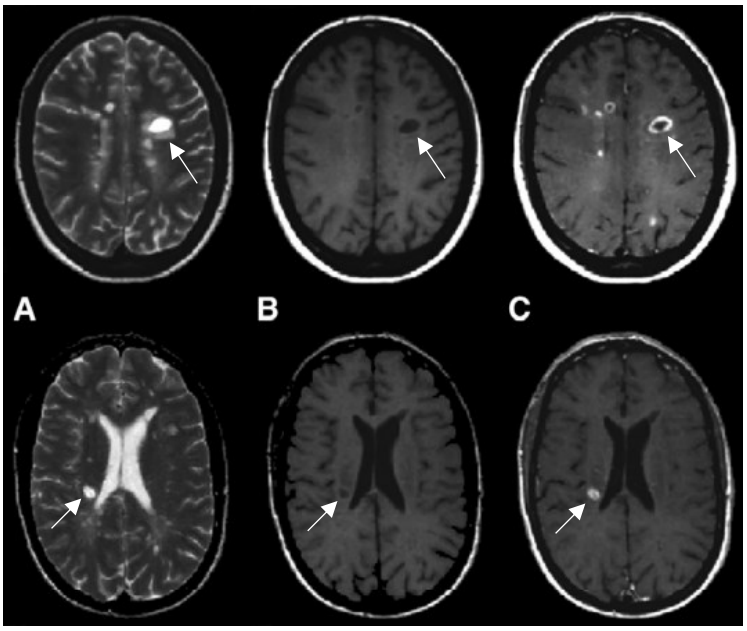

Fig. 4 Axial A) T2-weighted, B) T1-weighted and C) gadolinium-enhanced T1-weighted MR images of the brain of a patient with MS. There are lesions (arrows) that present as hyperintense on the T2-weighted scan (A), hypointense on the T1-weighted scan (B) and as enhanced on the enhanced T1-weighted scan (C) (Filippi & Rocca, 2011).

The detection of GM damage is difficult using conventional MRI (Ceccarelli et al., 2012; Filippi & Agosta, 2010), and the uncovering of these lesions needs a multimodal approach, which couples a sequence sensitive to T2 prolongation and a 3D T1-weighted image. GM atrophy can act as a marker for neurodegeneration in MS, but the mechanisms behind that process are not known. Besides atrophy, both GM diffuse damage and excessive GM iron may be present in patients with MS (Ceccarelli et al., 2012). Even though WM lesions are a main characteristic of MS patients, the WM lesion load only partially correlates with symptoms in MS. In fact, GM damage can better justify the disability often present in MS patients (Jehna et al., 2013).

Finally, spinal cord lesions can be found in patients with MS. The most common is spinal cord atrophy, which is present in all MS subtypes, and correlates with disease status, being independent from brain damage. This atrophy can act as a biomarker, but its utility is limited due to the presence of edema and the fact that it may not be relevant in MS when compared to the variability seen in normal populations (Ceccarelli et al., 2012).

Because conventional MRI lacks sensitivity, there are unconventional MRI techniques that are useful in the diagnosis, evaluation, and monitoring of MS. This sensitivity influences the detection of some lesions, such as grey matter lesions and diffuse changes in NABT (Ceccarelli et al., 2012).

2.3. Unconventional MRI Techniques in MS – Diffusion-Weighted imaging (DWI)

Conventional MRI fails to provide information about the processes behind microstructural changes in MS (Mustafi et al., 2019). Thus, more complex MRI techniques can aid in the detection of lesions in the WM, GM, and spinal cord. However, even though these techniques have higher sensitivity and specificity, they still may not account for specific processes such as inflammation, demyelination, axonal loss, and gliosis (Ceccarelli et al., 2012).

2.3.1. Physics of DWI

The use of DWI allows microstructure probing, by evaluating diffusion properties, which are influenced by the type of tissue and its state (Mustafi et al., 2019). It is non-invasive, has high sensitivity to water movement, uses the existing MRI equipment, and does not require contrast agents or tracers (Soares et al., 2013).

DWI is an unconventional MRI technique based on the diffusion of water molecules inside tissues. This diffusion has a Brownian motion, which means that there is a random movement of water molecules, with no preferred direction. The measurement of this diffusion will then reflect the water molecules displacement, when allowed to move in a certain period (de Figueiredo et al., 2011; Enzinger & Fazekas, 2015).

The DWI signal is obtained by using Stejkal and Tanner's method. Firstly, a 90º pulse (known as first diffusion sensitising gradient lobe) is used to dephase the stationary water spins. A second pulse of 180º refocuses the spins, compensating phase variations due to magnetic field inhomogeneities. Then, another 90º pulse (second diffusion sensitising gradient lobe) is used to rephase the spins by the same amount they were dephased. If the water spins move (diffusion), the second lobe will not be able to rephase them the same amount they were dephased; thus, there will be a signal attenuation, proportional to the degree of water diffusion. The direction of the applied lobes is the diffusion-sensitising direction, affecting spins in that direction only; if one is scanning an anisotropic tissue, where diffusion is not equal in all directions, more than one sensitising direction is needed. This method is mostly combined with spin-echo echo-planar imaging (EPI), taking advantage of a fast acquisition, with fast sampling rates (de Figueiredo et al., 2011).

The amount of diffusion weighting is controlled by a parameter called b-value, that accounts for gradient magnitude, duration, and time between lobes, as described in Equation 2, where γ is the gyromagnetic ratio, G is the strength of the diffusion-sensitising gradients, δ is the duration of the gradient pulse and Δ the time between those gradients. The units of this b-value are s/mm^2 (de Figueiredo et al., 2011):

$$b = \gamma^2 G^2 \delta^2 (\Delta - \frac{\delta}{3})$$ Equation 2 (de Figueiredo et al., 2011)

A common EPI-DWI protocol requires three orthogonal scans with diffusion sensitization in each main gradient direction, averaging them into a final image. It usually uses two b-values, and its choice must rely on a compromise, since higher b-values lead to more diffusion weighting and increased contrast, but the signal-to-noise ratio decreases (de Figueiredo et al., 2011).

In summary, DWI should be performed using high b-values along at least six non-collinear diffusion encoding directions and one minimally T2-weighted image with low b-values. The standard b-value for DWI in clinical practice is 1000 s/mm^2 (Soares et al., 2013).

2.3.2. The use of DWI in MS

In biological tissues, water molecules cannot diffuse freely, since they interact with structures; this means that the amount of water displacement can decrease, and diffusion can be restricted. Taking this into account, it is more meaningful to measure an apparent diffusion coefficient, instead of raw diffusion quantities (de Figueiredo et al., 2011). More specifically, water movement in the brain is restricted by both axons and myelin. Thus, if myelin is present and axonal membranes are intact, there is not diffusion in all directions, i.e., the diffusion is anisotropic rather than isotropic. In fact, there should not exist movement in the perpendicular direction to the longitudinal axis of the axon, which is where myelin and membranes are present (Aung et al., 2013; de Figueiredo et al., 2011). Because there is a demyelination process in MS, it is expected that in MS patients the level of anisotropy is lower when compared to controls, and isotropy levels are higher (Aung et al., 2013).

2.4. DWI processing

2.4.1. Pre-processing (artefacts)

As with other MRI techniques, DWI is prone to artefacts from various sources. These commonly are the system hardware, pulse sequence, type of acquisition and motion. The

two main artefacts that are intrinsic to DWI are image distortions due to eddy currents and motion (Soares et al., 2013).

Eddy currents arise from the fact that the gradients used in DWI are longer and stronger than those used in other weighted MRIs; these gradients induce currents in the MRI scanner by interfering with the magnetic field. The problem with eddy currents is that they are not constant, which means that they can vary with the diffusion gradient, leading to a misregistration between successive images (Soares et al., 2013).

Motion can either be due to macroscopical processes such as head motion, cardiac pulse and breathing, or due to microscopic processes like phase shifts induced by the diffusion of water molecules. This artefact is influenced by the magnitude and duration of the gradients and can be corrected by using pre-processing steps. Furthermore, patients are advised to be as still as possible, to reduce this problem. Its influence on the data can be diminished by decreasing scan time as well, which can be achieved by controlling the pulse sequence. The most used sequence in this case is the single-shot EPI, but it leads to other artefacts related to its characteristics and DWI properties. On the other hand, the use of shorter readout times increases the signal-to-noise ratio and decreases sensitivity to motion, susceptibility to geometric artefacts and blurring; this can be achieved by using phased-array head coils, which enables parallel imaging (Soares et al., 2013).

Another artefact is the vibration effect: because of the gradients applied in DWI, there can be low-frequency mechanical resonances of the MR system, leading to small brain tissue movements. If they happen in the direction of the diffusion-encoded gradient, phase offsets will occur, inducing signal dropouts in DWI images (Soares et al., 2013).

Finally, DWI is also prone to the T2 shine-through artefact, where there can be some T2 contributions to the image. This happens because DWI uses a long repetition time (TR) and a short echo time (TE), as do T2-weighted images. This artefact can be attenuated by using two b-values, where one is equal to zero, to acquire a T2-weighted scan; then, the diffusion image is divided by the b=0 image (de Figueiredo et al., 2011).

The main problem with the existence of artefacts in DWI is that they will lead to erroneous estimations for the diffusion tensor, resulting in wrong parameter values that mean errors in fibre orientation and length estimation (Soares et al., 2013). The reduction of the influence of artefacts in DWI is achieved through pre-processing steps to correct for the effects of all sources of noise described above.

2.4.2. Diffusion-Tensor Imaging

Diffusion-Tensor Imaging is the simplest way of analysing data from DWI images, allowing the evaluation of the integrity of WM tracts in specific neuronal circuits, using tractography (Ceccarelli et al., 2012). It assumes that the movement of water molecules follows a 3D Gaussian distribution, which can be characterised using a diffusion tensor (DT), and DT metrics are sensitive to changes in the WM, and in the NAWM, such as demyelination (Schneider et al., 2017). In fact, the use of DTI probability maps allows for topographical distribution of WM injury to be revealed, assessing NAWM damage regionally. This means that the examination of the topological organisation of specific neuronal circuits is possible, by determining structural connectivity, whose abnormalities contribute to cognitive impairment in MS patients (Ceccarelli et al., 2012).

The principle of this technique is the DT, which models diffusion in a single voxel, by computing a tensor per voxel. It is the 3x3 matrix represented in Fig. 5 A, and is characterised by three eigenvectors, representing an ellipsoid in three dimensions (Fig. 5 B), whose volume describes the mean diffusivity (MD) and whose eccentricity represents fractional anisotropy (FA) (Aung et al., 2013; de Figueiredo et al., 2011). In isotropic media, it is enough to describe water displacement with a parameter that does not depend on fibre orientation, such as MD. However, when movement is anisotropic and the measured diffusivity depends on fibre orientation, MD is not enough to characterise water movement; that is why FA is needed in this case (Basser & Jones, 2002).

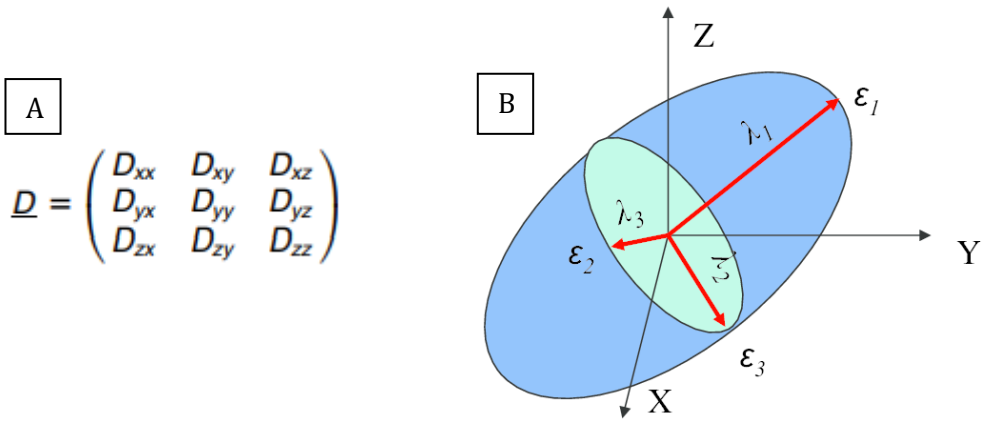

Fig. 5 A) The Diffusion Tensor; D is the diffusion coefficient, which determines how easily one particle can move in that given direction (de Figueiredo et al., 2011); B) The diffusion ellipsoid; λ_1, λ_2 and λ_3 are the three DT's eigenvalues, while ε_1, ε_2 and ε_3 are the eigenvectors (Rane, 2009).

FA is a parameter that describes the fraction of water molecules that move along the orientation of the axon fibre (preferred direction), ranging from 0 (isotropy) to 1 (infinite anisotropy) and is estimated by Equation 3. MD is described by Equation 4; it may not be directly assessed, but it is implicit in another metric, the apparent diffusion coefficient (ADC), which accounts for the fact that diffusion rates may only be apparent, due to the existence of physical barriers that restrict the movement of water (Aung et al., 2013; de Figueiredo et al., 2011). ADC is computed by using Equation 5, where S_0 and S_1 are the signal intensity for a b-value of zero (b_0) and a b-value different than zero (b_1), respectively (de Figueiredo et al., 2011).

$$FA = \frac{\sqrt{(D_{xx}-D_{yy})^2+(D_{yy}-D_{zz})^2+(D_{zz}-D_{xx})^2}}{\sqrt{2(D_{xx}^2+D_{yy}^2+D_{zz}^2)}}$$ Equation 3 (de Figueiredo et al., 2011)

$$MD = \frac{D_{xx}+D_{yy}+D_{zz}}{3}$$ Equation 4 (de Figueiredo et al., 2011)

$$ADC = \ln\left(\frac{\frac{S_1}{S_0}}{b_1-b_0}\right)$$ Equation 5 (de Figueiredo et al., 2011)

To be able to construct a DT, the diffusion-weighted images need to be acquired with at least six different gradient directions, since there are six unknown parameters in the DT; this is because it uses a 3D Gaussian distribution, which has six parameters (Descoteaux, 2015). Apart from the six gradient directions, there is the need to acquire an additional scan, with b=0, which means there should be a minimum of 7 acquisitions, so that diffusion directions can be calculated in anisotropic media (de Figueiredo et al., 2011).

Using the eigenvalues from the DT, it is possible to characterise the direction of diffusion. Radial diffusivity (RD) is the average of the two shortest eigenvalues and characterises diffusion in a perpendicular direction of the long axis of the axonal tract, representing diffusion to myelin. Axial diffusivity (AD) is the largest eigenvalue and characterises diffusion in a parallel direction to the axonal tract, having a greater value than RD in normal conditions. While the eigenvalues represent the magnitude of diffusion in each direction, the associated eigenvectors describe that direction. The discrimination of the direction of diffusion allows for anatomical structural entities to be considered (Aung et al., 2013; de Figueiredo et al., 2011).

DTI parameters can be used in the construction of lesion probability maps, which reveal associations between specific neurologic and cognitive deficits with lesion accumulation in different regions, and in tract-based spatial statistics (TBSS), which can

identify areas where reduced FA in WM tracts predicts cognitive impairment (when there is an overlap between cognitively relevant tracts and areas of high probability for lesions) (Ceccarelli et al., 2012). TBSS is based on the mapping of diffusion indices that are normalised to a stereotaxic space, and statistical tests are then applied to assess the significance of differences between populations. Analysis can also be performed based on regions of interest, by delineating them and determining a diffusion index average for each region, per subject (Costa Sousa, 2015).

DTI has limitations, mainly due to the fact that the measures are voxel-based, such as: when fibres branch or crossover, the assumption that one long axis represents the fibre orientation within the diffusion ellipsoid may not be valid; areas where at least two heterogeneous fibre populations pass within the same voxel may appear to be hypointense on DWI; in areas of tissue partial volume where WM and GM or WM and CSF are in the same voxel, there is diffusion bias, affecting anisotropy (Aung et al., 2013); anisotropy is prone to regional variations due to partial volume effects and noise (F. C. Yeh et al., 2019); the computed metrics are affected in a similar way by changes in the microstructure and changes in the orientational organisation, reducing the interpretability of the results; and the Gaussian model used does not perfectly describe the water displacement (Schneider et al., 2017).

The use of high angular resolution diffusion imaging (HARDI) can help overcome these limitations, thus allowing to perform tractography, which is a great application of DTI, with a more robust approach and providing new anisotropy measures. HARDI uses non-DTI reconstruction methods and typically relies on spherical sampling, having three acquisition strategies that depend on the number of measurements and the b-value(s) (Descoteaux, 2015).

2.4.2.1. Use of DTI in MS – what to expect

The DT is highly affected by the tissue's structure; its geometry depends on axonal density, amount of (de)myelination, the fibre's diameter, and the directions of the WM fibres within the same voxel (Goldberg-Zimring et al., 2005). When there is a disruption of the organisation of axonal fibres, there is a decrease in restriction of water diffusion, resulting in reduced FA and increased ADC values (inversely, low ADC values represent a well-organised structure) (Aung et al., 2013; F. C. Yeh et al., 2019); this happens because water diffusion is restricted in WM by axons (myelinated and demyelinated) but in MS, damage to these structures alter their permeability and water diffusion becomes less restricted

(Goldberg-Zimring et al., 2005) . Thus, anisotropy parameters such as FA and ADC can identify axonal damage that results in the interruption of the diffusion along the axon fibre before obvious structural changes on conventional MRI. However, one must take into consideration that these parameters are not specific to axon and myelin pathology: it is not possible to differentiate between the two kinds of damage just by investigating changes in FA and ADC values (Aung et al., 2013); as a matter of fact, anisotropy levels are maintained mostly by axonal membranes and density, while myelin plays a less important role (Costa Sousa, 2015), which means that damage to both axons and myelin can contribute to a decrease in anisotropy and increase in water diffusion. Still, these parameters are valuable in the identification of MS lesions, since they present decreased FA and AD, and increased ADC and RD values, due to myelin and axonal damage (Aung et al., 2013; Ceccarelli et al., 2012).

Studies have shown that RD seems to be a good indicator of myelin damage, whereas AD is only an indicator of axonal damage in the early stages of MS, since there is no correlation between this parameter and the extent of axonal loss in chronic stages. This happens due to factors such as inflammation, cellular infiltration, or gliosis (Aung et al., 2013). In fact, AD may even have normal values even if demyelination and/or axonal loss is present, because even though smaller calibre axons may disappear, larger calibre axons can be preserved (Costa Sousa, 2015).

In summary, studies show that changes in MS patients include a decrease in FA and an increase in MD/ADC in both WM lesions and NAWM, in the early stages of the disease (de Santis et al., 2019; Granberg et al., 2017; Schneider et al., 2017). It is also recognised that the more marked variations are associated with patients with high disability and progressive forms of MS. Changes in the GM can also be accounted for, in both lesions and normal appearing tissue, and these are associated with physical disability and cognitive impairment. So, there are significant correlations between changes in DTI indices and myelin content and axonal count in NAWM and WM lesions (Schneider et al., 2017). However, in the context of MS, DTI-derived measures may not be able to discern demyelination from axonal loss, since these processes have similar contributions to DTI parameters and cannot be differentiated using these metrics (de Santis et al., 2019).

2.4.2.2. Correlation of DTI metrics with clinical scores in MS

Some studies do not report any association between EDSS and DTI metrics, which may be normal when EDSS scores are low (Hagiwara et al., 2019; Lee et al., 2020). However,

this is not the rule. Barnabéu-Sanz, et. al found positive correlations between EDSS and MD and negative correlations between EDSS and FA, for thalamic connections in RRMS patients (Bernabéu-Sanz et al., 2021). On another example, ElSayed et al. found statistically significant negative correlations between FA and EDSS in both NAWM and tracts of the brain and spinal cord of MS patients. In the corpus callosum tract, they found a positive correlation between ADC and EDSS and a negative correlation between FA and EDSS. Still, this was only valid for SPMS patients; it is important to note that EDSS is related to physical disability. Thus, RRMS patients with low EDSS scores may not have many significant correlations with DTI metrics, since their motor disability may not be impaired at a clinically significant level (ElSayed et al., 2019).

On the other hand, a positive correlation between MFIS and ADC in different WM tracts has been found; however, no association between FA and MFIS was shown. This shows a relationship between fatigue and NAWM damage, here represented by the ADC parameter (Novo et al., 2018).

SDMT also presents some correlations with DTI metrics. For example, Barnabéu-Sanz et. al found a negative correlation between this test's scores and FA, while MD was positively correlated with SDMT scores, in thalamic connections (Bernabéu-Sanz et al., 2021).

A poorer performance in CVLT has been associated with FA reduction in cognitively relevant tracts, such as the sagittal stratum, fornix, and the posterior thalamic radiation. These correlations were strong and supported by an increase in radial diffusivity, which indicates demyelination as a major factor for cognitive impairment in MS (Yu et al., 2012).

BVMT also seems to correlate with DTI metrics, such as FA and MD in forniceal regions. Worse performance on this test has been associated to lower FA values and higher MD in MS patients, using a tract-based approach (Koenig et al., 2012).

DTI-derived parameters are well established to be altered in patients with MS, and correlate with clinical features such as fatigue and disability scores (Bester et al., 2013; Filippi et al., 2001; Rovaris & Filippi, 2007), and social cognition impairment (Batista, Alves, et al., 2017). However, there are scarce data on longitudinal measures, which are crucial to determine mechanisms underlying longitudinal disease progression, with contradicting results showing an association with clinical deterioration (Kolasa et al., 2018; Sämann et al., 2012; Schmierer et al., 2004) or not observing changes over time (Ontaneda et al., 2017; Rashid et al., 2008). These contradictory findings suggest that conventional DTI protocols

might have suboptimal capacity for capturing diffusivity pathological changes in normal appearing WM, which are in principle more subtle than in T2 lesions and follow the early disease course.

2.4.3. Neurite Orientation Dispersion and Density Imaging

Although DTI is a method with high sensitivity for microstructural changes, it lacks specificity since a variation in its measured parameters can be due to a myriad of processes (Zhang et al., 2012). This gives opportunity for methods such as NODDI to arise.

Neurites are the combination of axons and dendrites, which are projections of neurons, and quantifying both neurite density and orientation gives insights into brain function. On one hand, dendritic density represents the branching complexity of dendrites, which may reflect their function: there is an increase in complexion with the development of such function. On the other hand, brain development leads to an increase in the dispersion of neurite orientation distribution, and a decrease in such dispersion is associated with ageing. Other conditions, such as MS, can be linked to changes in neurite morphology (Zhang et al., 2012).

The NODDI model accounts for three types of microstructural environment (intracellular, extracellular and CSF) in which water diffusion has different properties, leading to different DWI signals (Zhang et al., 2012). These compartments are modelled with different diffusion distributions according to the diffusion characteristics. The intracellular space is modelled by a Watson distribution, the extracellular space by a Gaussian anisotropic diffusion distribution and the CSF by a Gaussian isotropic diffusion distribution (Schneider et al., 2017). The difference in diffusion distributions comes from the fact that the considered environments either have hindered or restricted diffusion. Hindered diffusion is present when water movement has a Gaussian pattern and they have their diffusion slowed, but not restricted, which happens in environments such as the extracellular space. Restricted diffusion is present when water movement has a non-Gaussian pattern and diffusion is blocked by barriers, such as cellular membranes; this happens in environments such as the intracellular space (Zhang et al., 2012).

The intracellular compartment – in this case, the axon - is bounded by the neurites' membranes. It is characterised as zero-radius cylinders (sticks) that reflect highly restricted diffusion in the transversal direction and free (unhindered) diffusion along the longitudinal

direction, where the latter leads to an attenuation in DWI signal. The sticks' orientation distribution reflects the spectrum of neurites' orientation in different brain tissues, ranging from highly parallel in some WM structures to highly dispersed in GM (Zhang et al., 2012).

The extracellular compartment is the space bounded by neurites, which slow water diffusion, but do not restrict it, which means diffusion is still anisotropic, as it was in the previously described compartment; this is the space where glial cells and cell bodies (somas) are. The NODDI model expresses parallel and perpendicular diffusivities in the extracellular compartments in terms of the neurite morphology and the intrinsic diffusivity, which means they are determined by both neurite density and orientation dispersion (Zhang et al., 2012).

The final compartment is the CSF, where there is isotropic Gaussian diffusion (Zhang et al., 2012).

Fig. 6 shows how the DWI signal can be decomposed to achieve a mathematical model for each compartment. Level 1 is the distinction between non-tissue signal (from CSF) and tissue signal (WM and GM), while level 2 separates the two compartments that together yield the tissue signal (extracellular or extra-neurite and intracellular or intra-neurite). Lastly, each compartment has a mathematical model assigned, as previously mentioned (Tariq et al., 2016).

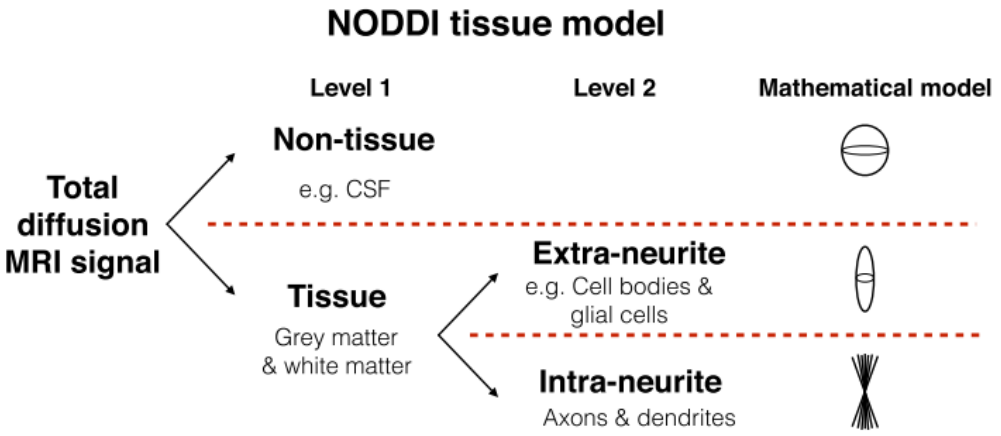

Fig. 6 Decomposition of the DWI signal into tissue and non-tissue. Each contribution has a mathematical model assigned; for non-tissue, it is the Gaussian isotropic diffusion model, while for tissue, it is the Gaussian anisotropic diffusion model for extra-neurite and the Watson distribution for intra-neurite (Tariq et al., 2016).

The NODDI protocol has been developed using two HARDI shells with b-values of 711 and 2855 s/mm^2 (30 and 60 directions, respectively) and nine b=0 images. In fact,

neurite density cannot be estimated using single-shell data, only with at least two-shells (Zhang et al., 2012).

The pre-processing steps in the NODDI model consist in segmenting the images into CSF, GM, and WM, according to criteria such as isotropic diffusion (if it is greater than 80%, it is considered as CSF) and orientation linearity (if it is lower than 0.2 it means that it is the GM, whereas if it is higher than 0.2, WM is identified) (Zhang et al., 2012).

The parameters obtained from this model are the intracellular volume fraction (same as neurite density index), intrinsic free diffusivity, concentration parameter of Watson distribution, mean orientation of Watson distribution, isotropic volume fraction, and isotropic diffusivity; the diffusivities are fixed to their typical values *in vivo*, while the rest of the parameters are estimated through model fitting. The concentration parameter of Watson distribution is later used to compute another value, the orientation dispersion index (ODI) by using Equation 6:

$$ODI = \frac{2}{\pi}\arctan(1/\kappa)$$ Equation 6 (Zhang et al., 2012)

The parameter κ was defined in (Zhang et al., 2011) as a concentration parameter that controlled dispersion in the Watson model; it was then named as orientation dispersion index and redefined as the ODI from Equation 6 in (Zhang et al., 2012).

By estimating the isotropic volume fraction, the contamination by CSF can be eliminated (Zhang et al., 2012). The computed parameters are used to produce maps of metrics such as neurite density index (NDI), ODI and isotropic volume fraction (Schneider et al., 2017).

The map of NDI shows lower neurite density in GM and higher in WM, having the highest values in WM tracts. This means that high intracellular volume fraction is linked to high neurite density, which is higher in WM, since GM has cell bodies and not neurites (Zhang et al., 2012).

The map of ODI shows higher values for GM and lower for WM, having the lowest values in the corpus callosum. This means that there is more orientation dispersion in GM, which is true, since the linearity is more prevalent in WM than in GM. The ODI of neurites can be used to quantify the bending and fanning of axons in the WM, which is useful to map brain structural connectivity, and to quantify the pattern of sprawling dendritic processes in GM. It can also help to determine whether the voxels identified as having crossing fibres really have just one dominant direction (Zhang et al., 2012).

Lastly, the map of isotropic volume fraction displays its highest values in the CSF regions, which means that there is more isotropic diffusion in those areas, as compared to others (Zhang et al., 2012).

A relationship between FA and NODDI measures can be drawn. The most contributing factors to FA are ODI and NDI, and FA is primarily sensitive to ODI: ODI and FA are inversely correlated and exhibit significant regional variation, while NDI shows less changes. Thus, FA is influenced by both the neurite orientation, showing strong negative correlation with ODI in both WM and GM, and a positive weak correlation with intracellular volume fraction. Therefore, for both WM and GM, an FA value can be achieved through a combination of ODI and NDI; two voxels can have the same FA value if the one with the largest ODI value also has the largest NDI value, so that one can compensate for the other (a small change in ODI needs to be compensated with a much larger change in NDI, since FA is more sensitive to ODI variations) (Zhang et al., 2012). The fact that an FA value can be disentangled into changes in density and orientation improves this measure's specificity, meaning that NODDI can differentiate whether a change in FA is due to a loss in neurites or to a change in fibre architecture (Spano et al., 2018).

However great NODDI is, it is not without limitations. The quantification of orientation dispersion is only for isotropic orientation dispersion; there is a level of anisotropy in orientation dispersion, in the case of bending and fanning axons, since dispersion in the main direction of orientation is higher in the plane of bending and fanning and lower in the perpendicular plane (Tariq et al., 2016).

2.4.3.1. Use of NODDI in MS – what to expect

There is evidence of a strong correlation between neurite density and the intensity of myelin damage, leading to the use of neurite density as a marker of MS. Since FA loosely depends on neurite density, maybe NDI could be a better marker for pathology than FA. It may even highlight signs of demyelination earlier, because even if there is a high decrease in neurite values, FA may not reflect it and thus not show alterations in its values and show signs of pathology (Zhang et al., 2012). However, it has been shown that neurite density is primarily sensitive to axonal loss, and to demyelination in a lesser degree (Mustafi et al., 2019).

It has been shown that NDI is lower in both WM lesions and in NAWM (By et al., 2017; Granberg et al., 2017; Grussu et al., 2017; Schneider et al., 2017), which means that there is a loss in neurite density in both tissues, but to a higher degree in WM lesions.

However, it also has been demonstrated that NDI can be higher in lesions, mainly lesions that are not enhanced in the presence of a contrast agent such as Gadolinium, which can be an indicator of remyelination in such tissue (Sacco et al., 2020).

It has also been shown a decrease in ODI in MS lesions (Grussu et al., 2017; Schneider et al., 2017) and an increase in NAWM (By et al., 2017; Grussu et al., 2017; Schneider et al., 2017). These findings support that there is a loss of fibre coherence in NAWM (since ODI increases) and a decrease in axonal density (decrease in NDI). These measures cannot be obtained using the DTI parameters, which reinforces the usefulness of NODDI metrics (Schneider et al., 2017). Still, ODI values can be found to be increased in WM lesions (By et al., 2017; Granberg et al., 2017; Spano et al., 2018), mainly because this parameter reflects a complex combination of structural changes, which can either result in an increase or decrease in the ODI value. Another explanation for this is the healthy brain status: if the normal ODI value is high, then it will experience a decrease in disease; if the normal ODI value is low, then it will be higher in disease (Spano et al., 2018).

Lastly, it has been reported an increase in isotropic volume fraction, which translates into an increase in isotropic diffusion, as expected (Schneider et al., 2017).

The main reason to use NODDI instead of DTI is its ability to differentiate between neurite density and fibre orientation. DTI accounts for these in a single value (FA), thus not discerning these contributions; besides, there may not be a change in FA simply because both ODI and NDI contribute to it, and they can cancel each other out. While both NODDI and DTI are sensitive to changes in MS patients, NODDI can identify the likely nature of these changes, particularly in GM. This is important, since GM involvement in pathology is associated with long term disability, disease progression and cognitive impairment (Spano et al., 2018). Even though the NODDI metrics do not add sensitivity to disease when compared to DTI, they add specificity to inference on pathology. This is due to the water compartmentalization, immunity to fibre crossing, and ability to estimate size, tortuosity, and geometry of axonal sizes (Chen et al., 2021).

2.4.3.2. Correlation of NODDI metrics with clinical scores in MS

Several studies have attempted to investigate correlations between NODDI metrics and clinical scores in MS, mainly EDSS. Spano et al. reported that there are significant negative correlations between NDI and EDSS in several brain regions; the contrary may happen with ODI, where an increase in EDSS can be associated with both a decrease and an

increase in ODI, in different brain regions. However, these correlations may not be true for RRMS patients, since their disability is not as advanced as in SPMS patients, who were found to drive these associations (Spano et al., 2018).

In the specific case of RRMS patients, correlations between EDSS and ODI have been found, in regions such as the left primary motor and somatosensory cortices, with a worsening in EDSS values accompanied by increased ODI (Granberg et al., 2017). Similar to what was reported by Spano et al., but now in the spinal cord, other studies found a strong negative correlation between NDI values and EDSS scores, in the white matter of RRMS patients. This correlation shows how reduced NDI contributes to physical disability in MS patients, namely in the spinal cord, where long axons are present; there can also be correlations in specific parts of the brain, and they are more probable to be found in regions with long tracts (Collorone et al., 2020).

In summary, it is more probable to find correlations between EDSS scores and NODDI metrics when there is clinical disability (EDSS>1) (Rahmanzadeh et al., 2021). This shows that, for lower EDSS values (early phases of MS), disability might be mainly due to inflammation and demyelination, and not neurite loss/neurodegeneration (Margoni et al., 2022).

On the other hand, there is evidence of a positive correlation between NDI and SDMT scores in the grey matter of the left primary motor area, i.e., a decrease in NDI values predicted a poorer performance in SDMT by MS patients. This shows how NODDI metrics can evaluate not only white matter integrity, but also grey matter (Radetz et al., 2021).

Note that the number of correlations illustrated in section 2.4.2.2. ("Correlation of DTI metrics with clinical scores in MS") if far higher than the one presented here. To my knowledge, not many studies attempted to correlate NODDI metrics with the cognitive and neuropsychological tests used in this work. The most common correlations are for EDSS and for the Multiple Sclerosis Functional Composite (MSFC).

2.5. Structural Connectivity

Structural connectivity allows the modelling of the brain as several cortical areas linked by structural pathways. It relies on graph theory, which identifies each cortical area as a node and each structural pathway as an edge; the edges are reconstructed using methods such as tractography and are characterised using parameters that resemble the strength of connection between nodes (Pagani et al., 2020), being either directed or

undirected, unweighted/binary (either it exists or not) or weighted. Graph theory is used since it provides metrics that characterise the topology of a network, and graphs can be represented by using a 2D matrix, also known as a connectivity matrix (C. H. Yeh et al., 2021).

Regarding structural connectivity in later stages of MS, studies have shown that network efficiency is globally disrupted and decreased in specific regions, correlating with increased lesion load. In fact, WM lesions seem to be associated with abnormal neuronal connectivity, which indicates MS as a disconnection syndrome (Pagani et al., 2020).

2.5.1. Tractography

Using DWI, a whole brain streamline tractography can be computed and used to link regions of interest in GM, inferring potential WM connections (edges) between pairs of GM areas (nodes). Using tractography, edges are undirected, because DWI cannot differentiate whether they are afferent or efferent, since the probability of molecular displacement along a vector is the same as that along the antipode (C. H. Yeh et al., 2021). The organisation of fibre tracts (tractography – represented in Fig. 7) is deduced using FA and ADC (Aung et al., 2013).

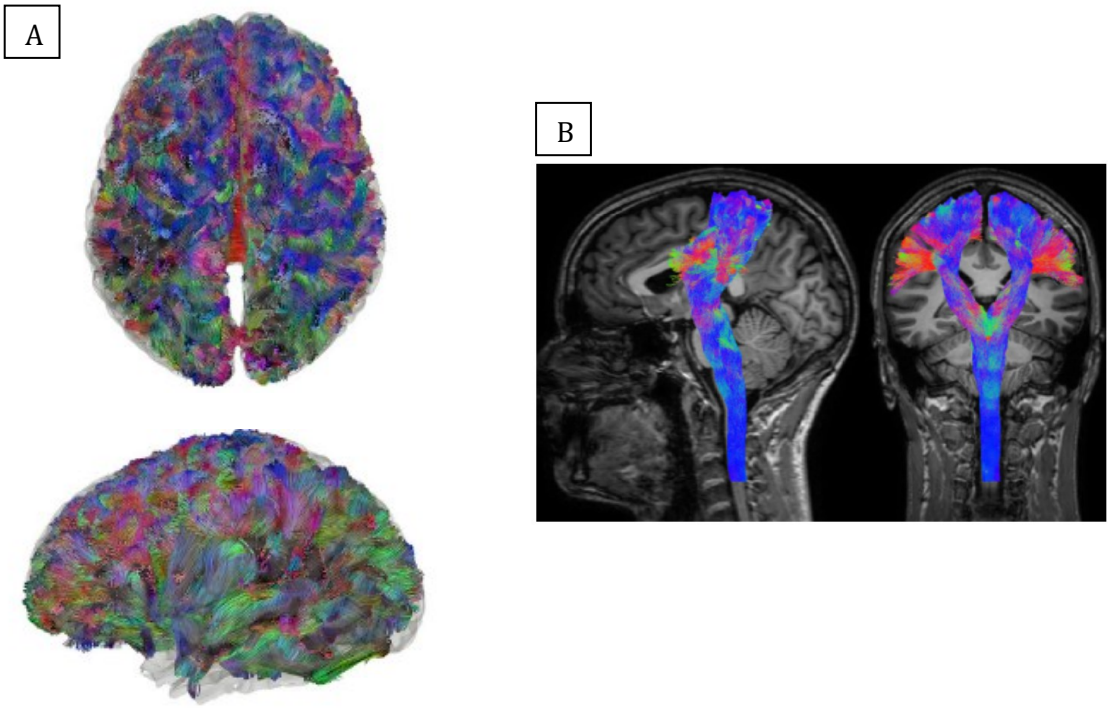

Fig. 7 Tractography of A) whole brain (F. C. Yeh et al., 2019) and B) Corticospinal tract (Jeurissen et al., 2018). The colours in A) represent fibre orientation: red is left-to-right, green is posterior-to-anterior, and blue is inferior-to-superior orientation.

The computation of fibre directions can either rely on a probabilistic or a deterministic approach. Whereas the first uses probabilistic distributions to outline different probable directions, the second gives a result based on the most likely direction in each voxel (de Figueiredo et al., 2011).

This technique is based on three steps. The first step is seeding, which means choosing the areas from where the fibres are drawn. The second step is propagation, which generates the fibres. The last step is termination, which is based on termination criteria (Soares et al., 2013). These criteria are needed since the signal in one voxel comes from more than one neuron. Thus, this data cannot pinpoint the exact location of neuronal cells, and because of that, there is no biological indicator of where a computed streamline should end. The criteria are then based on some constraints that lead to biologically plausible streamlines. These constraints are e.g., that fibres should reach at least the interface of GM and WM at both ends, and fibres cannot terminate either in the middle of WM or CSF (they must connect to cell bodies, which are in GM). If a fibre does not meet these criteria, then it is not biologically plausible. The opposite, however, is not true; just because a fibre meets the criteria, it does not mean that it exists. One can also incorporate anatomical data from magnetic resonance scans in the fibre-tracking process for streamline selection (C. H. Yeh et al., 2021).

Anatomical constrained tractography (ACT) is a variation of the tractography technique that uses T1-weighted images to segment tissue and biological/anatomical *a priori* knowledge to influence the termination and acceptance/rejection of each fibre track. Where there are lesions, T1-weighted images may not be truly reliable, and T2-weighted images (FLAIR) should be incorporated into the pipeline (Horbruegger et al., 2019).

In conclusion, DTI based tractography can be used to generate voxel-scale connectivity maps, which have a scalar value ranking the degree of connection to a seed point in each voxel; regions of voxels with the highest voxel-scale connectivity define pathways connected to the seed point (Costa Sousa, 2015).

2.5.2. Connectome

The connectome is the visual representation of both nodes (GM areas) and edges (WM paths). The nodes are obtained from brain parcellation of anatomical MRI data (Fig. 8 A), either using an individual's image data, or an atlas. The edges can be defined by the number, length, volume, or probability of all streamlines between the corresponding nodes, or by averaging diffusion metrics within the volume along the path of streamlines between the considered nodes (Fig. 8 B) (C. H. Yeh et al., 2021).

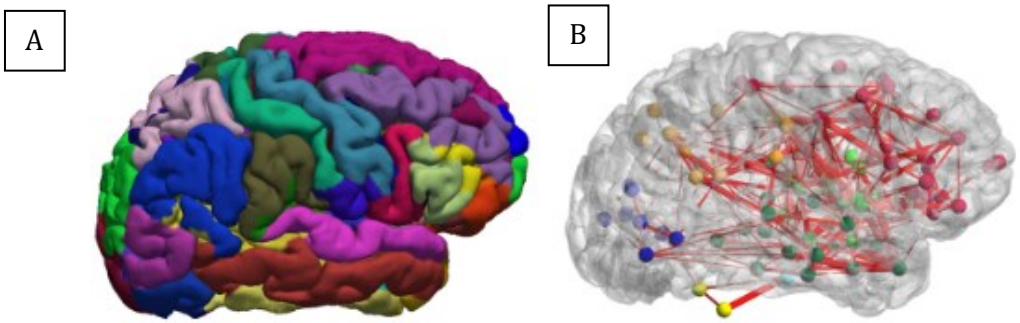

Fig. 8 A) Parcellation of the human brain to identify regions of interest (GM areas/nodes); B) connectome with the lines representing the edges/WM paths and the balls representing nodes/GM regions. Adapted from (Chu et al., 2018).

The construction of the structural connectome requires a streamline-to-node assignment process, to associate streamlines with GM areas, which influences the computed metrics and connectivity patterns. The most sensible way to construct this assignment process is to assign one streamline to only two GM regions. This is compatible with the anatomical knowledge, since an axonal fibre connects two cell bodies in the GM. Hence, the ideal streamline will connect one GM node with another, to represent a neuron-neuron connection (C. H. Yeh et al., 2021).

Since the raw streamline density cannot be used as a valid metric due to its lack of biological meaning, the used connectomes are either binary or weighted. In binary connectomes, streamlines only indicate whether there is a connection; this is achieved using a threshold where if the edges are below it, are set to zero, and otherwise, are set to one. This type of method, however, results in an oversimplification and is not a good portrait of real connections. In weighted connectomes, instead of stating the absence of fibre tracts, it infers the degree of fibre tracts density loss. Using this type of connectome, the weak connections that probably come from noisy data are eliminated through a threshold, which must be carefully chosen, since some weak connections are relevant; this elimination will result in sparse networks. Dense weighted connectomes can be used to compute global

weighted network metrics and do not need a threshold; these metrics are insensitive to the contribution of weak connections to the network (C. H. Yeh et al., 2021).

3. Methods

The data analysed in this thesis were collected in the context of the scientific project BIOMUSCLE, funded by Fundação para a Ciência e Tecnologia (reference PTDC/MEC-NEU/31973/2017). Patients were recruited and clinically evaluated by the members of the project at the Neurology Department of the University Hospital of Coimbra and met the criteria for MS diagnosis according to McDonald Criteria (Thompson et al., 2018). All the participants filled out written informed consent forms before the experiment.

3.1. Participants

Eighteen recently diagnosed RRMS patients (mean age ± standard deviation (sd) = 31.92 ± 8.09 years, 10 females) and eighteen age and sex-matched healthy controls (mean age ± sd = 31.89 ± 8.15 years, 10 females) were included in this study. The RRMS patients underwent neuropsychological and clinical assessment and performed the imaging session and clinical assessment before initiating pharmacological treatment (as per standard of care). Six assessments were included in this evaluation. The first two are scales that measure physical disability (Expanded Disability Status Scale - EDSS) and fatigue (Modified Fatigue Impact Scale - MFIS), four assessments are cognitive tests, namely those composing the Brief Cognitive Assessment for MS (BICAMS) (Langdon et al., 2012), which study brain performance during processing speed (Simplified Digit Modalities Test - SDMT), auditory, visuospatial, and verbal memory tasks (California Verbal Learning Test - CVLT and Brief Visuospatial Memory Test - BVMT, respectively), and the last assessment is a social cognition test (Reading the Mind in the Eyes - RME). Detailed demographic information can be found in Table 1.

Clinical and Demographic Information		
	MS patients	Healthy controls
Gender (females/males)	10/8	10/8
Age (mean ± sd, in years)	31.92 ± 8.09	31.89 ± 8.15
Disease duration (mean ± sd, in years)	0.91 ± 1.81	
EDSS (median ± interquartile range)	1.75 ± 1.00	
MFIS (mean ± sd)	31.78 ± 16.15	
SDMT (mean ± sd)	52.28 ± 9.43	
CVLT (mean ± sd)	50.56 ± 8.66	
BVMT (mean ± sd)	24.44 ± 7.68	
RME (mean ± sd)	24.22 ± 3.39	

Table 1 Summary of demographics for both MS patients and healthy controls.

3.2. DWI and MRI acquisition and analysis

3.2.1. Imaging protocol

MRI data was acquired on a 3 Tesla Siemens Magnetom Prismafit MRI system (Siemens, Munich, Germany). The sequence for T1-weighted images was the MP2RAGE, with voxel size equal to 1x1x1 mm^3, a TE of 3.11 ms, a TR of 5000 ms, 192 slices, and a Field of View (FOV) of 256 mm. The T2-weighted images were acquired with a FLAIR sequence, with voxel size equal to 1x1x1 mm^3, a TR/TE of 4800/441 ms, 160 slices, and a FOV of 256 mm. The DWI acquisition was performed with a voxel size of 1.5x1.5x1.5 mm^3, TR/TE of 3230/89.20 ms, 92 slices, and a FOV of 210 mm, using a multi-shell protocol with b-values of 1000, 2000 and 3000 s/mm^2 (30 gradient directions at b=1000 s/mm^2, 45 gradient directions at b=2000 s/mm^2 and 60 gradient directions at b=3000 s/m^2, with an additional 10 gradient directions for a b-value of 0 s/mm^2).

3.2.2. Pre-processing

The pre-processing of the DWI volumes was made using MRtrix3 as described in (Tournier et al., 2019) and the FMRIB Software Library (FSL) as described in (Jenkinson et al., 2002; S. M. Smith, 2002). The pre-processing of these images allows for the removal of noise sources such as movement and other artefacts. Before this step, however, it was necessary to combine all the raw DWI data with its corresponding .bvec and the .bval files and transform it to the MRtrix3 file extension (.mif); the .bvec file contains three numbers

per line which code the directions in which the gradients were applied in each volume, whereas the .bval file contains one number per line, which is the strength of the applied diffusion gradient in each volume.

In MRtrix3, the pre-processing of the data started with denoising it (using a command that implements noise level estimation and denoising based on random matrix theory). This was followed by Gibb's artefact removal, which is the presence of rings on tissues' boundaries caused by image reconstruction (Archibald & Gelb, 2002) once it was verified that that step did not worsen the images' quality. The next step was to combine the DWI data acquired in the posterior-anterior phase encoding direction with data acquired in the anterior-posterior direction, to estimate and correct magnetic susceptibility-induced geometric distortions in the data. Then, the data were corrected for eddy currents using FSL. Lastly, a brain mask was created using FSL, by thresholding voxels at 0.4; this value was determined after manual adjustments, and by visually inspecting the resulting masks.

3.2.3. Tractography

The tractography generation was done using MRtrix3, FSL, and MATLAB software (version R2019b); MRtrix3 used constrained spherical deconvolution to construct this tractography. The diffusion signal was decomposed into smaller individual fibre orientations, which means deconvolving the fibre orientation distributions for each tissue type (WM, GM, and CSF), using the *dhollander* algorithm, since the data was acquired with a multi-shell protocol. Response functions for each tissue were obtained, which show what diffusion looks like inside each tissue type and with each b-value. Fibre orientation densities were generated for each brain tissue type, which estimate the amount of diffusion in each of the three orthogonal directions; they were later normalised to perform group-level analysis without depending on intensity differences.

After this initial processing, the T1-weighted image was registered into the diffusion space (T1-DWI) using a linear registration algorithm form FSL (FLIRT), so that it could be submitted to FSL's command FAST and a five-tissue type (5tt) image could be created, i.e., a segmented anatomical image; the five tissue types were GM, subcortical GM, WM, CSF, and pathological tissue (MS lesions). The latter was edited into the 5tt image and was created using the Lesion Segmentation Toolbox (LST) for SPM12 (SPM – Statistical Parametric Mapping) in MATLAB; for that, the T2-weighted image was registered to the T1-DWI image in the same manner as described above, and then submitted to the LST algorithm, along with the T1-DWI, for automatic lesion segmentation and creation of (individual) lesion

maps. Then, a boundary between WM and GM was created, so that the seeds for the tractography could be placed along that boundary. These processes help to anatomically constrain the tractography.

Using ACT, tractography was constructed, using 10 million streamlines, as recommended; this was done using MRtrix3, in a probabilistic manner, and with plausibility criteria that is based on anatomical knowledge. However, the generated tractogram still had under and over-fitted tracts and was thus filtered using Spherical-deconvolution Information Filtering (SIFT), as described in (R. E. Smith et al., 2013).

3.2.4. Connectome

The brain connectome was constructed using MRtrix3. Firstly, the T1-weighted image was pre-processed using the Freesurfer software, to obtain the parcellation image from the Desikan-Killiany atlas (84 regions of interest, ROIs) and then the connectome construction was made using the ROIs as nodes and the weights derived from the SIFT process as edges between nodes.

3.2.5. DTI and NODDI maps

The DTI estimation was done using MRtrix3, and FA, ADC, AD and RD maps were derived. NODDI fitting was performed using the NODDI toolbox Version 1.05 as described in https://www.nitrc.org/projects/noddi_toolbox for MATLAB, generating maps of ODI, NDI and isotropic volume fraction.

DTI and NODDI measures were pre-processed using TBSS (S. M. Smith et al., 2006) from FSL (S. M. Smith et al., 2004), using predefined scripts available in the software. The FA maps were eroded, and the end slices were set to zero, so that outliers could be removed. The other maps were also fed into TBSS, which can also analyse non-FA data using adapted scripts. After this processing, the data were aligned with a target image in a standard space (FMRIB58_FA image, as suggested in https://fsl.fmrib.ox.ac.uk/fsl/fslwiki/TBSS/UserGuide), using a nonlinear registration. Then, the target image was aligned with the 1x1x1mm^3 standard MNI152 space using an affine transformation. Finally, each individual data was brought to the MNI152 space by using the nonlinear transform to the target image followed by the affine transform to the MNI152 space. The result was a 4D image with all the participants' 3D data merged in a single file. A mean of the individual images was also created, as was a mean data skeleton, via a skeletonization process. The final step used in TBSS before any statistical analysis is to

apply a threshold to the mean FA skeleton image, which was set to 0.2, a common value for this process (as suggested in https://fsl.fmrib.ox.ac.uk/fsl/fslwiki/TBSS/UserGuide; a visual inspection of the thresholded image shows that it is predominantly white matter). This thresholded mean skeleton is what is used in TBSS statistical processing.

3.3. Statistical Analysis

3.3.1. TBSS – Tract-based statistics on the skeletonised data

Using TBSS, the skeletonised maps from the previous section were analysed, using voxel-wise statistics, incorporated in TBSS scripts; however, note that this is not a true "voxel-wise" analysis, since TBSS uses a skeleton, rather than all voxels in the image. The main goal was to identify differences in diffusion metrics between the two groups (patients and healthy controls), in different voxels. This was achieved through the randomise tool (Winkler et al., 2014) from FSL, which is a permutation method (nonparametric test) used for inference on statistic maps when the null distribution is not known, as described in https://fsl.fmrib.ox.ac.uk/fsl/fslwiki/Randomise.

Before running randomise, a design matrix and a contrast file were generated through TBSS scripts. Randomise was used with the Threshold-Free Cluster Enhanced (TFCE) option and 5000 permutations.

3.3.2. SPM – Voxel-wise differences between groups

Using SPM, it was possible to infer differences between the MS patients' group (MSC) and the healthy controls' group (CNT), truly voxel-wise over the whole brain. This means that the software compared scans from different groups voxel by voxel, originating difference maps with multiple comparisons. The input images for SPM were FA, ADC, ODI and NDI scans registered into the MNI152 standard space using TBSS, as described in the previous Methods section. These scans were smoothed using a filter with 3 mm Full-Width at Half-Maximum (FWHM), to achieve Gaussianity so that Gaussian random field theory could be applied, to correct for multiple comparisons, and to correct for putative misalignment issues (S. M. Smith et al., 2006).

The statistical model was designed using the CAT12 toolbox for SPM12; this design comprised a two-sample t-test, with covariates, and with and without masking. The considered covariates were age, gender, and total intracranial volume (TIV), which was

estimated using CAT12. The used masks were a global lesion map, and global NAWM. The first was obtained by combining (adding) the individual lesion maps from each individual in the MSC group (Fig. 9 A) and then binarizing the final image (Fig. 9 B), using FSL (this mask is referred as "global lesion mask" thereafter). The second was achieved by extracting the WM image obtained from the segmentation of the T1 image of each subject in the CNT group, which was done in CAT12 when estimating the TIV, and then averaging them in SPM. Then, the mean image was thresholded at 0.6 so that it could be binarized, creating as little regions with non-WM tissue as possible; this threshold was chosen from a range of thresholds, by visually inspecting the images. Finally, the NAWM mask came from subtracting the global lesion mask from the WM mask, and then setting negative values to 0, which came from lesions outside the defined WM mask (this mask is called "global NAWM mask" – Fig. 9 C).

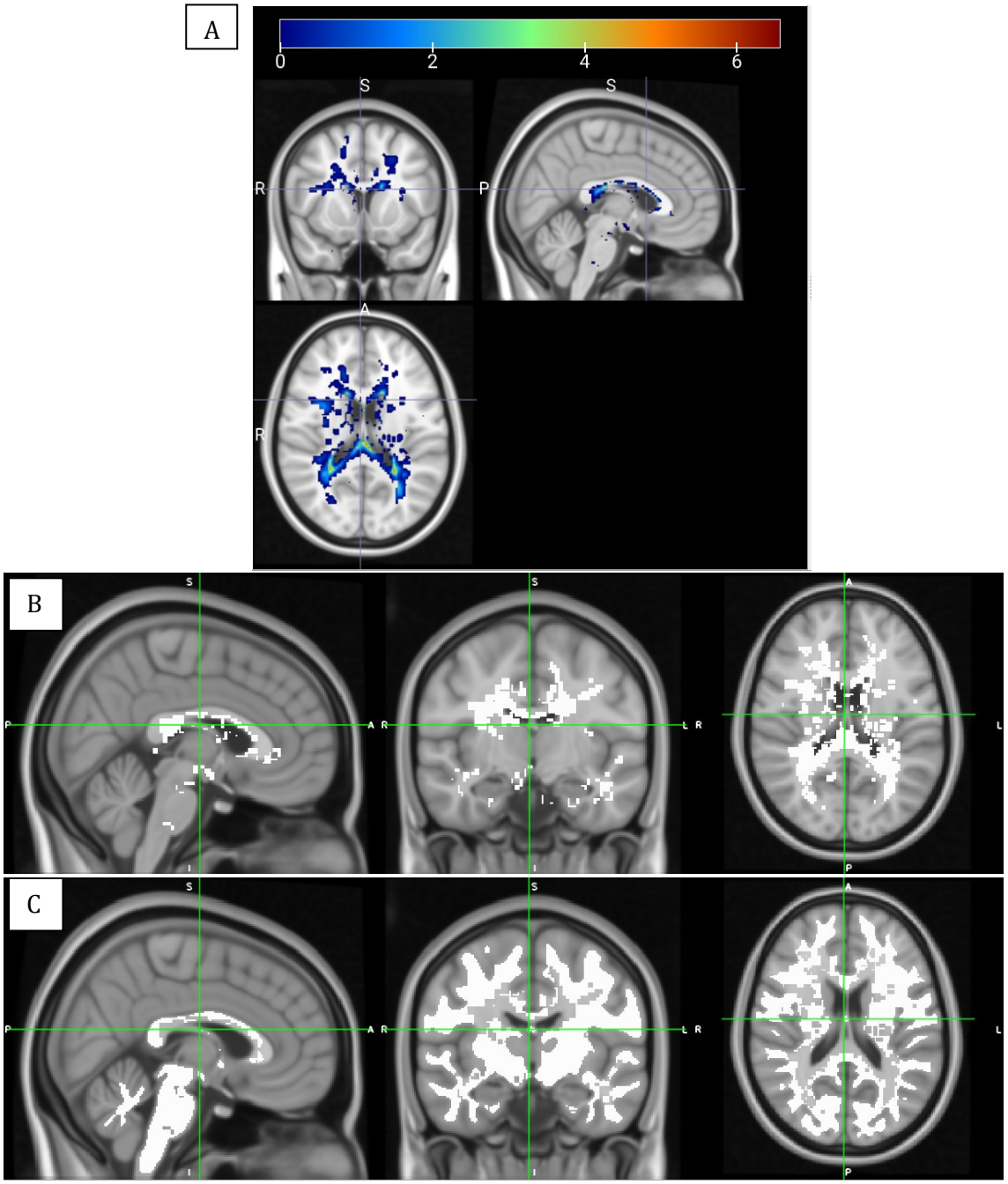

Fig. 9 A) original and B) binarized lesion map mask, and C) NAWM mask. The masks are overlaid on a MNI152 T1-weighted template, and the slice shown has the MNI coordinates 3, -11,18 mm. In A) the colours range from deep blue (minimum value) to deep red (maximum value) and the scale here represented is 0:6.562.

Apart from the designs using the global masks, individual masks were also considered. For that, the model design had the same specifications as described above, except for the masking step. Instead of using an explicit mask, the images fed into CAT12 were previously masked in the following manner: each participant's scan was multiplied by their own individual mask (either NAWM or WM); these masks were originated during the anatomical image segmentation and were then processed accordingly to what was previously described, excluding all averaging steps. In this analysis, the images were

thresholded, so that any voxel that was not present in at least one scan could be excluded from voxel-wise analysis. For that, for each parameter (FA, ADC, ODI and NDI), the considered threshold was the minimum value across all NAWM/WM images.

Then, the models were estimated using SPM and between-group differences were tested. Two different contrasts were defined, taking the considered differences into account: MSC>CNT and CNT>MSC; these contrasts allow to statistically make inferences of where values of the diffusion metrics are greater in the MSC group than in the CNT group and vice-versa, respectively. Because we were in the presence of multiple comparisons (many voxels), the obtained p-values needed to be corrected, and this was done with False Discovery Rate (FDR), with a significance level at $p<0.05$. The cluster extent threshold (minimum number of voxels in a cluster for being considered significant) for each map was estimated directly from the data by SPM.

3.3.3. Means in Tissues of Interest

To further verify results from voxel-wise analysis in SPM and perform summary statistics of differences in diffusion metrics in different tissues (lesions and NAWM in MS patients, and WM in healthy controls), means and standard deviations of FA, ADC, ODI and NDI were computed, using MATLAB. This was done by averaging each metric for each participant, in each tissue of interest (NAWM, WM and lesions) and then averaging across groups, yielding one single mean value and standard deviation, for each parameter, in each tissue (knowing that NAWM and lesions were the tissues considered for the MSC group and WM for the CNT group). Then, statistical analysis was performed to compare such means and assess if there were differences that could be considered statistically different.

Using MATLAB, the normality for each set of means was checked, and all came back as normally distributed, using a Kolmogorov-Smirnov test. Thus, to evaluate the differences in means, a two-tailed t-test was used, considering equal or unequal variances, according to a previously performed F-test for variances, and with a significance level at $p<0.05$. Comparisons made were WM vs NAWM, WM vs lesions and NAWM vs lesions; for the first two, the t-test was for independent samples, whereas for the NAWM vs lesions comparison, since these measures belong to the same subjects, the paired samples t-test was used.

3.3.4. Correlation of DTI and NODDI metrics with clinical scores

Lastly, the cognitive and neuropsychological assessments described in section 3.1 (“Participants") were used to verify if correlations could be established between them and DTI (FA, ADC) and NODDI (ODI, NDI) parameters.

For correlations of DTI and NODDI parameters with EDSS, the Spearman’s rank correlation was used, since EDSS does not follow a normal distribution. However, for MFIS, SDMT, CVLT, BVMT and RME, Pearson’s correlation was chosen since these are normally distributed. All estimations were performed using MATLAB. A statistically significant correlation was considered if the p-value was below the significance level of 0.05; the p-value was corrected for multiple corrections via FDR correction (qFDR).

These correlations were performed on tissues of interest (NAWM and lesions) and on regions of interest (ROIs). These ROIs were extracted from the Atlas provided by Neuromorphometrics, Inc., using a script provided online by K. Nemoto (25 April 2015) available on https://www.nemotos.net/?p=1083. After extraction, the ROIs were registered into the MNI space, thresholded (threshold of 0.7 for all ROIs, except the Optic Chiasm, where the threshold was 0.6), and then binarized, using FSL. Thus, one rho/r (EDSS and other tests, respectively) and one p-value for each ROI were computed, representing the correlation between the parameter in that region with the cognitive/neuropsychological score.

4. Results

4.1. Voxel-wise FA comparisons

Voxel-wise comparison of FA values shows that there are no statistically significant differences for the contrast MSC>CNT in the analysis performed in the whole brain, global NAWM mask and global lesion mask. The same happens for the analysis with the individual NAWM/WM masking process. On the contrary, the CNT>MSC contrast shows statistically significant differences in all considered tissues (Fig. 10 A-D), with 128 clusters (extent threshold of 15 voxels) in the whole brain, 124 clusters (extent threshold of 19 voxels) in the global NAWM, 73 clusters (extent threshold of 29 voxels) in the individual NAWM/WM, and 32 clusters (extent threshold of 70 voxels) in the global lesion mask.

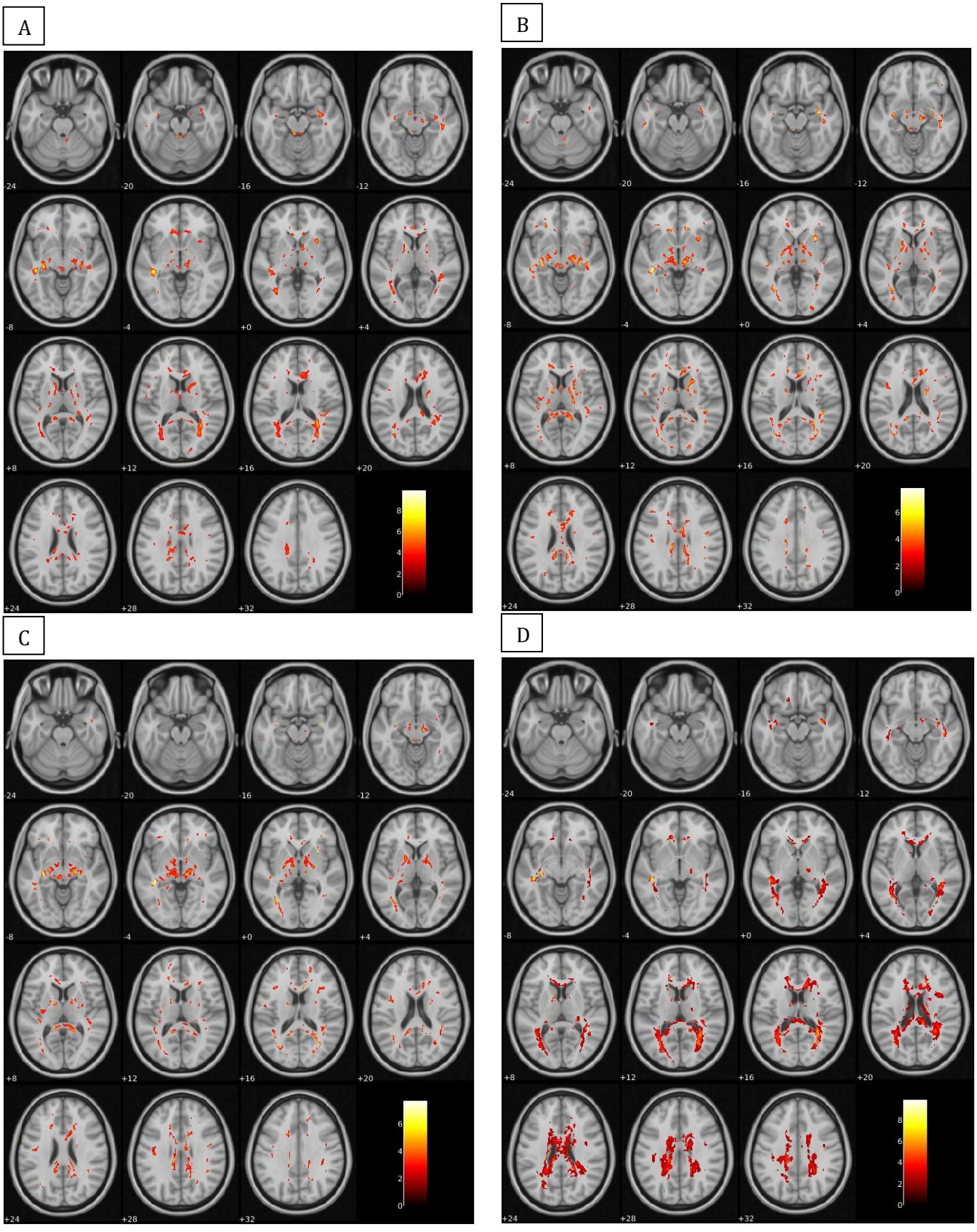

Fig. 10 Voxel-wise analysis of FA with the CNT>MSC contrast and significance value at 0.05 (corrected with FDR), highlighting statistically significant differences where the FA value is lower in the MSC group than in the CNT group in A) whole brain analysis, B) analysis with global NAWM masking, C) analysis with individual NAWM masking and D) analysis with global lesion map masking; the differences are overlaid on a MNI152 T1-weighted template image (slices -24 to 32) and the colour bar represents t-statistic values.

4.2. Voxel-wise ADC comparisons

Voxel-wise comparison of ADC values shows that there are no statistically significant differences for the contrast CNT>MSC in the whole brain, global NAWM mask and global lesion mask analysis. The same happens for the analysis with the individual NAWM/WM masking process. On the contrary, the MSC>CNT contrast shows statistically significant differences in all considered tissues (Fig. 11 A-D), with 49 clusters in the whole brain (extent threshold of 28 voxels), 31 clusters in the global NAWM (extent threshold of 57 voxels), 3 clusters in the individual NAWM/WM (extent threshold of 179 voxels), and 4 clusters in the global lesion map (extent threshold of 273 voxels).

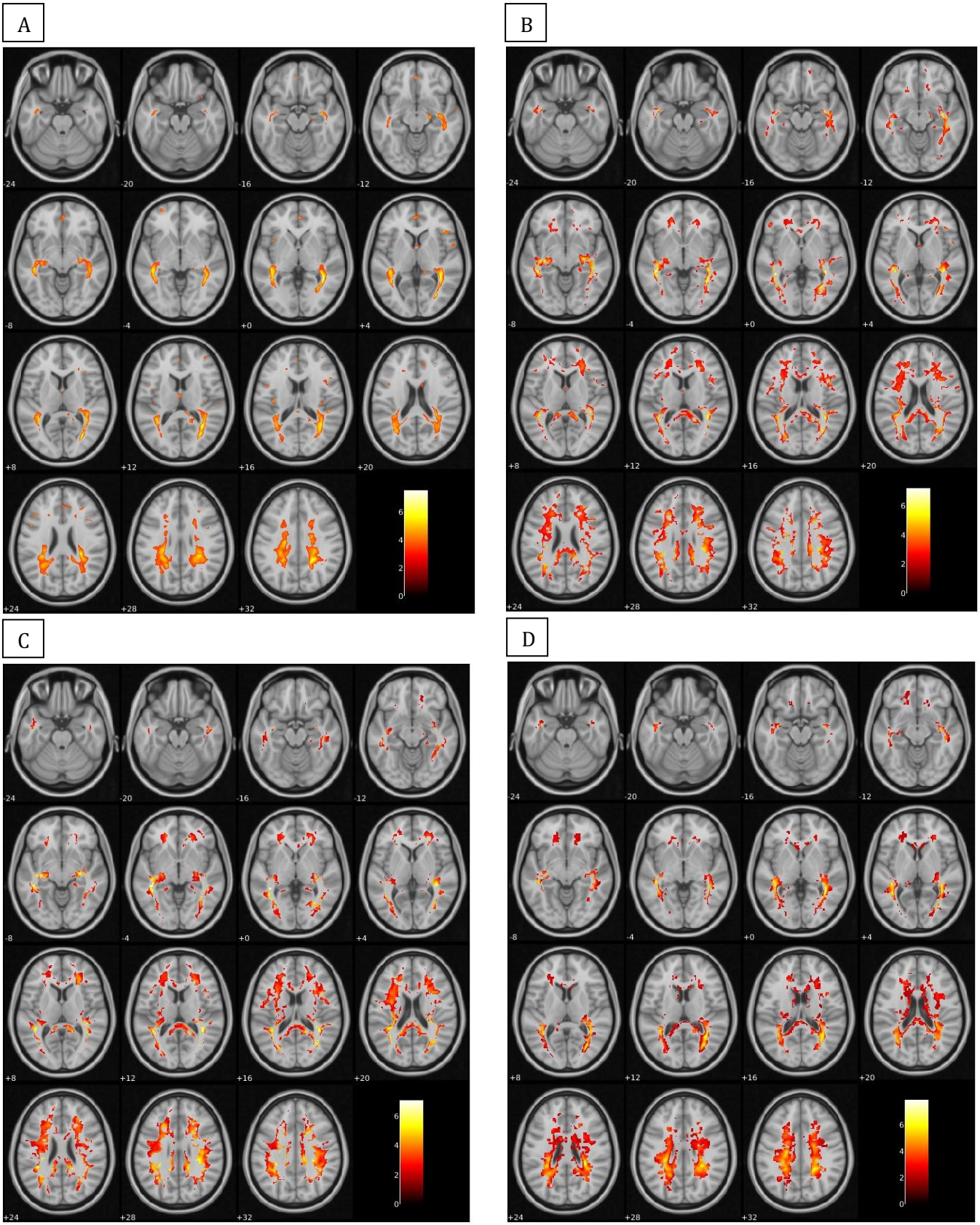

Fig. 11 Voxel-wise analysis of ADC with the MSC>CNT contrast and significance value at 0.05 (corrected with FDR), highlighting statistically significant differences where the ADC value is greater in the MSC group than in the CNT group in A) whole brain analysis, B) analysis with global NAWM masking, C) analysis with individual NAWM masking and D) analysis with global lesion map masking; the differences are overlaid on a MNI152 T1-weighted template image (slices -24 to 32) and the colour bar represents t-statistic values.

4.3. Voxel-wise ODI comparisons

Voxel-wise comparison of ODI values shows that there are no statistically significant differences for both contrasts in both whole brain and lesion map analysis. However, for both the global NAWM masking and the individual NAWM/WM masking process, there are statistically significant differences for the MSC>CNT contrast (Fig. 12 A-B), with 10 clusters (extent threshold of 9 voxels, and extent threshold of 13 voxels, respectively).

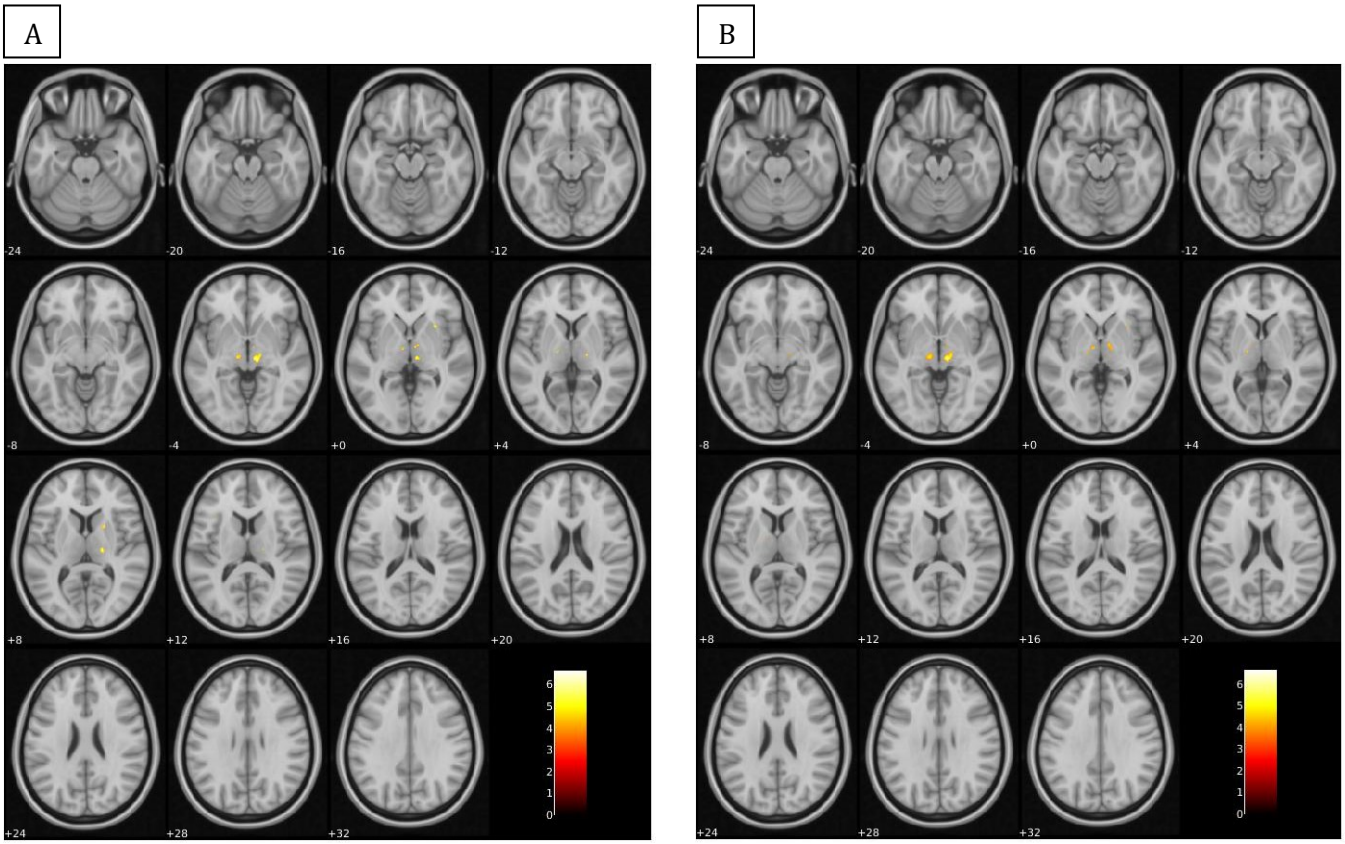

Fig. 12 Voxel-wise analysis of ODI with the MSC>CNT contrast and significance value at 0.05 (corrected with FDR), highlighting statistically significant differences where the ODI value is greater in the MSC group than in the CNT group in A) analysis with global NAWM masking and B) analysis with individual NAWM masking; the differences are overlaid on a MNI152 T1-weighted template image (slices -24 to 32) and the colour bar represents t-statistic values.

4.4. Voxel-wise NDI comparisons

Voxel-wise comparison of NDI values shows that there are virtually no statistically significant differences for the contrast MSC>CNT in the global and individual NAWM and lesion map analysis. There was only a significant small cluster (with 22 voxels) in the whole brain for this contrast, located in the left superior parietal lobe, which was interpreted as a false positive, since this was an unexpected finding for this contrast. On the contrary, the CNT>MSC contrast shows statistically significant differences in all considered tissues (Fig. 13 A-D), with 16 clusters in the whole brain (extent threshold of 79 voxels), 8 clusters in the global NAWM (extent threshold of 124 voxels), 5 clusters in the individual NAWM/WM

(extent threshold of 340 voxels), and 1 cluster in the global lesion mask (extent threshold of 520 voxels).

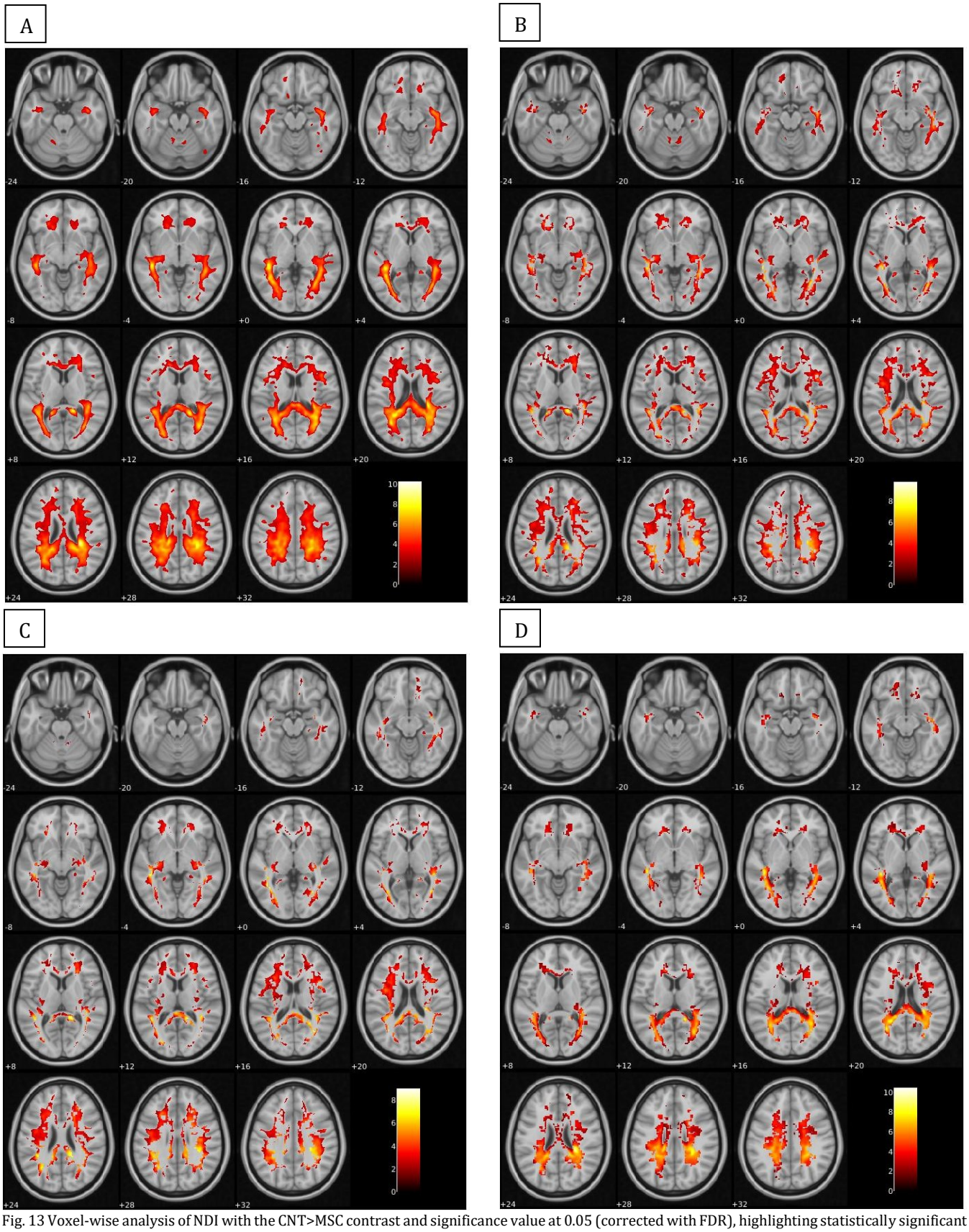

Fig. 13 Voxel-wise analysis of NDI with the CNT>MSC contrast and significance value at 0.05 (corrected with FDR), highlighting statistically significant differences where the NDI value is lower in the MSC group than in the CNT group in A) whole brain analysis, B) analysis with global NAWM masking, C) analysis with individual NAWM masking and D) analysis with global lesion map masking; the differences are overlaid on a MNI152 T1-weighted template image (slices -24 to 32) and the colour bar represents t-statistic values.

4.5. Location of voxel-wise differences

Voxel-wise differences were located using the SPM default atlas (Neuromorphometrics labels provided by Neuromorphometrics, Inc.). These results are in Table 2, Table 3, Table 4, Table 5, Table 6, Table 7, Table 8, Table 9, Table 10 and Table 11. The number of voxels, qFDR (q-value), MNI coordinates and t-value are shown for the most significant cluster of each region, and for peak-level.

Voxel-wise differences in FA (Whole brain) CNT>MSC				
Region	**MNI coordinates [x;y;z] (mm)**	**t-value**	**qFDR**	**# voxels**
Left Cerebral White Matter (LCWM)	[-40;-32;-6]	9.926	0.00003	884
Right Cerebral White Matter (RCWM)	[30;13;-1]	7.113	0.00069	274
Left Ventral Diencephalon (LVDC)	[-7;-6;-12]	6.917	0.00101	98
Brain Stem (BS)	[0;-28;-5]	6.793	0.00128	249
Right Ventral Diencephalon (RVDC)	[9;-22;-3]	6.205	0.00276	691
Left Cerebellum White Matter (LCumWM)	[-21;-58;-33]	5.851	0.00444	66
Left Anterior Cingulate Gyrus (LACG)	[-4;35;4]	5.832	0.00456	109
Right Angular Gyrus (RAG)	[49;-58;34]	5.676	0.00572	47
Left Caudate (LC)	[-10;9;7]	5.654	0.00586	322
Right Cerebellum Exterior (RCE)	[33;-56;-48]	5.510	0.00696	222
Right Cerebellum White Matter (RCumWM)	[21;-59;-33]	5.458	0.00746	119
Left Pallidum (LP)	[-21;-8;1]	5.412	0.00796	195
Right Putamen (RPu)	[24;-5;9]	5.351	0.00873	139
Right Thalamus Proper (RTP)	[19;-19;9]	5.318	0.00922	89
Right Caudate (RC)	[12;3;10]	5.252	0.01008	470
Right Amygdala (RAm)	[16;-5;-18]	5.209	0.01078	76
Left Thalamus Proper (LTP)	[-18;-24;-2]	5.086	0.01242	59
Right Superior Frontal Gyrus (RSFG)	[26;27;52]	4.972	0.01429	56
Left Posterior Cingulate Gyrus (LPCG)	[-1;-36;26]	4.917	0.01506	63
Left Opercular part of the Inferior Frontal Gyrus (LOPOFIFG)	[-48;7;12]	4.721	0.01868	41
Right Pallidum (RP)	[19;-3;3]	4.570	0.02165	22
Left Putamen (LPu)	[-27;-15;5]	4.569	0.02168	23
Left Superior Frontal Gyrus Medial Segment (LSFGMS)	[-5;45;47]	4.550	0.02224	44
Left Superior Parietal Lobule (LSPL)	[-17;-60;58]	4.544	0.02241	21
Left Planum Polare (LPP)	[-40;-7;-14]	4.529	0.02276	31
Left Lateral Ventricle (LLV)	[-5;-2;12]	4.508	0.02314	90
Left Postcentral Gyrus (LPG)	[-40;-36;57]	4.473	0.02378	53
Right Inferior Temporal Gyrus (RITG)	[42;-2;-39]	4.387	0.02595	22
Left Middle Cingulate Gyrus (LMCG)	[-4;21;26]	4.185	0.03043	39
Cerebellar Vermal Lobules VI-VII (CVLVIVII)	[-3;-72;-28]	4.155	0.03130	27
Left Supplementary Motor Cortex (LSMC)	[-6;0;62]	4.012	0.03561	23

Table 2 Locations of the voxel-wise statistically significant differences in FA in the whole brain for the CNT>MSC contrast, according to the Neuromorphometrics labels; t-value represents the value of the t-test's statistic; qFDR represents the FDR-corrected p-value. The details of the regions identified here belong to the clusters with higher t-value for each region and are for peak-level.

Voxel-wise differences in FA (NAWM) CNT>MSC				
Region	**MNI coordinates [x;y;z] (mm)**	**t-value**	**qFDR**	**# voxels**
GLOBAL NAWM				
Left Cerebral White Matter (LCWM)	[-40;-30;-8]	7.846	0.00062	613
Right Cerebral White Matter (RCWM)	[30;13;-1]	7.112	0.00133	470
Right Ventral Diencephalon (RVDC)	[9;-22;-3]	6.206	0.00280	3430
Left Cerebellum White Matter (LCumWM)	[-21;-58;-33]	5.851	0.00393	311
Brain Stem (BS)	[-6;-35;-16]	5.605	0.00516	79
Right Cerebellum White Matter (RCumWM)	[21;-59;-33]	5.457	0.00600	1075
Right Cerebellum Exterior (RCE)	[33;-49;-49]	4.754	0.01133	81
Left Putamen (LPu)	[-27;-15;5]	4.569	0.01276	185
Left Postcentral Gyrus (LPG)	[-40;-36;57]	4.475	0.01358	126
Right Inferior Temporal Gyrus (RITG)	[42;-2;-39]	4.389	0.01446	96
Left Cerebellum Exterior (LCE)	[-29;-72;-44]	4.011	0.01892	122
Right Postcentral Gyrus (RPG)	[37;-15;36]	3.687	0.02449	62
Left Ventral Diencephalon (LVDC)	[-10;-17;-13]	3.652	0.02538	23
Left Thalamus Proper (LTP)	[-9;-7;14]	3.542	0.02802	45
Right Lingual Gyrus (RLG)	[20;-60;-7]	3.418	0.03150	27
Right Precentral Gyrus (RPreG)	[12;-25;69]	3.351	0.03351	21
INDIVIDUAL NAWM				
Left Cerebral White Matter (LCWM)	[-40;-33;-4]	7.739	0.00022	222
Right Cerebral White Matter (RCWM)	[30;13;-1]	7.169	0.00045	76
Right Ventral Diencephalon (RVDC)	[9;-22;-3]	6.262	0.00145	2793
Left Cerebellum White Matter (LCumWM)	[-21;-58;-33]	5.898	0.00231	669
Left Pallidum (LP)	[-21;-8;1]	5.501	0.00375	2793
Right Cerebellum White Matter (RCumWM)	[26;-39;-37]	5.188	0.00595	1164
Brain Stem (BS)	[-6;-34;-15]	4.821	0.00794	61
Left Ventral Diencephalon (LVDC)	[-10;-17;-13]	3.670	0.01859	42

Table 3 Locations of the voxel-wise statistically significant differences in FA in NAWM (global and individual) for the CNT>MSC contrast, according to the Neuromorphometrics labels; t-value represents the value of the t-test's statistic; qFDR represents the FDR-corrected p-value. The details of the regions identified here belong to the clusters with higher t-value for each region and are for peak-level.

Voxel-wise differences in FA (Lesion Map) CNT>MSC				
Region	**MNI coordinates [x;y;z] (mm)**	**t-value**	**qFDR**	**# voxels**
Left Cerebral White Matter (LCWM)	[-40;-32;-6]	9.913	0.000002	48014
Left Caudate (LC)	[-9;9;7]	5.540	0.000688	244
Right Cerebral White Matter (RCWM)	[13;3;10]	5.217	0.001156	73
Right Ventral Diencephalon (RVDC)	[7;-5;-13]	4.699	0.002431	158
Right Thalamus Proper (RTP)	[19;-19;-5]	4.363	0.003625	187
Left Lateral Ventricle (LLV)	[-5;-3;11]	3.939	0.005641	98

Table 4 Locations of the voxel-wise statistically significant differences in FA in the (global) lesion mask for the CNT>MSC contrast, according to the Neuromorphometrics labels; t-value represents the value of the t-test's statistic; qFDR represents the FDR-corrected p-value. The details of the regions identified here belong to the clusters with higher t-value for each region and are for peak-level.

Voxel-wise differences in ADC (Whole brain) MSC>CNT				
Region	**MNI coordinates [x;y;z] (mm)**	**t-value**	**qFDR**	**# voxels**
Right Cerebral White Matter (RCWM)	[38;-47;0]	7.564	0.00487	19219
Left Middle Frontal Gyrus (LMFG)	[-27;58;-2]	6.235	0.00852	128
Left Cerebral White Matter (LCWM)	[-42;-34;-6]	5.779	0.00852	18032
Left Postcentral Gyrus (LPG)	[-41;-37;57]	5.614	0.00852	160
Right Superior Frontal Gyrus Medial Segment (RSFGMS)	[0;44;-10]	5.524	0.00852	265
Right Frontal Operculum (RFO)	[42;26;4]	5.259	0.00858	184
Right Superior Frontal Gyrus (RSFG)	[24;23;48]	5.023	0.00918	117
Right Planum Temporale (RPT)	[46;-33;17]	4.939	0.00947	69
Right Supramarginal Gyrus (RSG)	[51;-41;47]	4.896	0.00957	58
Left Frontal Operculum (LFO)	[-39;12;2]	4.831	0.00983	68
Right Anterior Cingulate Gyrus (RACG)	[2;47;0]	4.825	0.00987	188
Left Central Operculum (LCO)	[-37;-18;17]	4.626	0.01124	115
Left Opercular part of the Inferior Frontal Gyrus (LOPOFIFG)	[-47;9;24]	4.599	0.01148	36
Right Supplementary Motor Cortex (RSMC)	[1;-12;53]	4.489	0.01251	85
Right Middle Frontal Gyrus (RMFG)	[38;51;14]	4.425	0.01332	58
Left Thalamus Proper (LTP)	[-1;-10;12]	4.398	0.01368	88
Left Superior Frontal Gyrus Medial Segment (LSFGMS)	[-1;46;13]	4.350	0.01438	56
Right Anterior Insula (RAIns)	[33;15;-19]	4.339	0.01453	37
Left Superior Frontal Gyrus (LSFG)	[-24;20;57]	4.230	0.01646	66
Right Central Operculum (RCO)	[57;5;4]	4.014	0.02164	58
Right Middle Temporal Gyrus (RMTG)	[60;-6;-13]	3.977	0.02275	35
Right Opercular part of the Inferior Frontal Gyrus (ROPOFIFG)	[42;17;25]	3.965	0.02308	47
Right Posterior Insula (RPIns)	[36;-19;13]	3.919	0.02454	56
Left Lateral Ventricle (LLV)	[-1;1;8]	3.909	0.02489	68
Right Hippocampus (RH)	[21;-31;-6]	3.903	0.02507	35
Right Precentral Gyrus (RPreG)	[43;5;28]	3.724	0.03187	30
Right Lateral Ventricle (RLV)	[9;7;21]	3.637	0.03572	60

Table 5 Locations of the voxel-wise statistically significant differences in ADC in the whole brain for the MSC>CNT contrast, according to the Neuromorphometrics labels; t-value represents the value of the t-test's statistic; qFDR represents the FDR-corrected p-value. The details of the regions identified here belong to the clusters with higher t-value for each region and are for peak-level.

Voxel-wise differences in ADC (NAWM) MSC>CNT				
Region	**MNI coordinates [x;y;z] (mm)**	**t-value**	**qFDR**	**# voxels**
GLOBAL NAWM				
Right Cerebral White Matter (RCWM)	[38;-44;-1]	7.222	0.00318	79744
Left Postcentral Gyrus (LPG)	[-41;-36;57]	5.576	0.00333	220
Left Cerebral White Matter (LCWM)	[-6;43;46]	4.547	0.00632	254
Right Central Operculum (RCO)	[57;5;5]	3.924	0.01133	66
Right Inferior Temporal Gyrus (RITG)	[45;0;-40]	3.745	0.01359	60
Right Occipital Fusiform Gyrus (ROFG)	[29;-81;-13]	3.699	0.01425	74
Right Hippocampus (RH)	[22;-33;-7]	3.435	0.01864	216
Right Postcentral Gyrus (RPG)	[48;-26;54]	3.309	0.02131	60
INDIVIDUAL NAWM				
Left Cerebral White Matter (LCWM)	[-42;-36;-5]	7.108	0.00053	87946
Right Cerebral White Matter (RCWM)	[10;20;18]	3.639	0.00423	583
Left Cerebellum White Matter (LCumWM)	[-12;-46;-30]	3.448	0.00536	453

Table 6 Locations of the voxel-wise statistically significant differences in ADC in NAWM (global and individual) for the MSC>CNT contrast, according to the Neuromorphometrics labels; t-value represents the value of the t-test's statistic; qFDR represents the FDR-corrected p-value. The details of the regions identified here belong to the clusters with higher t-value for each region and are for peak-level.

Voxel-wise differences in ADC (Lesion Map) MSC>CNT				
Region	**MNI coordinates [x;y;z] (mm)**	**t-value**	**qFDR**	**# voxels**
Right Cerebral White Matter (LCWM)	[38;-47;0]	7.940	0.00011	93651
Left Cerebral White Matter (RCWM)	[-33;-57;34]	4.901	0.00039	414

Table 7 Locations of the voxel-wise statistically significant differences in ADC in the (global) lesion mask for the MSC>CNT contrast, according to the Neuromorphometrics labels; t-value represents the value of the t-test's statistic; qFDR represents the FDR-corrected p-value. The details of the regions identified here belong to the clusters with higher t-value for each region and are for peak-level.

Voxel-wise differences in ODI (NAWM) MSC>CNT				
Region	**MNI coordinates [x;y;z] (mm)**	**t-value**	**qFDR**	**# voxels**
GLOBAL NAWM				
Right Thalamus Proper (RTP)	[8;-20;-2]	6.652	0.0123	286
Right Putamen (RPu)	[29;14;-1]	5.192	0.0233	45
Right Cerebellum White Matter (RCumWM)	[31;-57;-44]	5.131	0.0256	24
Right Cerebral White Matter (RCWM)	[21;8;8]	4.835	0.0357	28
Left Thalamus Proper (LTP)	[-10;-20;-2]	4.805	0.0362	74
Left Cerebral White Matter (LCWM)	[-36;21;13]	4.754	0.0372	9
INDIVIDUAL NAWM				
Right Thalamus Proper (RTP)	[8;-20;-2]	6.675	0.00504	358
Right Cerebral White Matter (RCWM)	[29;15;0]	5.089	0.01794	20
Left Thalamus Proper (LTP)	[-10;-20;-2]	4.815	0.02502	172
Left Cerebellum White Matter (LCumWM)	[-21;-57;-31]	4.805	0.02550	14
Right Cerebellum White Matter (RCumWM)	[32;-56;-44]	4.702	0.02727	14
Left Cerebral White Matter (LCWM)	[-36;21;14]	4.463	0.03316	16

Table 8 Locations of the voxel-wise statistically significant differences in ODI in NAWM (global and individual) for the MSC>CNT contrast, according to the Neuromorphometrics labels; t-value represents the value of the t-test's statistic; qFDR represents the FDR-corrected p-value. The details of the regions identified here belong to the clusters with higher t-value for each region and are for peak-level.

Voxel-wise differences in NDI (Whole brain) CNT>MSC				
Region	**MNI coordinates [x;y;z] (mm)**	**t-value**	**qFDR**	**# voxels**
Right Cerebral White Matter (RCWM)	[27;-34;23]	10.260	0.00001	198964
Left Middle Temporal Gyrus (LMTG)	[-50;-54;14]	4.799	0.00090	97
Left Cerebral White Matter (LCWM)	[-55;-13;4]	4.183	0.00325	100
Right Occipital Fusiform Gyrus (ROFG)	[40;-71;-19]	3.740	0.00806	219
Left Cerebellum White Matter (LCumWM)	[-26;-59;-40]	3.702	0.00869	152
Left Cerebellum Exterior (LCE)	[-19;-55;-26]	3.687	0.00895	324
Right Cerebellum White Matter (RCumWM)	[13;-35;-39]	3.589	0.01086	296
Right Hippocampus (RH)	[25;-36;-6]	3.325	0.01805	152
Right Cerebellum Exterior (RCE)	[7;-58;-20]	3.237	0.02131	84

Table 9 Locations of the voxel-wise statistically significant differences in NDI in the whole brain for the CNT>MSC contrast, according to the Neuromorphometrics labels; t-value represents the value of the t-test's statistic; qFDR represents the FDR-corrected p-value. The details of the regions identified here belong to the clusters with higher t-value for each region and are for peak-level.

Voxel-wise differences in NDI (NAWM) CNT>MSC				
Region	**MNI coordinates [x;y;z] (mm)**	**t-value**	**qFDR**	**# voxels**
GLOBAL NAWM				
Right Cerebral White Matter (RCWM)	[26;-33;23]	9.863	0.00001	139490
Right Cerebellum White Matter (RCumWM)	[31;-51;-41]	3.885	0.00322	2783
Left Cerebellum White Matter (LCumWM)	[-26;-59;-40]	3.781	0.00387	1283
Left Cerebellum Exterior (LCE)	[-17;-54;-25]	3.775	0.00391	960
Left Lingual Gyrus (LLG)	[-4;-86;-6]	3.396	0.00747	190
Right Cerebellum Exterior (RCE)	[7;-58;-20]	3.362	0.00790	433
Left Cerebral White Matter (LCWM)	[-42;27;11]	3.098	0.01240	138
INDIVIDUAL NAWM				
Right Cerebral White Matter (RCWM)	[15;-43;9]	9.048	0.00001	95015
Right Cerebellum White Matter (RCumWM)	[31;-51;-41]	3.897	0.00159	2957
Left Cerebellum White Matter (LCumWM)	[-26;-59;-40]	3.781	0.00196	1648

Table 10 Locations of the voxel-wise statistically significant differences in NDI in NAWM (global and individual) for the CNT>MSC contrast, according to the Neuromorphometrics labels; t-value represents the value of the t-test's statistic; qFDR represents the FDR-corrected p-value. The details of the regions identified here belong to the clusters with higher t-value for each region and are for peak-level.

Voxel-wise differences in NDI (Lesion Map) CNT>MSC				
Region	**MNI coordinates [x;y;z] (mm)**	**t-value**	**qFDR**	**# voxels**
Right Cerebral White Matter (LCWM)	[27;-34;23]	10.485	3.08E-07	108947

Table 11 Locations of the voxel-wise statistically significant differences in NDI in the (global) lesion mask for the CNT>MSC contrast, according to the Neuromorphometrics labels; t-value represents the value of the t-test's statistic; qFDR represents the FDR-corrected p-value. The details of the regions identified here belong to the clusters with higher t-value for each region and are for peak-level.

4.6. Summary statistics of the means

Table 12 and the boxplots in Fig. 14 (A-D) show the mean and the standard deviation (SD) for each diffusion metric and each tissue; Fig. 14 also shows the median and each point represents one participant, either patient or healthy control.

Summary statistics for tissues of interest

	mean	sd
FA_WM	4.07E-01	1.35E-02
FA_NAWM	3.83E-01	1.59E-02
FA_LES	3.86E-01	2.74E-02
ADC_WM	5.88E-04	1.48E-05
ADC_NAWM	6.08E-04	1.69E-05
ADC_LES	1.14E-03	8.68E-05
ODI_WM	3.20E-01	7.76E-03
ODI_NAWM	3.25E-01	9.68E-03
ODI_LES	2.90E-01	1.87E-02
NDI_WM	5.59E-01	1.86E-02
NDI_NAWM	5.29E-01	2.22E-02
NDI_LES	5.85E-01	3.02E-02

Table 12 Mean and SD for each parameter (FA, ADC, ODI and NDI), in each tissue of interest (NAWM, WM and lesions).

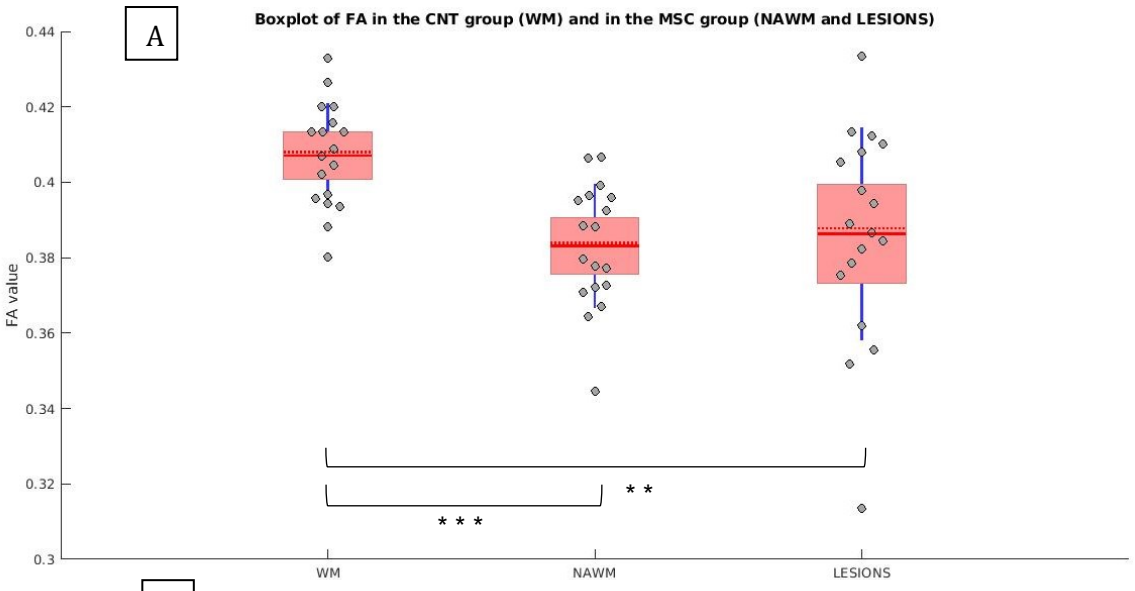
A
Boxplot of FA in the CNT group (WM) and in the MSC group (NAWM and LESIONS)
FA value
0.44
0.42
0.4
0.38
0.36
0.34
0.32
0.3
* * *
* *
WM
NAWM
LESIONS

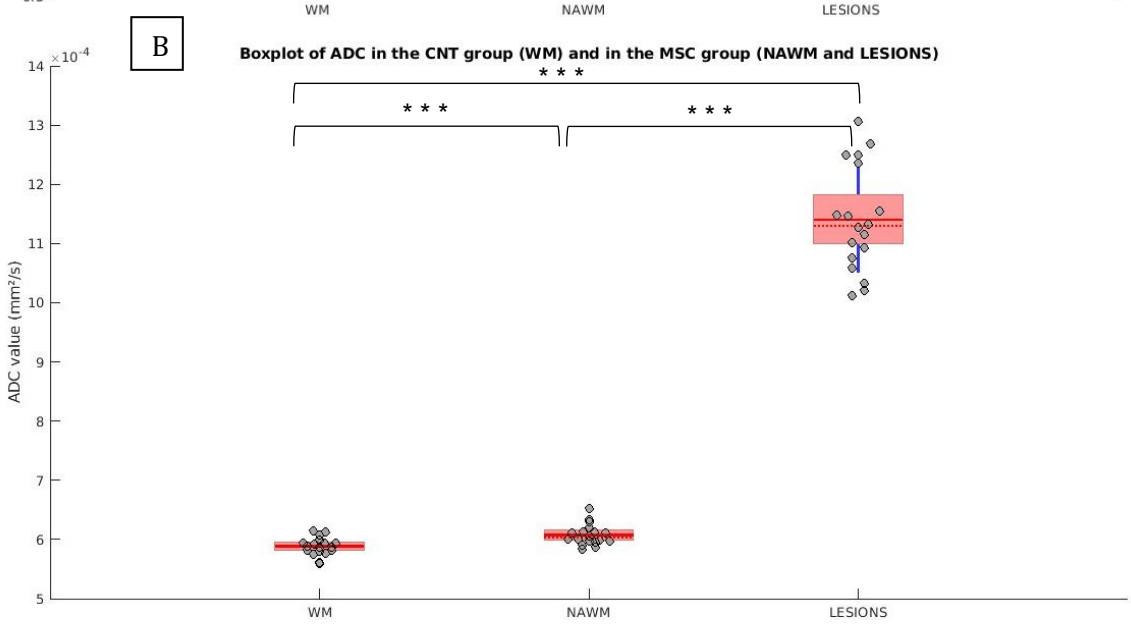
B
Boxplot of ADC in the CNT group (WM) and in the MSC group (NAWM and LESIONS)
×10⁻⁴
ADC value (mm²/s)
14
13
12
11
10
9
8
7
6
5
* * *
* * *
* * *
WM
NAWM
LESIONS

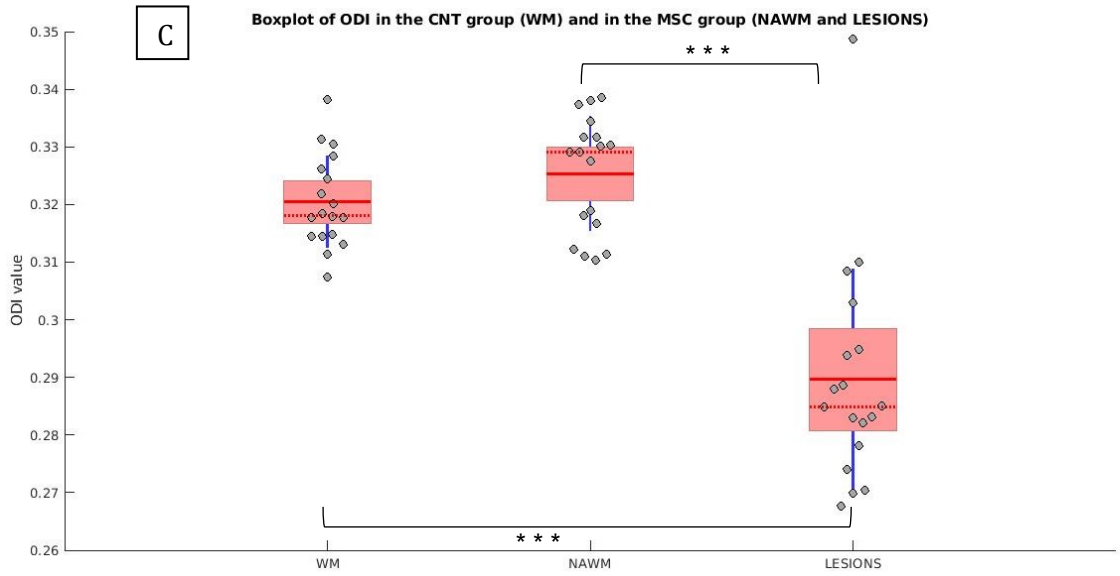
C
Boxplot of ODI in the CNT group (WM) and in the MSC group (NAWM and LESIONS)
ODI value
0.35
0.34
0.33
0.32
0.31
0.3
0.29
0.28
0.27
0.26
* * *
* * *
WM
NAWM
LESIONS

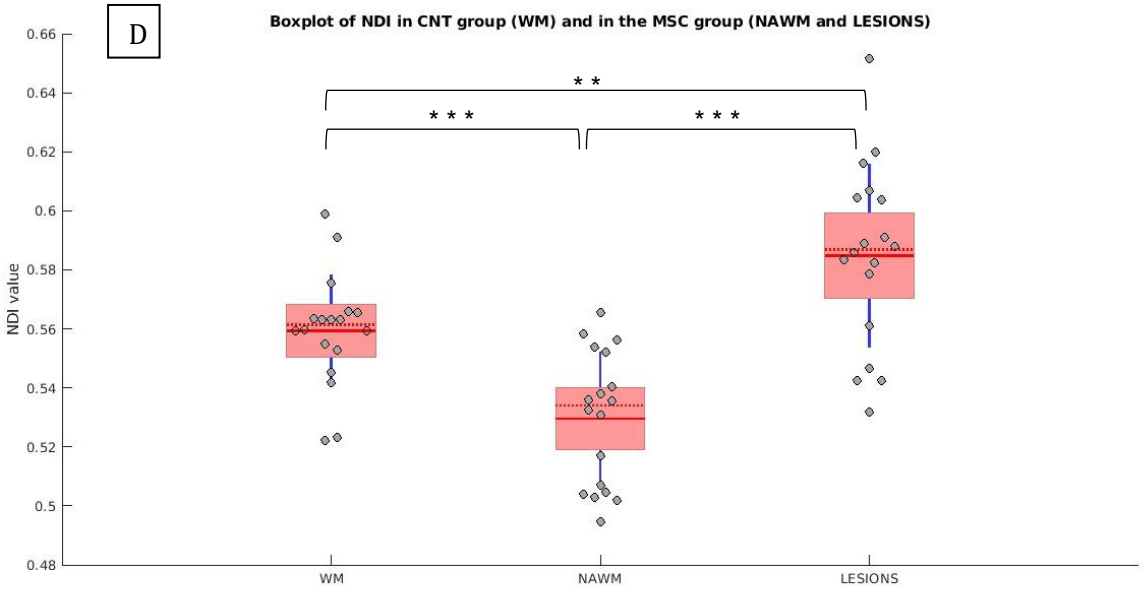

Fig. 14 Boxplots of DTI (A,B) and NODDI (C,D) metrics; each figure has three boxplots, each computed with the means from the participants (MSC group in NAWM and lesions and CNT group in WM), with each point representing this measure for each participant; the mean is the full red line, while the median is the dotted red line. The standard deviation is represented by the blue line, whereas the red area is the 95% confidence interval. The black lines between boxplots represent statistically significant differences, with the number of asterisks representing the p-value (* p<0.05; ** p<0.01; *** p<0.001).

The results for the statistical analysis of the means are summarised in Table . Each entry in the table is the p-value for each comparison, which has an asterisk or more if it is lower than the significance value 0.05, and thus the null hypothesis that the means are the same is rejected. By combining the results from both Table 12 and Table 13 it can be seen that, in MS patients: FA is decreased in NAWM and lesions; ADC is increased in NAWM and lesions; ODI is decreased in lesions; NDI is increased in lesions and decreased in NAWM.

p-values for comparisons of the means in tissues of interest			
	WM VS NAWM	**WM VS LESIONS**	**NAWM VS LESIONS**
FA	3.71E-05***	0.0097**	0.6774
ADC	9.68E-04***	1.11E-15***	3.86E-15***
ODI	0.1139	2.21E-06***	2.65E-06***
NDI	1.58E-04***	0.0063**	1.68E-07***

Table 13 p-values of the statistical analysis (comparisons) performed on the means in tissues of interest. Asterisks represent statistically significant p-values (** p<0.01; *** p<0.001).

4.7. Correlations with clinical scores

In tissues of interest, the only statistically significant correlation found was between ODI in NAWM and MFIS, with an r of 0.528 and a p-value of 0.0242; this correlation is represented by the scatter plot and the least squares line seen on Fig. 15.

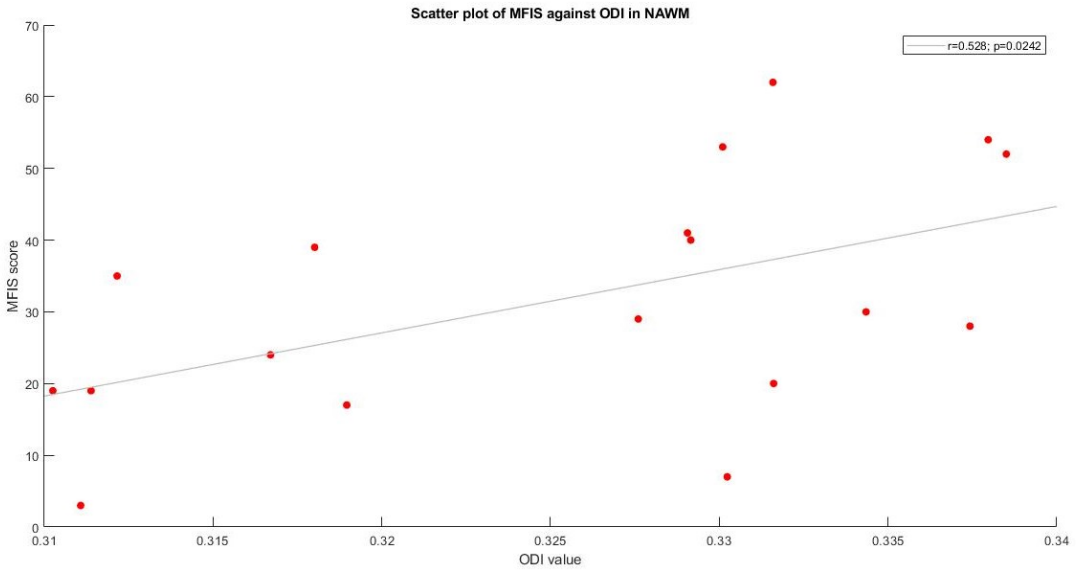

Fig. 15 Scatter plot of the MFIS score against ODI values in NAWM. The grey line represents a least squares line, which is used by Pearson's correlation to describe the relationship between the two variables as linearly dependent.

For the correlations between ROIs and clinical scores, the detailed statistically significant (uncorrected p-value<0.05) results can be found in Table 14, Table 15, Table 16, Table 17, Table 18, and Table 19 in Annex D. For better visualising these correlations, the ROIs with statistically significant correlations were overlaid on the considered atlas. In each figure, the coloured ROIs are numbered (those showing significant correlations), and the legend is on the right; if the ROI remained statistically significant after FDR correction, that fact is indicated by an asterisk next to the abbreviation. Note that since there is only one slice displayed for each view (axial, sagittal and coronal) not all ROIs are visible.

FA and EDSS were correlated in 13 ROIs, with negative correlations in 10 and positive in 3; when FDR correction was applied, only one ROI remained statistically significant (see FA column in Table 14 of Annex D). The highest positive correlation was found in the Right Accumbens Area (RAA) (rho of 0.769; remained statistically significant after FDR correction) and the highest negative correlation was found in the Left Fusiform Gyrus (LFG) (rho of -0.640). ADC and EDSS showed associations in 7 ROIs, all with positive correlations; none of these survived FDR correction (see ADC column in Table 14 of Annex D). The highest correlation was found in LCE, with a rho of 0.666. ODI and EDSS showed negative correlations in 6 ROIs, and a positive correlation in 1 ROI (see ODI column in Table 14 of Annex D). The maximum positive correlation was in the Left Calcarine Cortex (LCC)

(rho = 0.520), whereas the highest negative one was in LC (rho=-0.666). All correlations (5 ROIs) between NDI and EDSS were negative (see NDI column in Table 14 of Annex D); the highest correlation was for the Right Basal Forebrain (RBF) (rho of -0.619). These results are displayed in Fig. 16 (EDSS and FA), Fig. 17 (EDSS and ADC), Fig. 18 (EDSS and ODI) and Fig. 19 (EDSS and NDI).

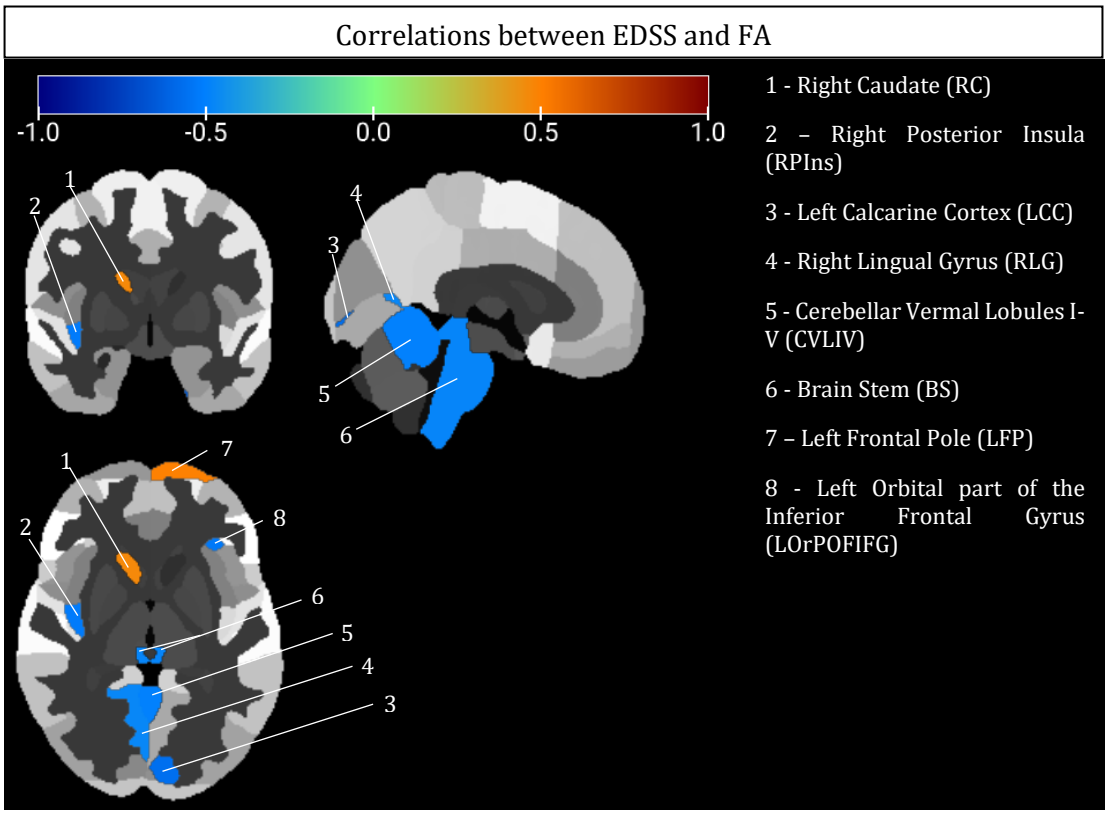

Fig. 16 ROIs with correlations between EDSS and FA. The ROIs are overlaid on the Neuromorphometrics atlas, and the displayed slices have coordinates 0,0,0 mm in the MNI space. The colourbar represents the strength of the correlation; note that blue-ish colours represent negative correlations, while red-ish ones indicate positive correlations

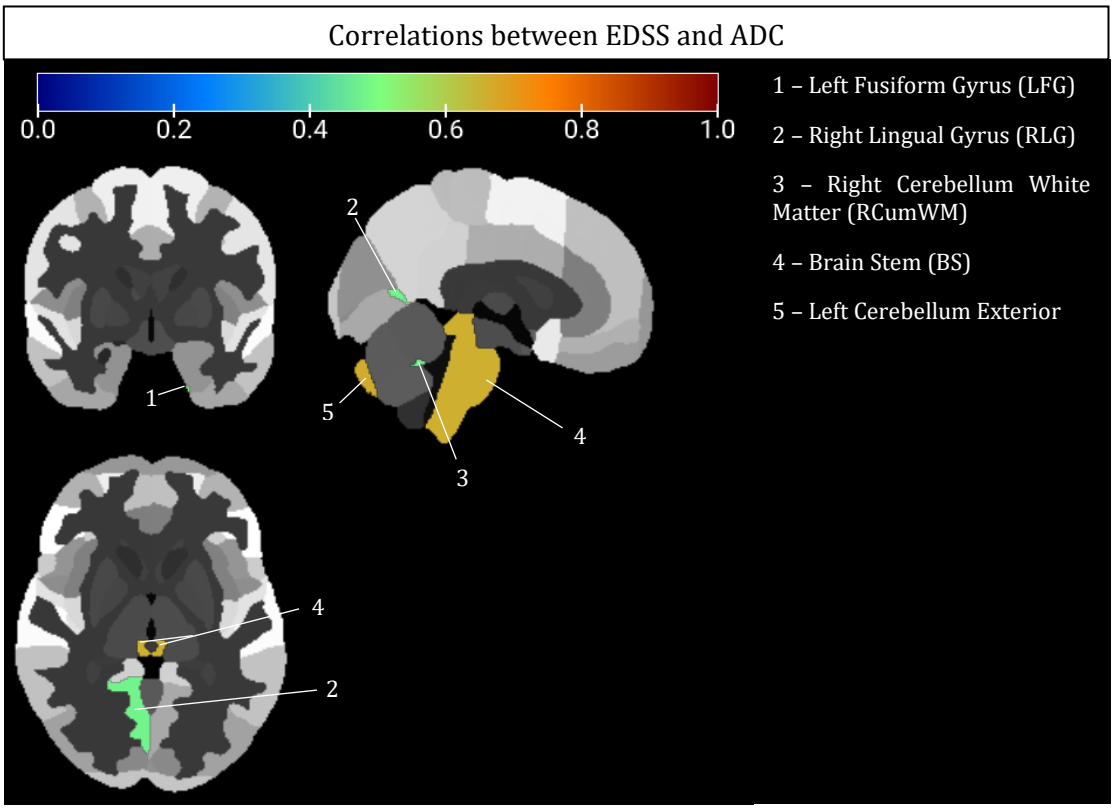

Fig. 17 ROIs with correlations between EDSS and ADC. The ROIs are overlaid on the Neuromorphometrics atlas, and the displayed slices have coordinates 0,0,0 mm in the MNI space. The colourbar represents the strength of the correlation; note that there are only positive correlations.

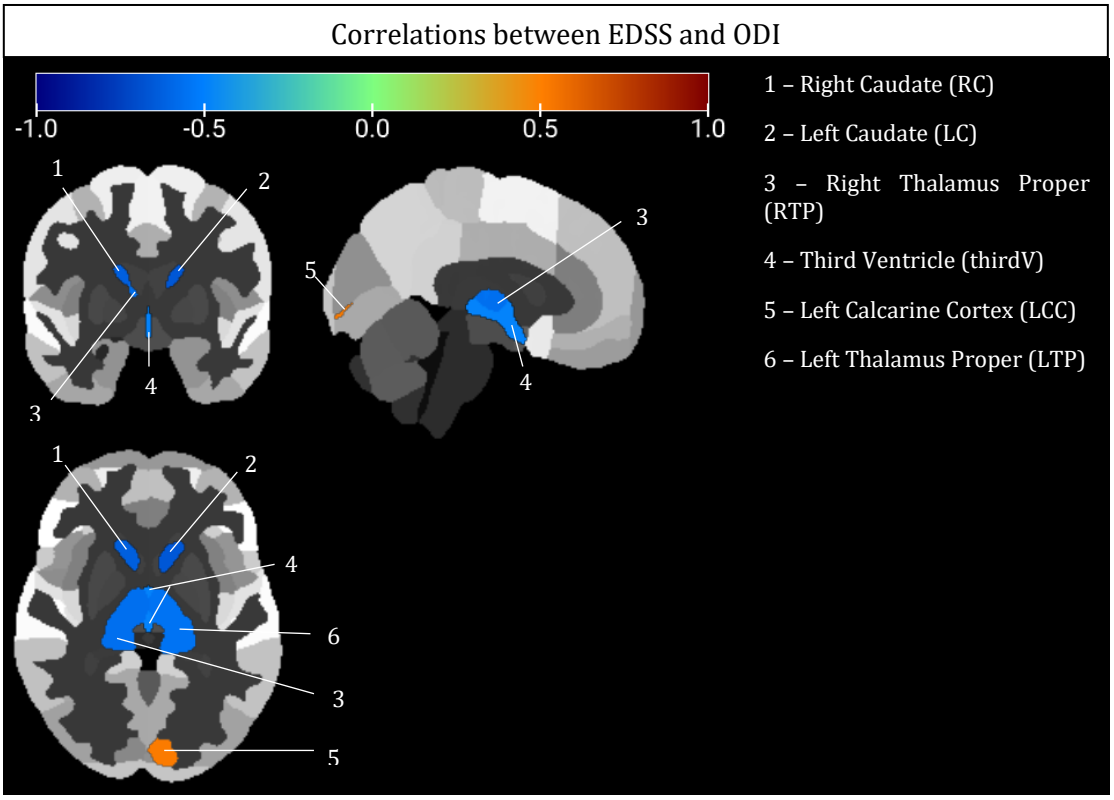

Fig. 18 ROIs with correlations between EDSS and ODI. The ROIs are overlaid on the Neuromorphometrics atlas, and the displayed slices have coordinates 0,0,0 mm in the MNI space. The colourbar represents the strength of the correlation; note that blue-ish colors represent negative correlations, while red-ish ones indicate positive correlations.

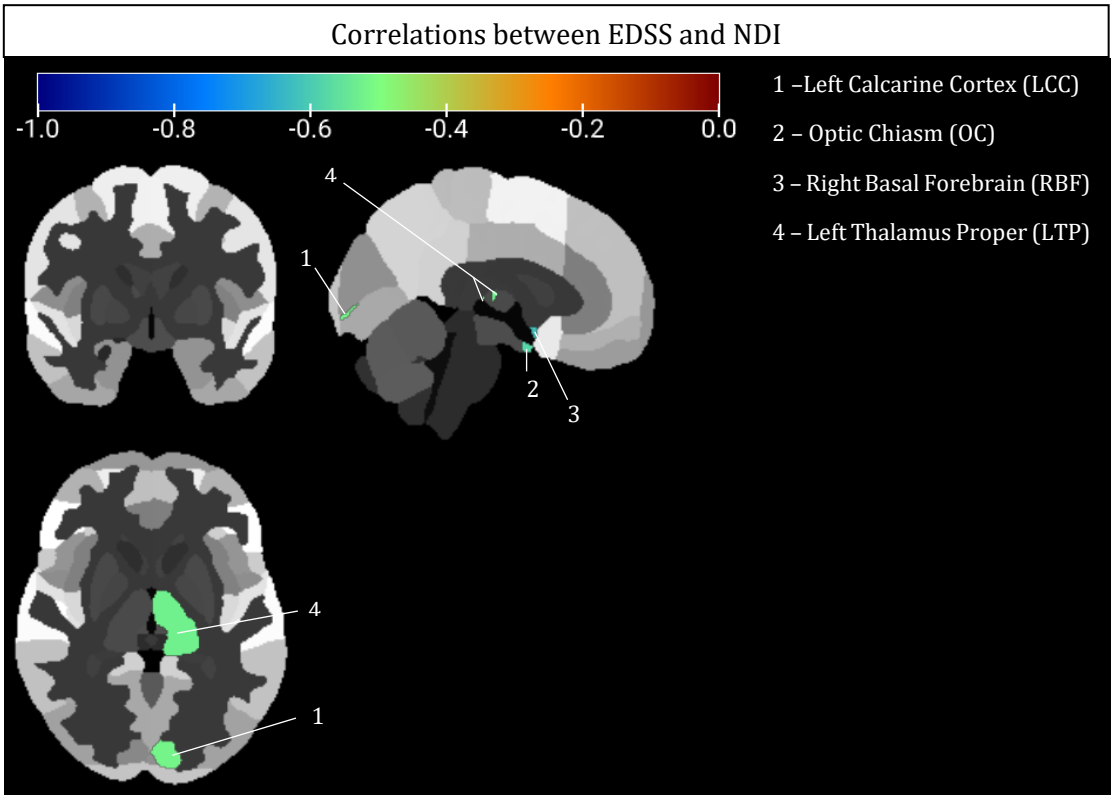

Fig. 19 with correlations between EDSS and NDI. The ROIs are overlaid on the Neuromorphometrics atlas, and the displayed slices have coordinates 0,0,0 mm in the MNI space. The colourbar represents the strength of the correlation; note that there are only negative correlations.

FA and MFIS were inversely correlated in all 9 statistically significant ROIs (see FA column in Table 15 of Annex D) with no multiple comparisons' correction. Once FDR correction was employed, no ROIs survived. For these correlations, the higher had an r of -0.555 and was in the Left Subcallosal Area (LSA). ADC and MFIS showed correlations in only 2 ROIs, all positive, and with none surviving the FDR correction (see ADC column in Table 15 of Annex D); the highest correlation was in the Left Posterior Orbital Gyrus (LPOrG) (r=0.508). ODI was the metric that showed more correlations with MFIS (all positive): a total of 18 ROIs, with two of them surviving the multiple comparisons' correction (see ODI column in Table 15 of Annex D). One of the ROIs that survived FDR correction was the Right Fusiform Gyrus (RFG), and this was the region with higher correlation coefficient (r=0.721). Finally, correlations between NDI and MFIS were found in 4 ROIs, all of them were positive and none survived the FDR correction (see NDI column in Table 15 of Annex D). The highest correlation was in the Right Transverse Temporal Gyrus (RTTG), with an r of 0.726. These results can be viewed on Fig. 20 (MFIS and FA), Fig. 21 (MFIS and ADC), Fig. 22 (MFIS and ODI) and on Fig. 23 (MFIS and NDI).

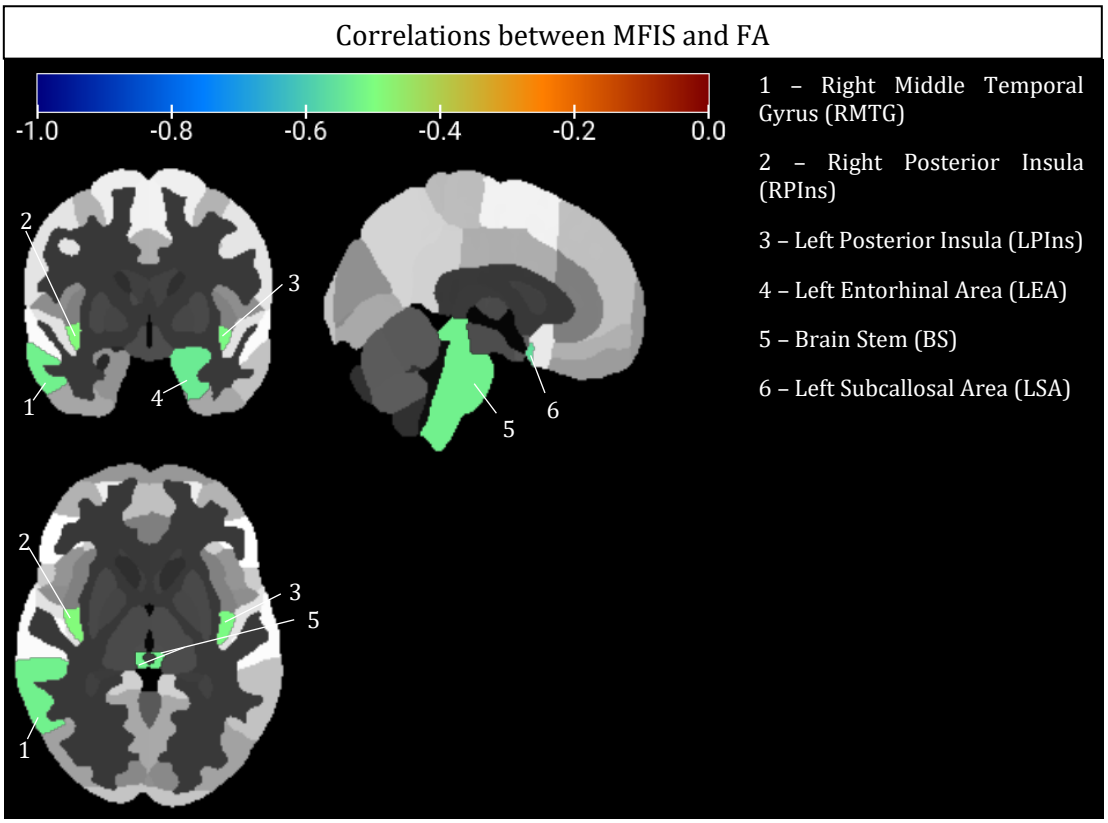

Fig. 20 ROIs with correlations between MFIS and FA. The ROIs are overlaid on the Neuromorphometrics atlas, and the displayed slices have coordinates 0,0,0 mm in the MNI space. The colourbar represents the strength of the correlation; note that there are only negative correlations.

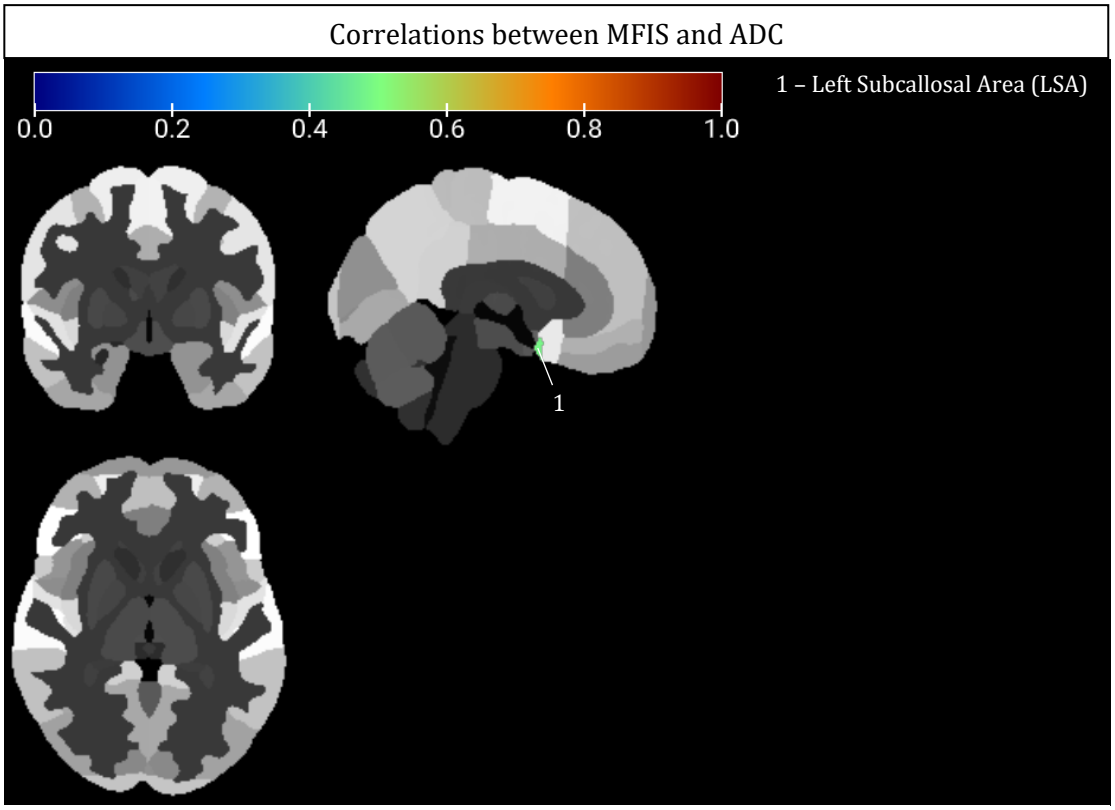

Fig. 21 ROIs with correlations between MFIS and ADC. The ROIs are overlaid on the Neuromorphometrics atlas, and the displayed slices have coordinates 0,0,0 mm in the MNI space. The colourbar represents the strength of the correlation; note that there are only positive correlations.

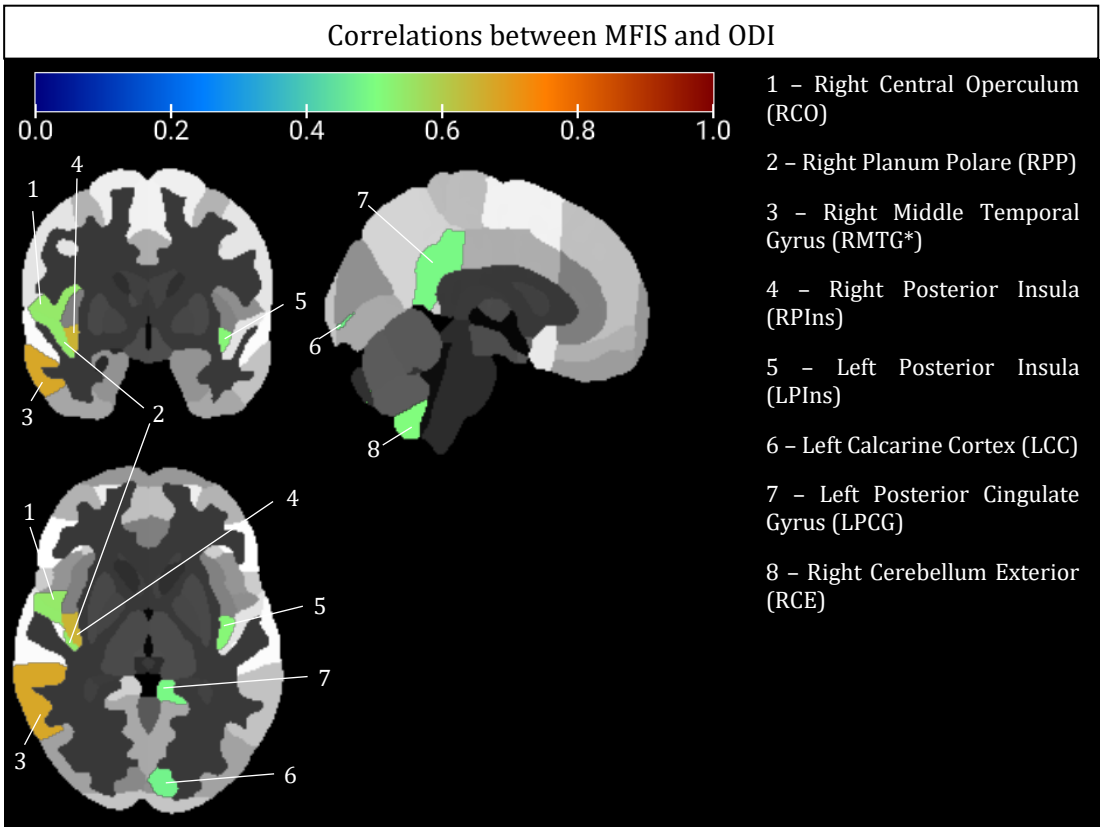

Fig. 22 ROIs with correlations between MFIS and ODI. The ROIs are overlaid on the Neuromorphometrics atlas, and the displayed slices have coordinates 0,0,0 mm in the MNI space. The colourbar represents the strength of the correlation; note that there are only positive correlations. Asterisks show statistically significant correlations with an FDR-corrected p-value lower than 0.05.

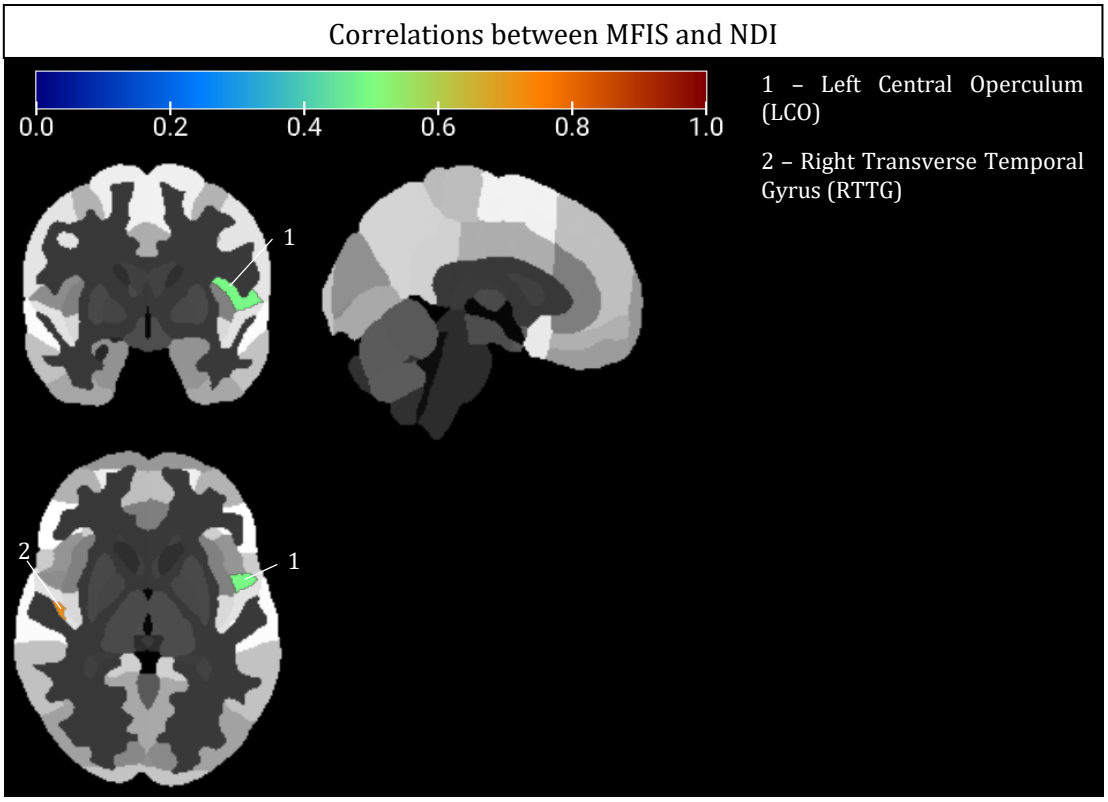

Fig. 23 ROIs with correlations between MFIS and NDI. The ROIs are overlaid on the Neuromorphometrics atlas, and the displayed slices have coordinates 0,0,0 mm in the MNI space. The colourbar represents the strength of the correlation; note that there are only positive correlations.

SDMT and FA were positively correlated in 14 ROIs and negatively correlated in one (see FA column in Table 16 of Annex D). The highest positive correlation was in LSMC, with an r of 0.70; the only negative correlation was in the Right Middle Occipital Gyrus (RMOG) and had an r of -0.483. 12 ROIs showed correlations between SDMT and ADC, with 10 having negative associations, 2 having positive associations, and none of them remaining significative after FDR correction (see ADC column in Table 16 of Annex D). For the negative correlations, the highest was in LSMC (r -0.634) and for the positive, it was in the Left Accumbens Area (LAA) (r=0.644). ODI showed a negative correlation with SDMT in all the 17 statistically significant ROIs (see ODI column in Table 16 in Annex D), for an uncorrected p-value (no ROIs were considered as statistically significant for the FDR-corrected p-value). The highest correlation was found in the Left Anterior Insula (LAIns), with r=-0.631. Lastly, NDI was the only metric that showed significant ROIs after FDR correction. All 32 ROIs previously identified as significant remained as such and presented negative correlations between NDI and SDMT (see NDI column in Table 16 of Annex D). Thus, the higher correlation was for RACG, with r=-0.744. These results are represented in Fig. 24 (SDMT and FA), Fig. 25 (SDMT and ADC), Fig. 26 (SDMT and ODI) and in Fig. 27 (SDMT and NDI).

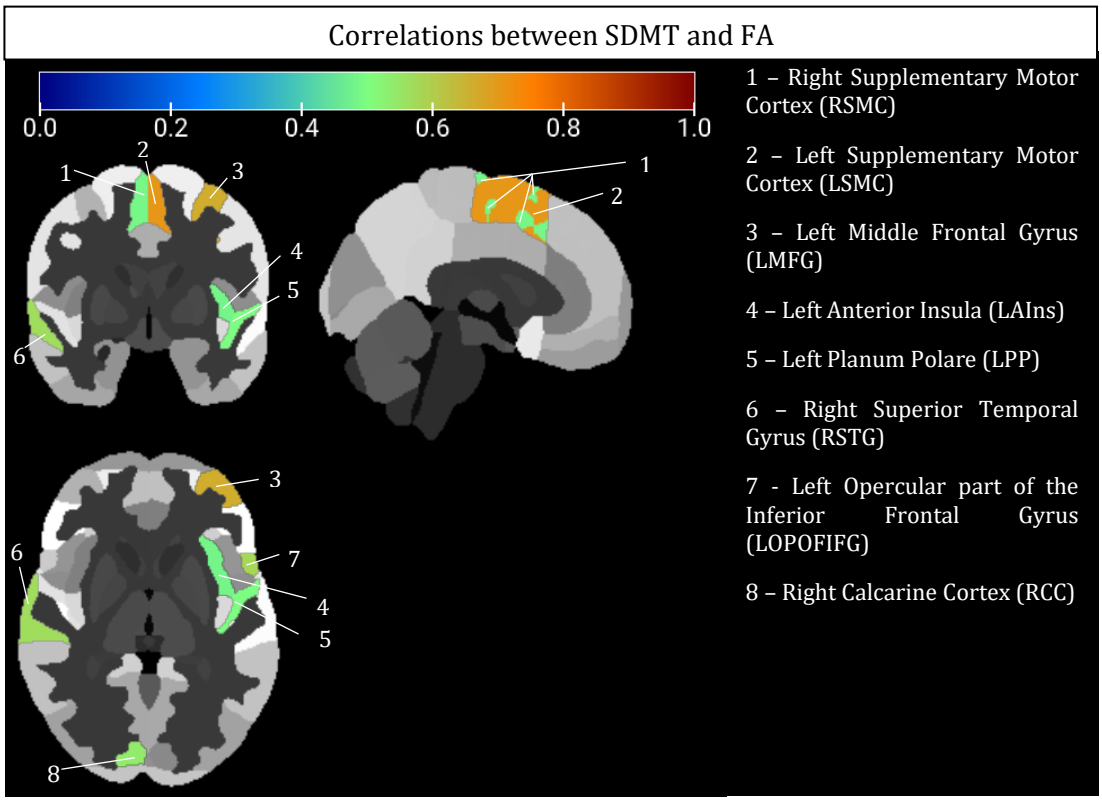

Fig. 24 ROIs with correlations between SDMT and FA. The ROIs are overlaid on the Neuromorphometrics atlas, and the displayed slices have coordinates 0,0,0 mm in the MNI space. The colourbar represents the strength of the correlation; note that there are only positive correlations.

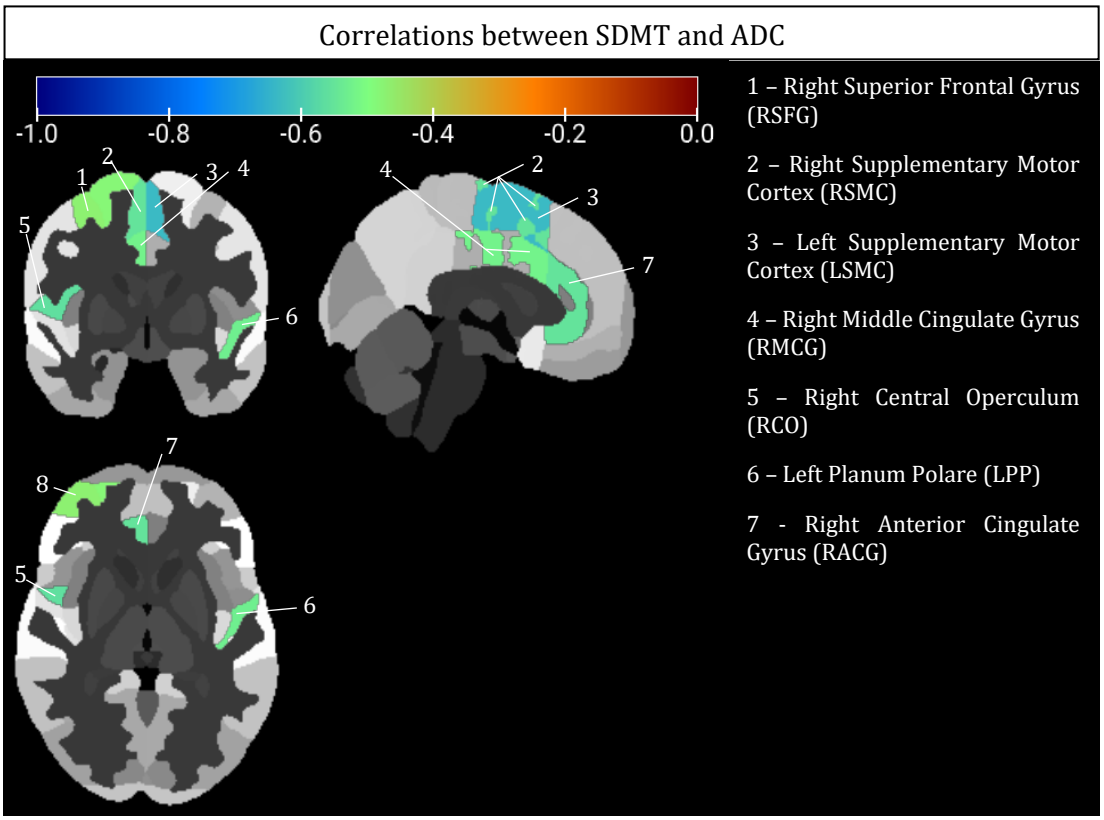

Fig. 25 ROIs with correlations between SDMT and ADC. The ROIs are overlaid on the Neuromorphometrics atlas, and the displayed slices have coordinates 0,0,0 mm in the MNI space. The colourbar represents the strength of the correlation; note that there are only negative correlations.

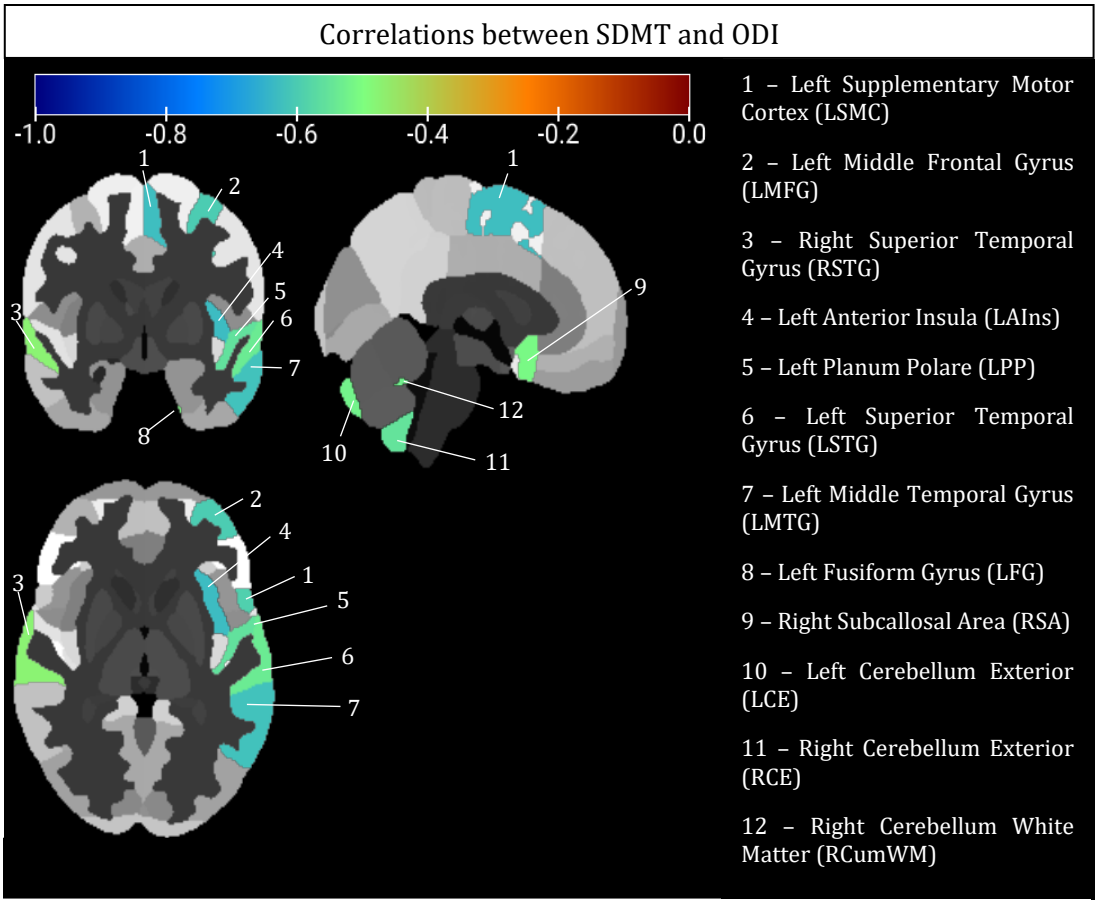

Fig. 26 ROIs with correlations between SDMT and ODI. The ROIs are overlaid on the Neuromorphometrics atlas, and the displayed slices have coordinates 0,0,0 mm in the MNI space. The colourbar represents the strength of the correlation; note that there are only negative correlations.

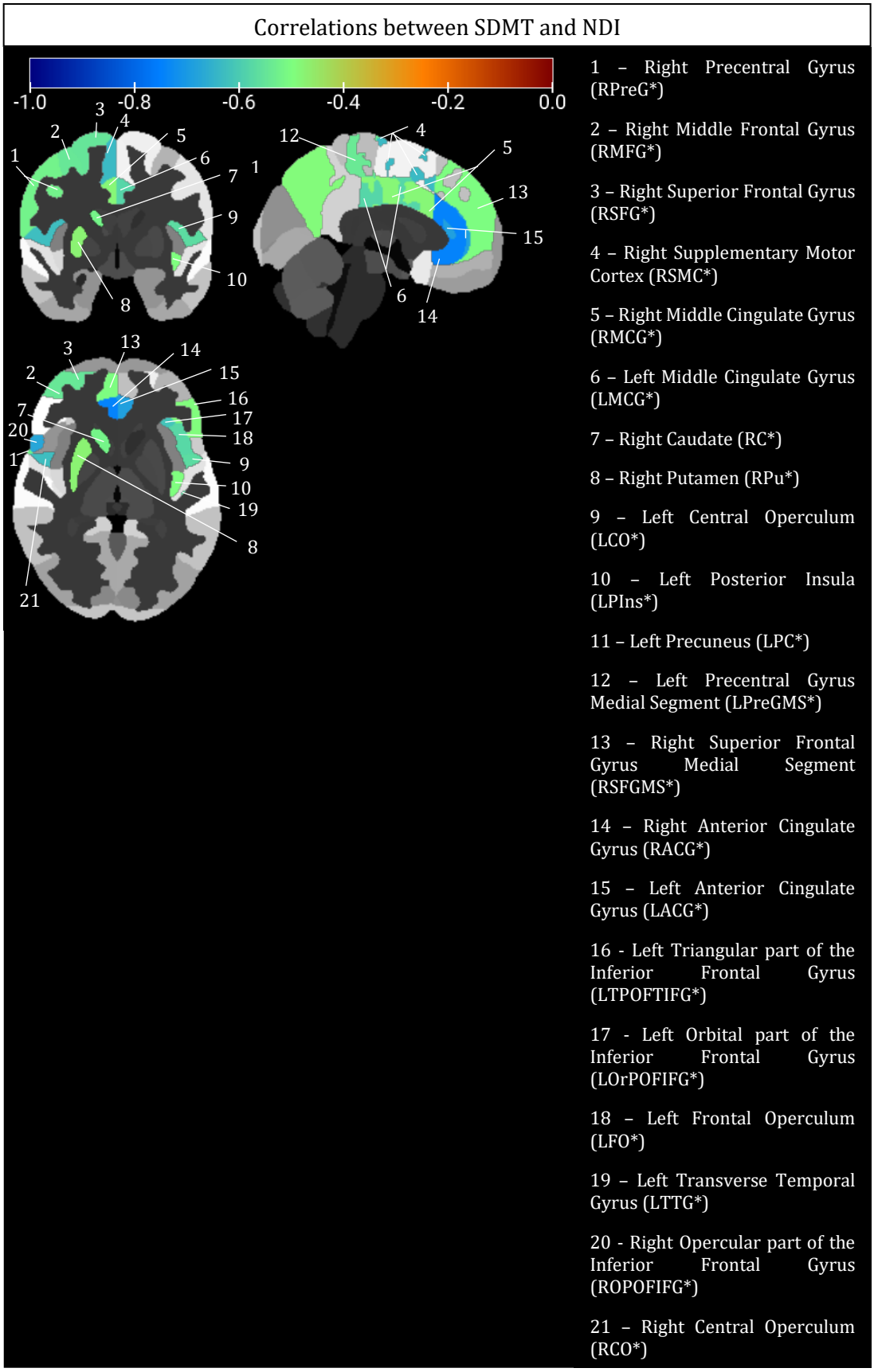

Fig. 27 ROIs with correlations between SDMT and NDI. The ROIs are overlaid on the Neuromorphometrics atlas, and the displayed slices have coordinates 0,0,0 mm in the MNI space. The colourbar represents the strength of the correlation; note that there are only negative correlations. Asterisks show statistically significant correlations with an FDR-corrected p-value lower than 0.05.

Correlations between CVLT and FA were all positive, present in 4 ROIs, and none of them was statistically significant when FDR correction was applied (see FA column in Table 17 of Annex D). In this case, the highest correlation was for Left Gyrus Rectus (LGR), with an r of 0.567. ADC and CVLT were negatively correlated in 4 of the 5 ROIs found to be statistically significant (the highest correlation was for CSF, with r=-0.557); the fifth ROI presented a positive correlation, with an r of 0.586 (the ROI was the Left Amygdala - LAm) (see ADC column in Table 17 of Annex D). However, none of them survived FDR correction. ODI and CVLT were inversely correlated in all 10 ROIs, which were statistically significant only for non-corrected p-values (see ODI column in Table 17 of Annex D). The highest association was found in LPP, with r=-0.586. NDI and CVLT showed negative correlations in 16 ROIs, and these ROIs did not remain statistically significant after FDR correction (see NDI column in Table 17 of Annex D); the Left Orbital part of the Inferior Frontal Gyrus (LOrPOFIFG) was the ROI with the highest correlation (r=-0.627). These findings are illustrated in Fig. 28 (CVLT and FA), Fig. 29 (CVLT and ADC), Fig. 30 (CVLT and ODI), and in Fig. 31 (CVLT and NDI).

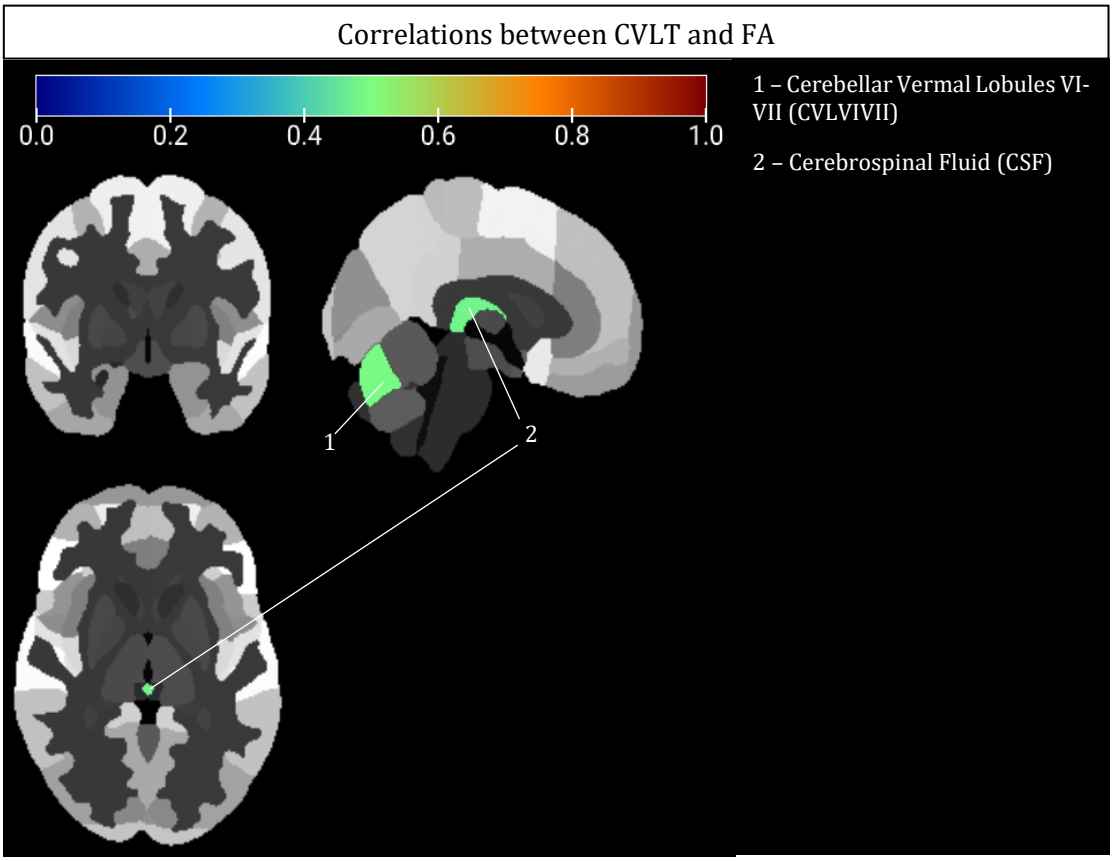

Fig. 28 ROIs with correlations between CVLT and FA. The ROIs are overlaid on the Neuromorphometrics atlas, and the displayed slices have coordinates 0,0,0 mm in the MNI space. The colourbar represents the strength of the correlation; note that there are only positive correlations.

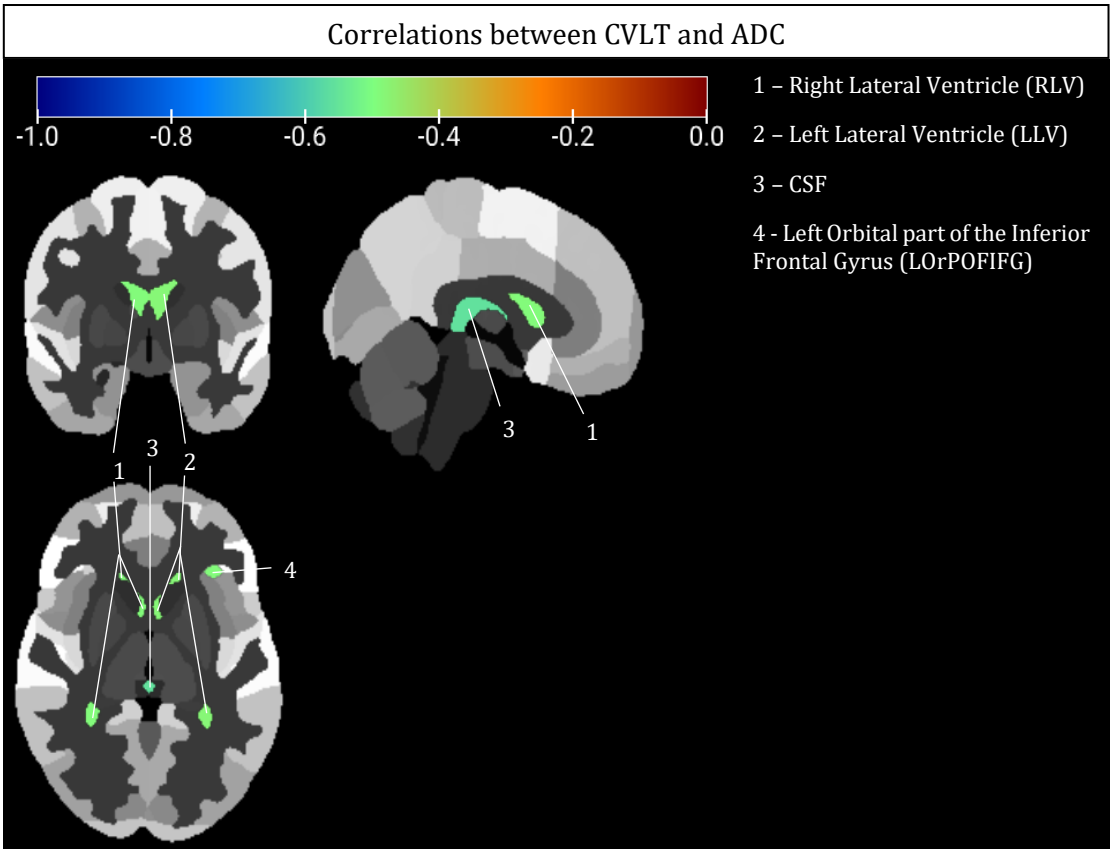

Fig. 29 ROIs with correlations between CVLT and ADC. ROIs are overlaid on the Neuromorphometrics atlas, and the displayed slices have coordinates 0,0,0 mm in the MNI space. The colourbar represents the strength of the correlation; note that there are only negative correlations.

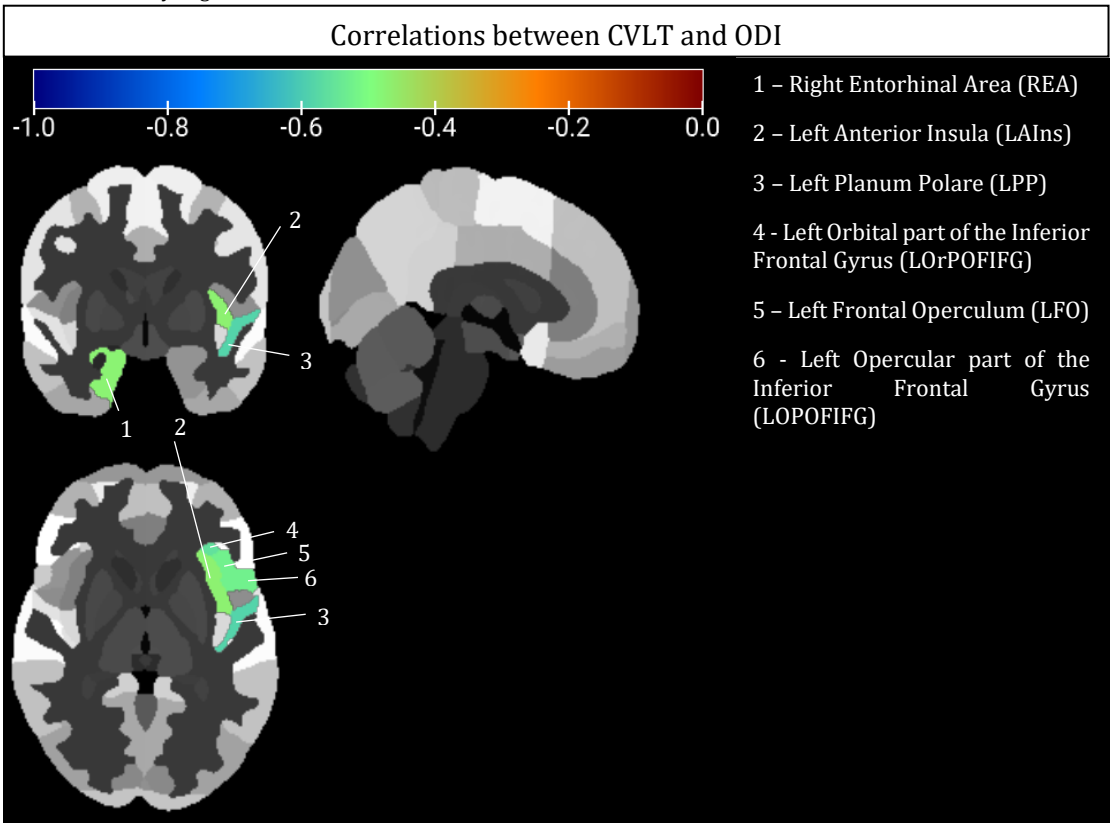

Fig. 30 ROIs with correlations between CVLT and ODI. The ROIs are overlaid on the Neuromorphometrics atlas, and the displayed slices have coordinates 0,0,0 mm in the MNI space. The colourbar represents the strength of the correlation; note that there are only negative correlations.

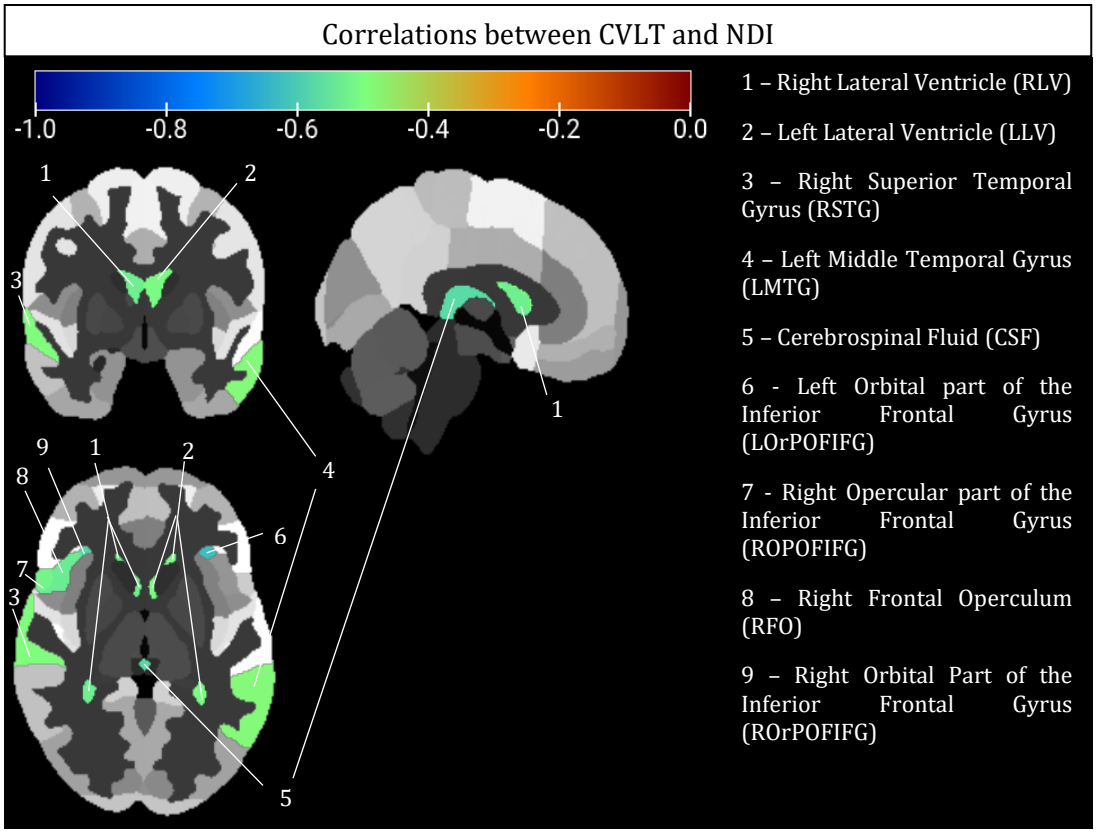

Fig. 31 ROIs with correlations between CVLT and NDI. The ROIs are overlaid on the Neuromorphometrics atlas, and the displayed slices have coordinates 0,0,0 mm in the MNI space. The colourbar represents the strength of the correlation; note that there are only negative correlations.

BVMT and FA were positively correlated in 11 ROIs, with none surviving FDR correction (see FA column in Table 18 of Annex D); the maximum correlation was 0.723, in LSMC. For BVMT and ADC, 11 statistically significant ROIs showed negative correlations, but one ROI showed a positive one (r=0.618, in RAA) (see ADC column in Table 18 of Annex D); the strongest negative correlation was in LSMC, with r=-0.678. Again, none of these were significant after an FDR correction. 22 ROIs showed statistically significant correlations between BVMT and ODI, all of them negative, and none of them remained significant after FDR correction (see ODI column of Table 18 in Annex D). The highest correlation was in LAIns, with r -0.675. NDI was the metric that showed more correlations with BVMT. There were 35 statistically significant ROIs, with 15 remaining significant after FDR correction (see NDI column in Table 18 of Annex D), all negative. The strongest correlation was in LACG, with an r of -0.701. These can be seen in Fig. 32 (BVMT and FA), Fig. 33 (BVMT and ADC), Fig. 34 (BVMT and ODI), and in Fig. 35 (BVMT and NDI).

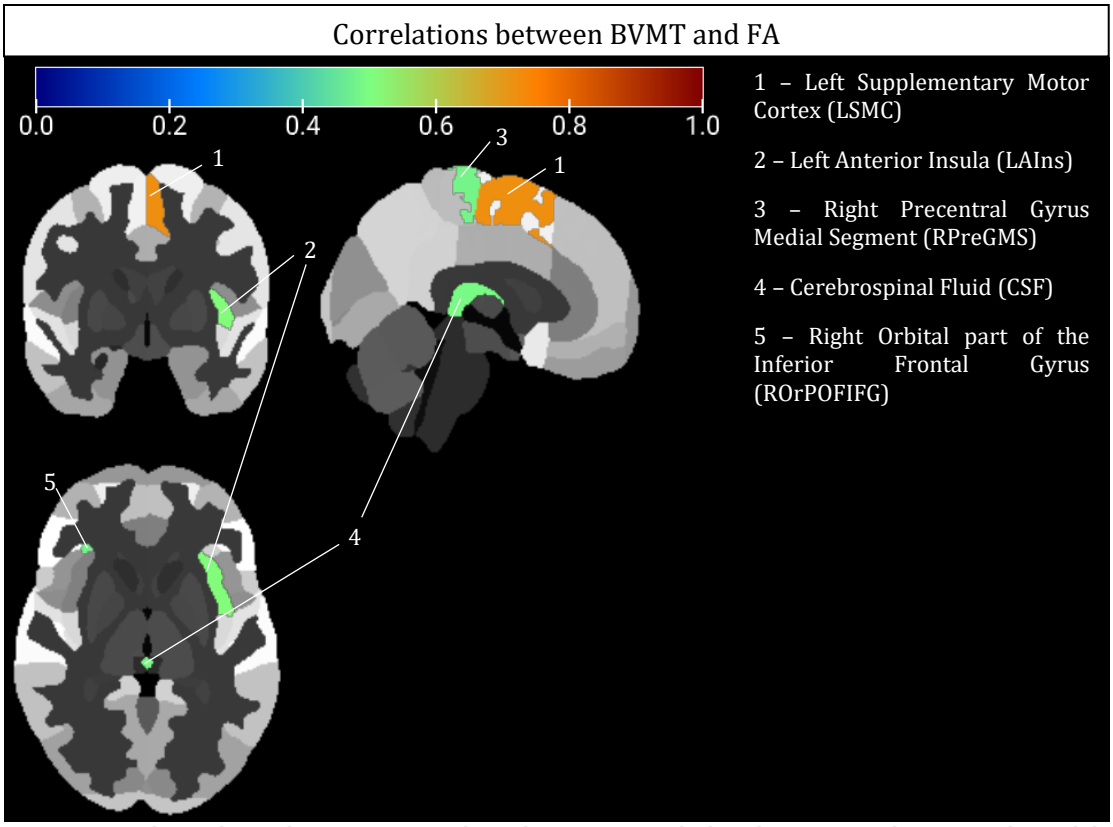

Fig. 32 ROIs with correlations between BVMT and FA. The ROIs are overlaid on the Neuromorphometrics atlas, and the displayed slices have coordinates 0,0,0 mm in the MNI space. The colourbar represents the strength of the correlation; note that there are only positive correlations.

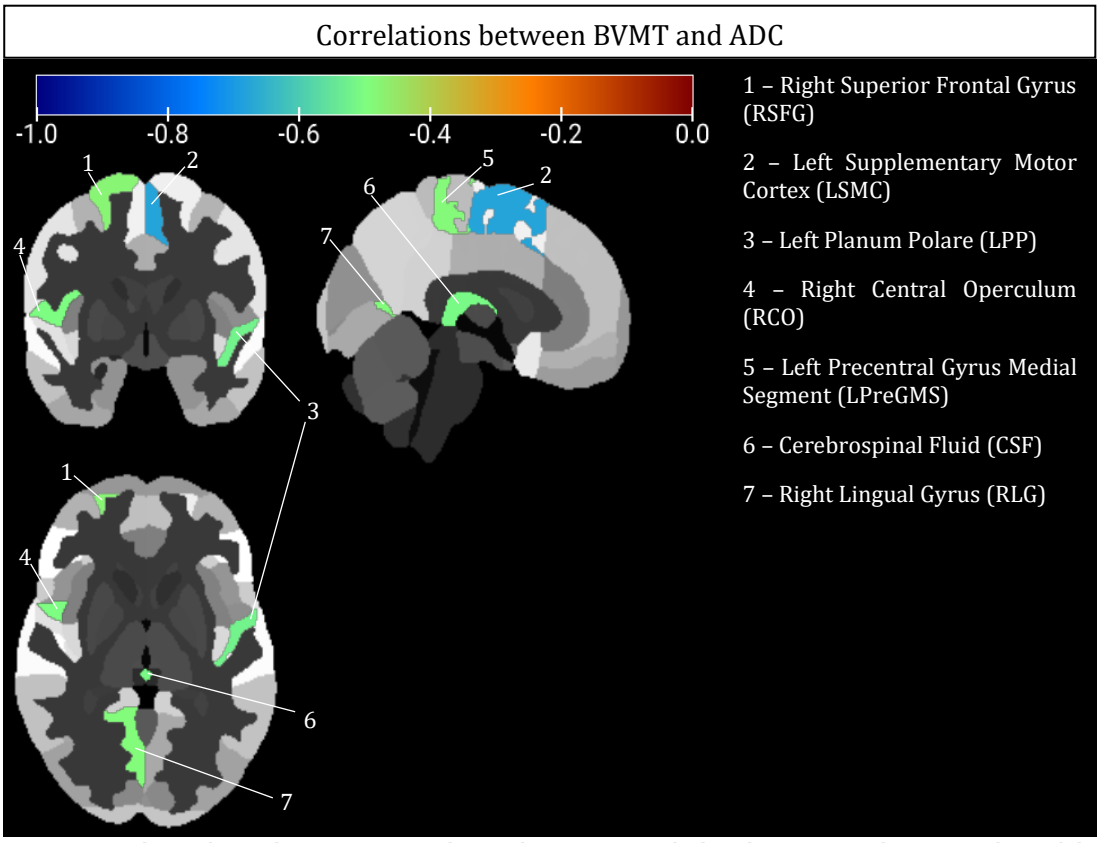

Fig. 33 ROIs with correlations between BVMT and ADC. The ROIs are overlaid on the Neuromorphometrics atlas, and the displayed slices have coordinates 0,0,0 mm in the MNI space. The colourbar represents the strength of the correlation; note that there are only negative correlations.

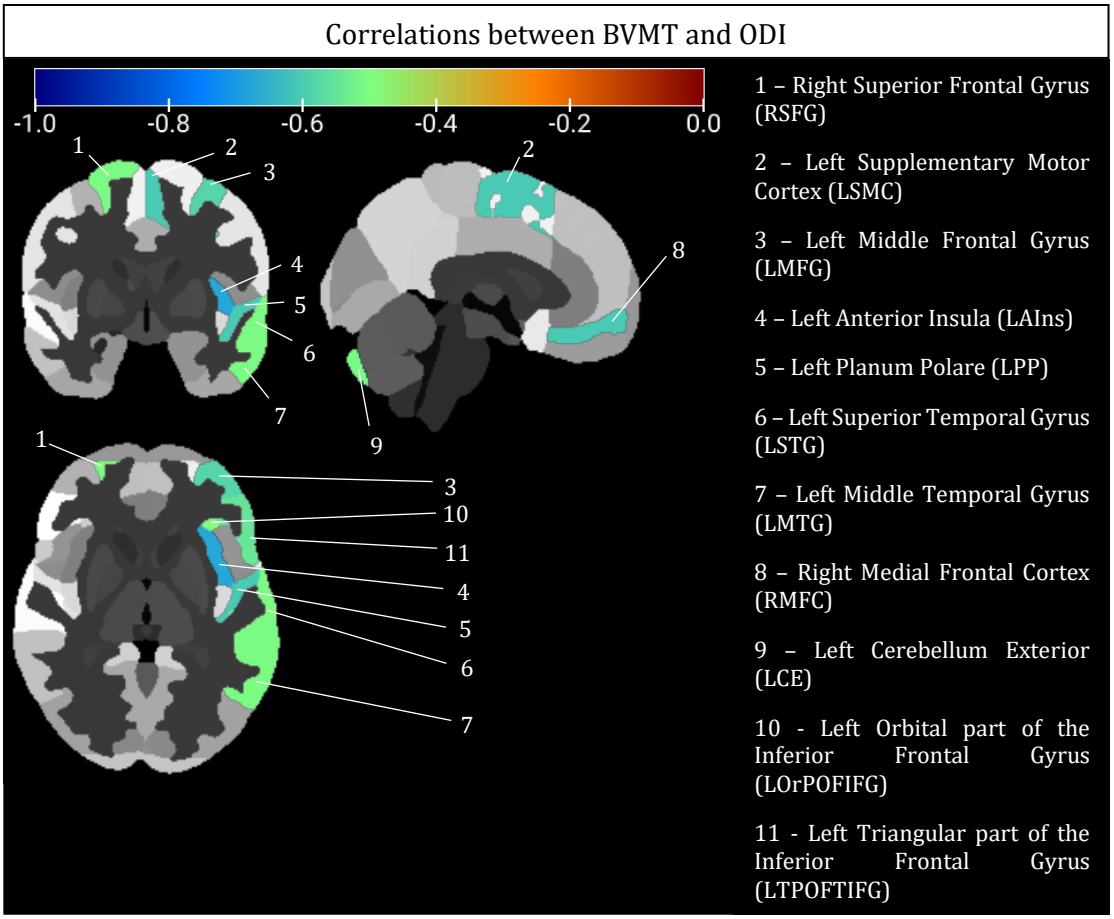

Fig. 34 ROIs with correlations between BVMT and ODI. The ROIs are overlaid on the Neuromorphometrics atlas, and the displayed slices have coordinates 0,0,0 mm in the MNI space. The colourbar represents the strength of the correlation; note that there are only negative correlations.

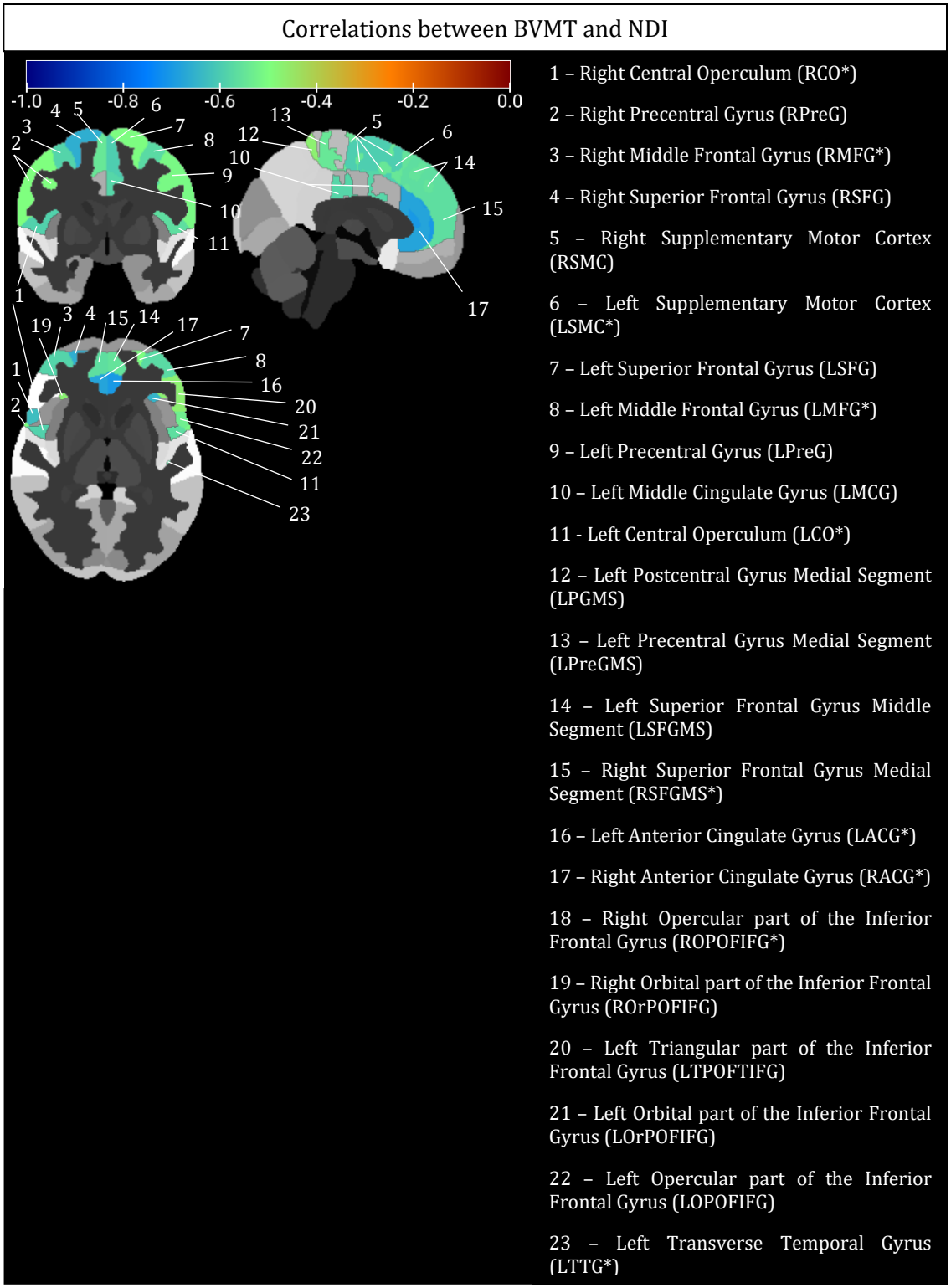

Fig. 35 ROIs with correlations between BVMT and NDI. The ROIs are overlaid on the Neuromorphometrics atlas, and the displayed slices have coordinates 0,0,0 mm in the MNI space. The colourbar represents the strength of the correlation; note that there are only negative correlations. Asterisks show statistically significant correlations with an FDR-corrected p-value lower than 0.05.

Of all the studied ROIs, 24 showed statistically significant correlations between FA and RME, with none remaining significant after FDR correction (see FA column in Table 19 of Annex D). In these ROIs, correlations were positive in all except one (LAA, r=-0.559); the highest correlation found was in the Left Precentral Gyrus (LPreG; r = 0.656). ADC and RME were widely correlated, showing negative associations in 29 ROIs (see ADC column in Table 19 of Annex D). Of these, 2 remained statistically significant (LAIns, Right Parahippocamapal Gyrus (RPhG)) after FDR correction; the highest correlation was for LAIns, with an r of -0.735. ODI and RME showed correlations in only 13 ROIs (12 negative, 1 positive), and none of them were statistically significant considering FDR-corrected p-values (see ODI column in Table 19 of Annex D). The positive correlation was in LAA (r = 0.710), and the strongest negative correlation was found in RACG (r=-0.644). Finally, NDI and RME were extensively correlated, with 27 ROIs identified as statistically significant maintaining their status after FDR correction (see NDI column in Table 19 of Annex D), and 2 ROIs that switched to nonsignificant. Yet, all these correlations were negative, with the highest being r=-0.697 (in RPG). These correlations are represented in Fig. 36 (RME and FA), Fig. 37 (RME and ADC), Fig. 38 (RME and ODI), and in Fig. 39 (RME and NDI).

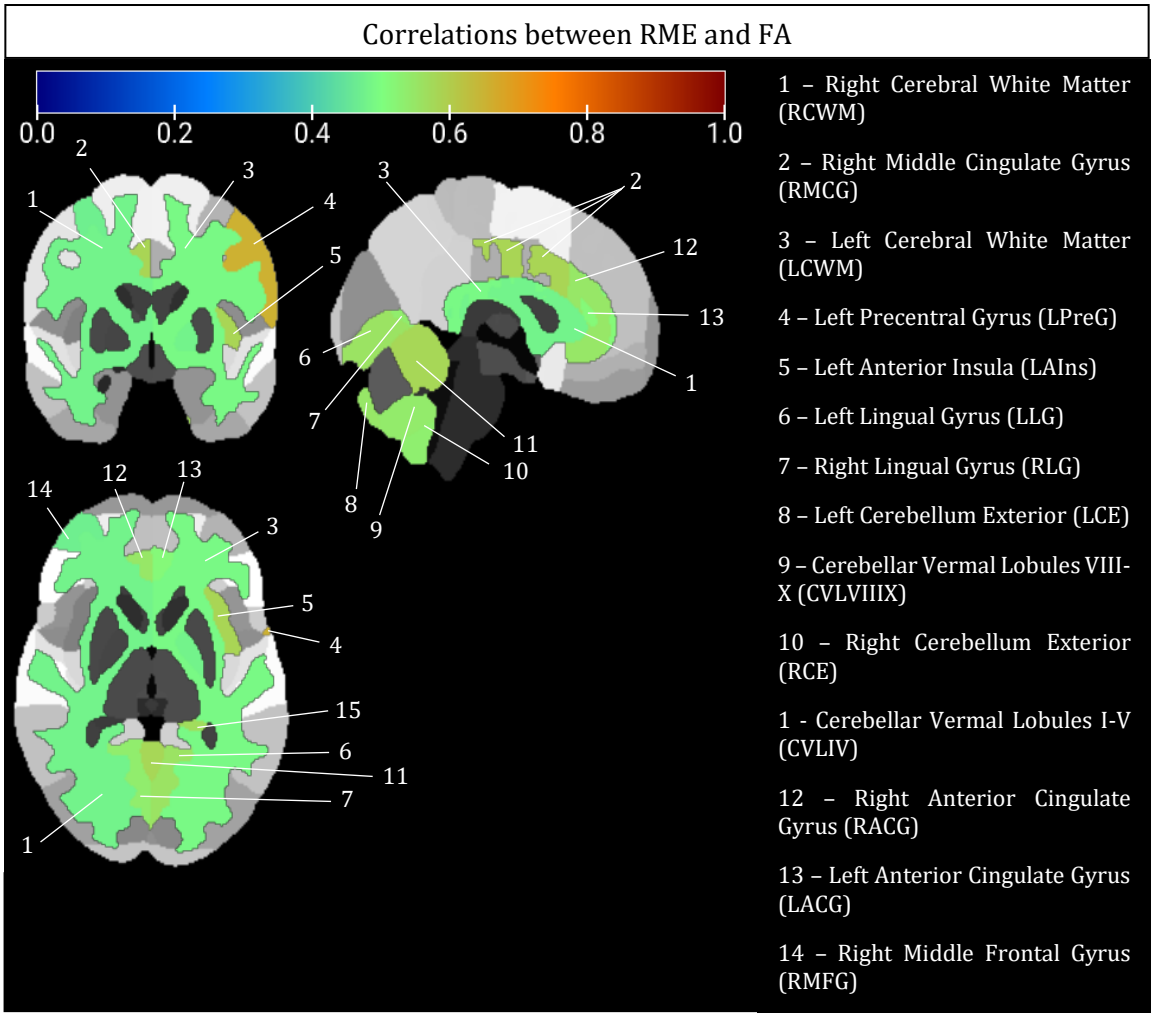

Fig. 36 ROIs with correlations between RME and FA. The ROIs are overlaid on the Neuromorphometrics atlas, and the displayed slices have coordinates 0,0,0 mm in the MNI space. The colourbar represents the strength of the correlation; note that there are only positive correlations.

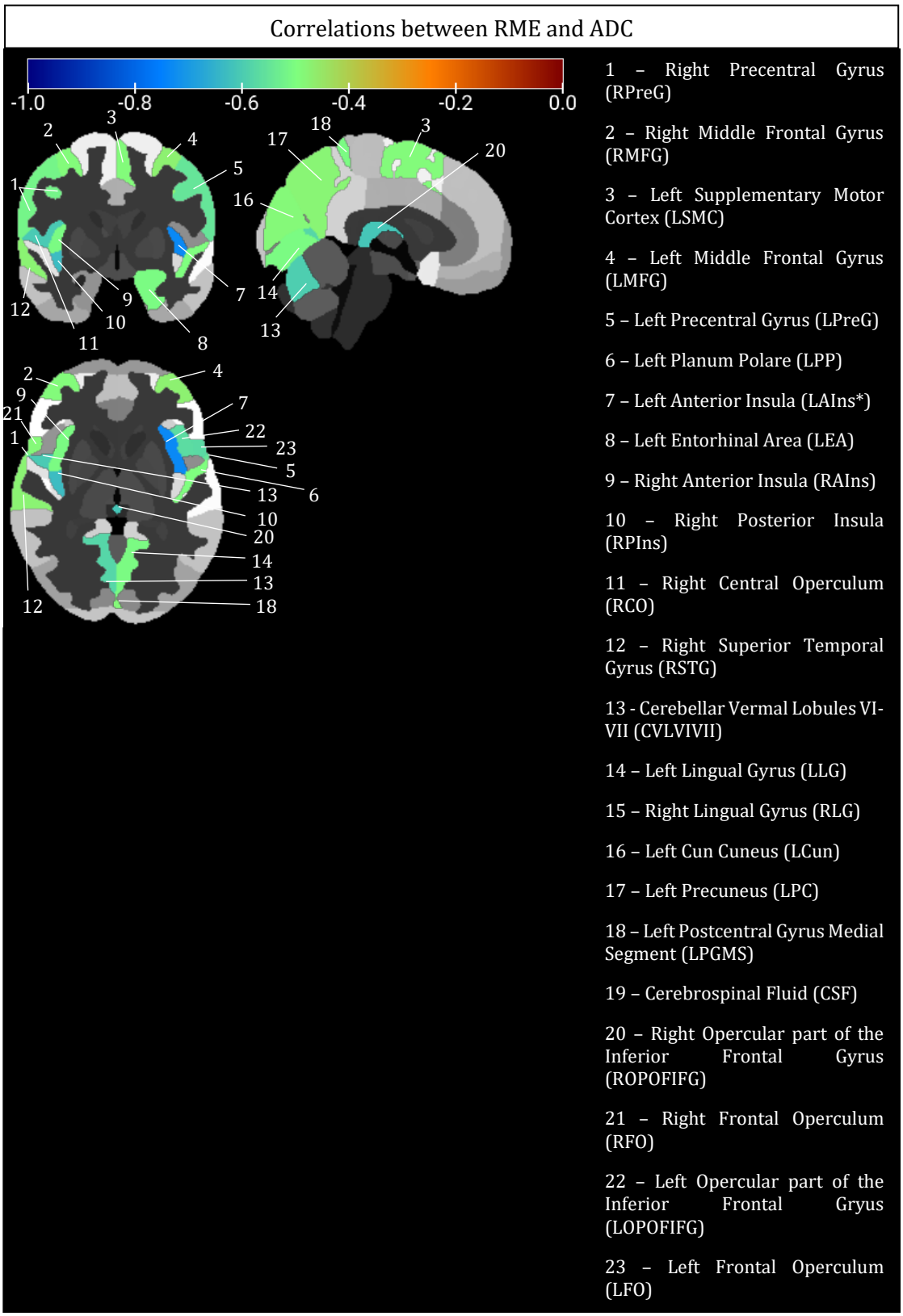

Fig. 37 ROIs with correlations between RME and ADC. The ROIs are overlaid on the Neuromorphometrics atlas, and the displayed slices have coordinates 0,0,0 mm in the MNI space. The colourbar represents the strength of the correlation; note that there are only negative correlations. Asterisks show statistically significant correlations with an FDR-corrected p-value lower than 0.05.

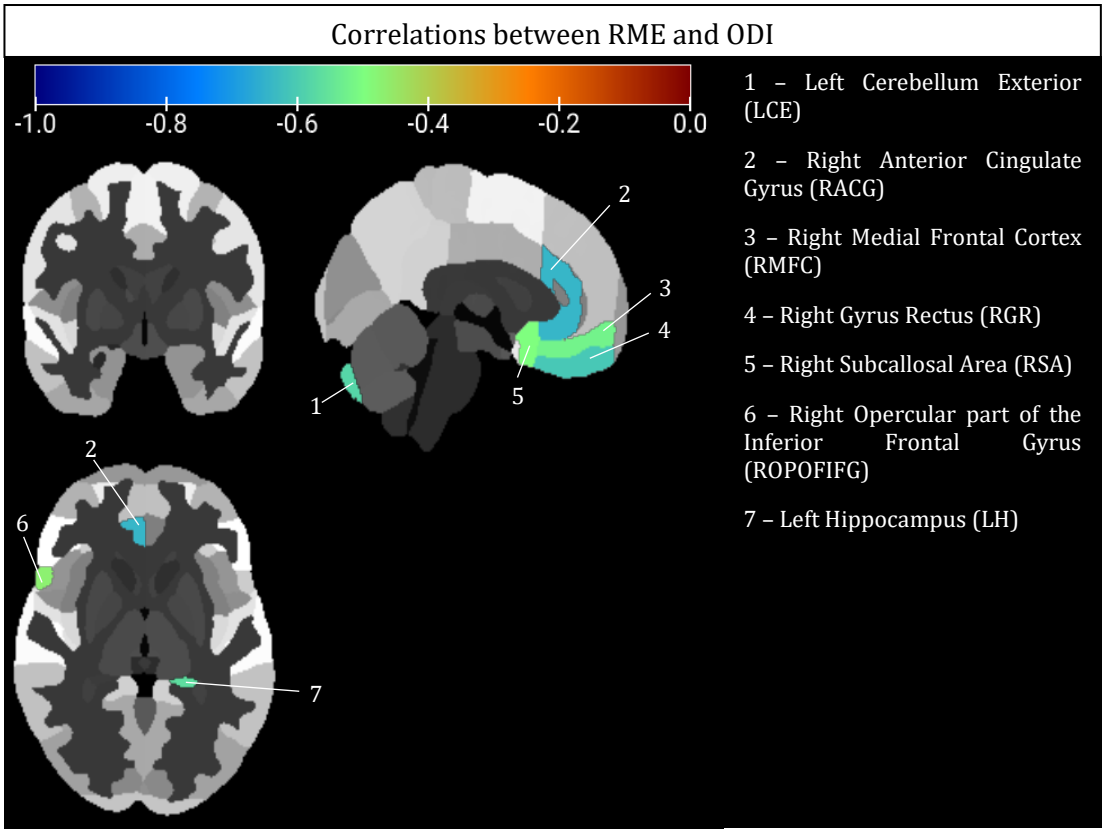

Fig. 38 ROIs with correlations between RME and ODI. The ROIs are overlayed on the Neuromorphometrics atlas, and the displayed slices have coordinates 0,0,0 mm in the MNI space. The colourbar represents the strength of the correlation; note that there are only negative correlations.

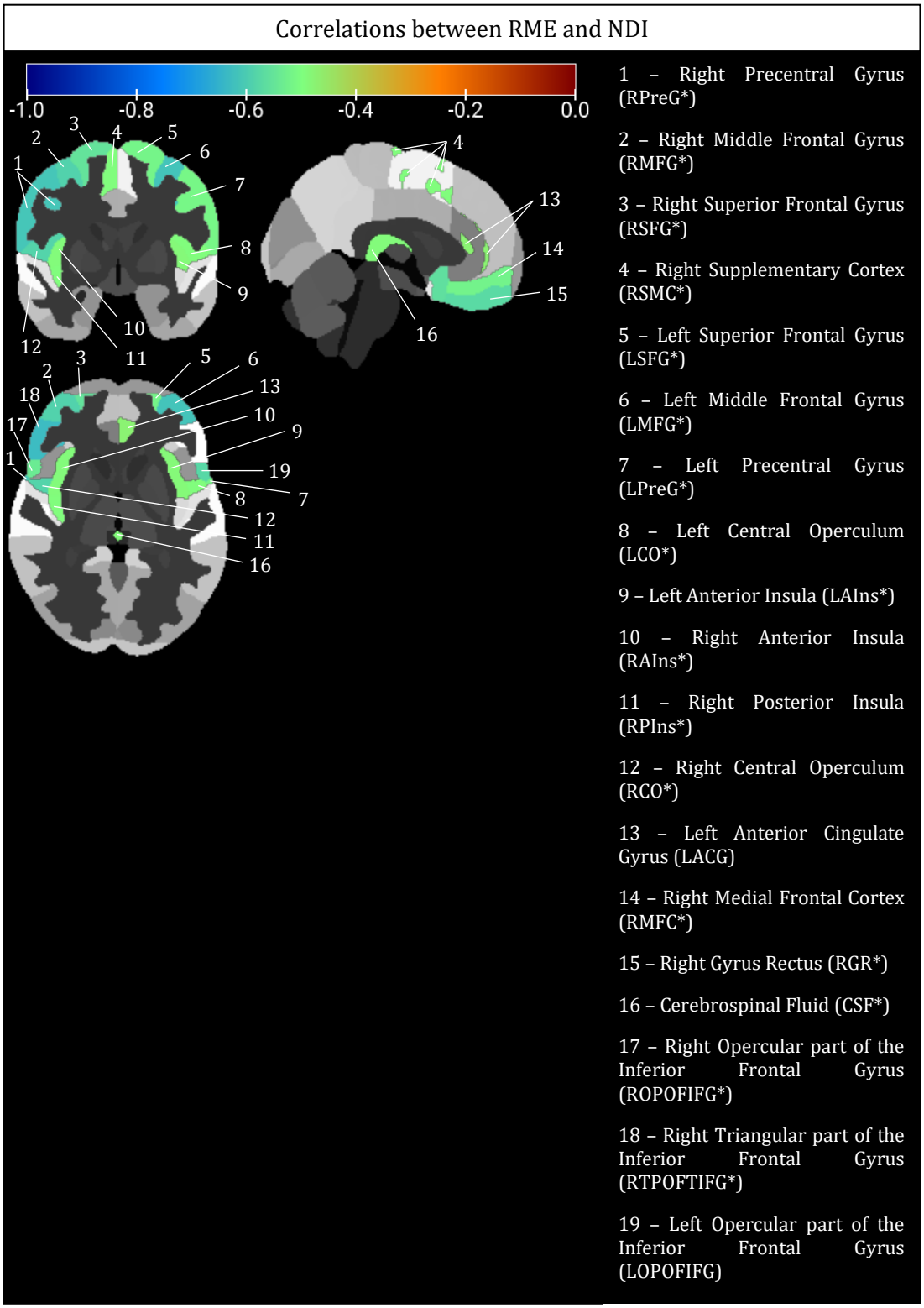

Fig. 39 ROIs with correlations between RME and NDI. The ROIs are overlaid on the Neuromorphometrics atlas, and the displayed slices have coordinates 0,0,0 mm in the MNI space. The colourbar represents the strength of the correlation; note that there are only negative correlations. Asterisks show statistically significant correlations with an FDR-corrected p-value lower than 0.05.

5. Discussion

5.1. Voxel-wise FA comparisons

The voxel-wise FA analysis showed a widespread decrease in FA in the MS patients' group, when compared to the healthy controls' group, as was expected. This solidifies the well-known notion that demyelination in MS patients leads to the loss of myelin integrity and possibly axonal damage, disrupting the barrier that keeps water moving with a preferred direction. The decrease in FA value thus represents the movement of water across the axon, leading to an increase in isotropy; this could be further verified by computing radial diffusivity and assess its voxel-wise differences.

Interestingly, the decrease in FA was not only present in lesions (where it is expected to exist more marked myelin insults) but also in NAWM. This suggests that NAWM is, in fact, "normal appearing", and not completely healthy. Even though there are no visible lesions in imaging, this tissue shows indications of myelin and axonal injury, as has been previously reported (Andersen et al., 2020; Cercignani et al., 1999; Costa Sousa, 2015). Comparing the global NAWM to the individual NAWM masking process, the latter seems to add sensitivity to the analysis. Differences are less widespread and more confined and may be interpreted as "truer" differences that the ones visible on Fig. 10 B (global NAWM masking), since this analysis excludes any voxel that does not exist in at least one participant, whereas the global NAWM mask includes voxels that may not belong to NAWM in some subjects. In lesions, there was a marked decrease in FA, which is visible in the high t-statistic of clusters in Fig. 10 D; this again shows demyelination in these regions. Even though these conclusions were reached, one still needs to keep in mind that other processes beside demyelination, like microstructural changes and orientation distribution, or even the existence of crossing fibres, contribute to a lower FA value.

5.2. Voxel-wise ADC comparisons

Inversely to FA, ADC shows an increase in MS patients, when compared to healthy controls. Again, this was to be expected (Aung et al., 2013; Cercignani et al., 1999). The loss of myelin integrity and axonal injury increase the directions in which water can diffuse, and so the amount of water diffusion (here represented by ADC) escalates; on the other hand, the increase in ADC represents a loss in structural organisation, which here is true, since the loss of myelin can lead to axonal damage, decreasing anisotropy, i.e., diffusion along the

axon fibre. Increased ADC values might also be due to an increase in free water, which can be caused by inflammation, and not demyelination. This is especially noticeable in NAWM and lesions (Fig. 11 B-D), where the t-statistic values are higher, which represents higher differences between the two groups. Furthermore, there seem to be more differences associated with ADC than with FA, which may mean that ADC can detect damage in locations not seen with FA analysis.

As was seen with FA, ADC can only indicate that there are changes in diffusion, but it cannot pinpoint exactly what changed. By knowing the organisation of WM tracts and what changes diffusion properties, one can conclude that these parameters are related to myelin and axonal injury, or inflammation, but they might lose meaning if, for example, the analysed voxel has crossing fibres. Therefore, it is important to consider other diffusion metrics, such as the ones presented next (NODDI model); mainly, using isotropic volume fraction maps from the NODDI model, it would be possible to infer the volume fraction that has isotropic diffusion, and see if an increase in ADC reflected a true increase in isotropy. Still, DTI can easily assess the severity of WM damage in MS, since higher differences in ADC and FA reflect more injury.

5.3. Voxel-wise ODI comparisons

ODI only showed statistically significant differences between the MSC group and the CNT group in one tissue of interest, NAWM. Even though there were not many differences, this still provides insight into WM disruption in MS: ODI is a marker of fibre dispersion and an increase in this value shows a loss in fibre coherence in NAWM, i.e., regions with highly compacted and parallel fibres lose this organisation and neurites become dispersed in more directions; a loss in neurite density (seen in the next topic – 5.4.) can also increase the orientation dispersion. The fact that there were not found any statistically significant differences in WM lesions may only mean that, for example, neurite density might decrease so much that any expected alteration in ODI will be overshadowed, since there are less neurites to be dispersed and an increase in ODI will not be observed. Considering this, it is plausible that ODI in MS patients will be similar to that in healthy controls.

5.4. Voxel-wise NDI comparisons

NDI is consistently lower in the MSC group, when compared to the CNT group, in all tissues of interest. This is an indication of the loss of neurite density in both NAWM and MS lesions. Comparing these results with DTI metrics, NDI seems to be more sensitive to

damage in MS, primarily in cerebral WM, since it identifies more voxels as being statistically different between groups than any other metric. In fact, NDI seems to not be very influenced by DTI metrics, which enlightens this parameter as a possible biomarker for early MS pathology. This is further supported by the fact that NDI shows a higher number of abnormal voxels than FA and ADC, which may reflect that there may be axonal pathology in early MS that is not justified by demyelinating processes, and thus the decrease in anisotropy is not only due to myelin injury; to try to verify this, it would be interesting to do an analysis that could quantify myelin content.

Lastly, the fact that NDI shows a higher number of voxels with differences for the CNT>MSC contrast than ODI shows for the MSC>CNT contrast, and still FA shows abnormal voxels for the MSC>CNT contrast stresses the relationship between these three parameters: both ODI and NDI contribute to FA, but ODI to a higher degree; NDI and FA are negatively related, whereas ODI and FA have a strong positive correlation. Knowing this, in the presence of a small number of abnormal voxels for ODI, it is necessary a greater change in NDI values for FA voxel-wise analysis to show results, which happens here.

5.5. Summary statistics of the means

When analysing statistically significant differences between the means of FA, ADC, ODI and NDI in the two studied groups, some interesting results were found. For both FA and ADC, this analysis corroborated what was found in the voxel-wise statistical analysis: an increase in ADC in NAWM and lesions when compared with WM in the CNT group, to a higher degree in lesions, which also showed a significant difference when compared to NAWM; a decrease in FA in NAWM and lesions compared with WM in the CNT group, but no difference between NAWM and lesions. The fact that there were no statistically significant differences between average FA in NAWM and lesions might indicate that other processes besides demyelination and/or axonal injury justify the evolution of NAWM tissue to lesion. If FA values are similar in these two tissues, NAWM shows the same degree of anisotropy loss, which is interpreted as myelin and axonal injury, as lesions, showing that other processes such as neurodegeneration play a part in lesions being visible on structural images.

On the other hand, ODI did not show statistically significant differences between lesions and WM in the voxel-wise analysis; however, average ODI in NAWM does not differ from the one in WM, whereas there is a marked difference between lesions and NAWM, and WM. Note that this analysis takes one average value of ODI per participant, while the voxel-

wise analysis identifies any voxel with a statistically significant difference and is then corrected for multiple comparisons. This may justify this apparent discrepancy in these results because the voxel-wise approach can hide voxels where statistically significant differences in lesions could occur. Still, this analysis shows a decrease in ODI in lesions, while an increase ODI in the NAWM is observed (even if not significant); this is in line with some results (Hagiwara et al., 2019; Zhang et al., 2012), but contradictory to others (Granberg et al., 2017). ODI analysis seems to present an intriguing outcome, since it can either be increased or decreased in both NAWM and lesions, without being expectable. The fact that ODI is lower in lesions may seem surprising, since it indicates that there is an increase in fibre coherence, and should be indicative of an increase in FA, because of the high negative correlation between ODI and FA (Zhang et al., 2012), which does not happen in MS lesions (FA values are lower). However, NDI also contributes to FA (to a lesser degree) and its wide variations may justify FA values (Zhang et al., 2012). It also needs to be taken into consideration that the interpretation of ODI values depend on its ground truth: if the healthy brain's ODI is high in that region (namely, highly parallel WM tracts), it may experience a decrease in disease (Spano et al., 2018). Lastly, a decrease in ODI can be accompanied by an increase in NDI, since a gain in neurite density in WM restores lower dispersion values seen in healthy cases. This is discussed in the next paragraph.

Finally, the NDI analysis shows the most surprising results of all: an increase in mean NDI in lesions. This is not seen on the voxel-wise analysis, but again note that this analysis was corrected for multiple comparisons, which is not the case here. One hypothesis for this result is the fact that there could be some degree of remyelination that leads to an increase in NDI, as suggested by (Sacco et al., 2020), showing that not all MS lesions have active tissue destruction; note that this work is focused on very early MS, with recently diagnosed patients, so it is probable that they can experience some degree of remyelination in lesions. This may very well help to justify the decrease in ODI values in lesions, since if there is active remyelination, there could also be a gain in fibre coherence at the same time. Here, there is no way to prove this; however, using a contrast agent such as Gadolinium could provide an insight as to whether there is an active inflammation in these lesions. Also, investigating changes in time, in a longitudinal study, could show if there was a shrinkage in the lesion or not, and thus trying to understand its evolution. Lastly, using other measures, such as T1/T2 ratio to evaluate myelin content, could supply more information that could be conjugated with these findings to reach a conclusion about the pathophysiological meaning of these results.

5.6. Correlations with cognitive and neuropsychological tests

Regarding the analysis of average diffusion metrics in tissues of interest, the only correlation found was between ODI in NAWM and MFIS. This was a positive correlation, which states that an increase in ODI in NAWM should lead to an increase in MFIS, i.e., an increase in the patient's fatigue degree. In both the voxel-wise analysis and the statistical analysis of the means, it was seen an increase in ODI in NAWM, when compared to WM and to lesions. Since this increase implicates a loss in fibre coherence and can be accompanied by a loss in neurite density, as well as a decrease in FA, it is acceptable to consider that it may also lead to a decay in a patient's physical sate.

The correlations with diffusion metrics in ROIs, on the other hand, showed a multitude of different results, which are discussed below.

5.6.1. Correlations between EDSS and diffusion metrics

Knowing that EDSS is a scale that measures disability, and higher scores represent worse disability, and that a decrease in FA is a sign of myelin/axonal damage that leads to the slowing or interruption of the conduction of the nerve impulse, the negative correlations seen seem to make sense: an increase of EDSS can be justified by a decrease in FA. However, positive correlations were not to be expected. They indicate that a worsening in a patient's incapacity can be explained by an increase in FA. In fact, one of the ROIs that survived the FDR correction shows a positive correlation, but that might be a spurious correlation. Nonetheless, if these measures are in cortical lesions, these results may start to make sense, since it has been reported an increase in FA in cortical lesions (Granberg et al., 2017). Furthermore, it is also conceivable that maladaptive compensatory mechanisms might be observed, namely corresponding to (apparently beneficial) increased FA correlating with higher EDSS scores.

However, in the Right Accumbens Area (RAA), where FA shows a positive correlation with EDSS, ODI shows a negative one. Knowing that the ODI value largely contributes to the FA value and that they are inversely correlated, there seems to be some consistency in these results. Hypothetically, an increase in FA would lead to an increase in EDSS, as would a decrease in ODI, in this region; this could be justified if histological analysis

was performed to assess the integrity of fibres in that region, and to see if maybe there could be a compensation mechanism in MS patients that led to an improvement in diffusion metrics. Still, note that this is a subcortical region, and thus has a different microstructure from WM and other GM regions, which should be taken into account.

Since an increase in ADC indicates an overall increased diffusion and may indicate axonal/myelin injury, a positive correlation with EDSS seems to be reasonable. Still, ADC is not specific for a loss in myelin, and it may represent other processes, such as ongoing inflammation (increase in inflammatory free water component) and so the interpretation of these correlations remains limited.

An increase in orientation dispersion indicates a loss in fibre coherence and increasing of bending processes, and thus it seems reasonable to think that it is positively related to EDSS: a loss in fibre coherence can lead to an increase in disability and EDSS score. However, interpretation of ODI results needs greater care. The variation of its value may depend on whether we are in the presence of MS lesions or NAWM, as it has been demonstrated in section 5.5. Thus, by only looking at the ROIs where correlations appeared it is not possible to infer their veracity. It would be necessary to evaluate the type of tissue (either normal appearing brain tissue or lesions) to better understand these correlations. These results are in line with the ones from (Spano et al., 2018), where EDSS was associated with both an increase and a decrease in ODI, since this parameter may depend on regional microstructure.

The fact that all correlations between EDSS and NDI were negative means that, in the identified regions, a decrease in NDI is associated to an increase in EDSS, i.e., a decrease in neurite density explains an increase in disability. This is understandable, considering that a decrease in neurite density may break some important connections that were maintaining the patient's physical status, leading to physical disability. The fact that correlations between both NDI and EDSS and ODI and EDSS were found may indicate that disability in early phases of MS, however clinically relevant it may be, can be explained by neurodegeneration.

5.6.2. Correlations between MFIS and diffusion metrics

MFIS is a scale that indicates more fatigue for higher scores, and thus it is coherent that a decrease in FA (myelin/axonal damage) is associated with an increase in MFIS. It would be interesting to know the exact mechanisms behind fatigue in MS, so that some light could be shed into the importance of these ROIs in showing negative correlations with FA.

As it was with FA, the positive correlations between MFIS and ADC are coherent with the notion that an increase in ADC is related to the worsening of MS symptoms, such as fatigue.

All correlations between MFIS and ODI were positive, meaning that an increase in ODI and consequently loss of highly compact fibres, contributes to an increase in MFIS and, ultimately, fatigue. It is interesting to note that in some regions (Left Planum Temporale (LPT), Left Posterior Insula (LPIns), RMTG and RPIns) these positive correlations are accompanied by negative correlations between FA and MFIS, thus reinforcing the relationship between these two metrics, in these regions.

The correlations between MFIS and NDI were all positive. That indicates that an increase in NDI leads to an increase in fatigue, i.e., worsening of MS symptoms. Since it was observed a decrease in NDI in the voxel-wise analysis and an increase in average NDI in MS lesions for MS patients, by solely looking at these results, no conclusions can be drawn as to whether these are spurious correlations, or e.g., the increase in NDI results in more neuronal activation or connectivity, leading to higher energy consumption, which in turn would lead to increased levels of fatigue.

5.6.3. Correlations between SDMT and diffusion metrics

SDMT measures information processing and motor speed, which are known to be impaired in MS (Ryan et al., 2020). Because higher scores mean higher processing speed, most of the correlations were expected. A decrease in FA should reflect in a decrease in SDMT, since the apparent loss of myelin should compromise impulse conduction and consequent neurological abilities. The only negative correlation may be related to noise, but again its location should be further analysed, as should the myelin content.

The negative associations found between SDMT and ADC match the concept that an increase in ADC is associated with cognitive impairment, here represented by a decrease in processing speed. The positive correlations, however, cannot have such an easy interpretation since they may not represent a true correlation and rather a spurious one; however, these positive correlations could still be an indicator of maladaptive diffusion compensatory mechanisms, or of functional compensatory mechanisms that allow higher scores for higher ADC, simply because structural damage can be overcome.

The results from correlations between SDMT and ODI express the connection between the increase in neurite orientation and the increase in cognitive impairment, here represented by a decrease in SDMT. This increase in neurite orientation is representative of a disorganisation in axonal tracts and loss of highly parallel orientations, which can eventually lead to a decline in processing and motor speed. Also, note that ODI is remarkably higher for GM areas, so the location of ROIs should be taken into account, to see if these correlations are related to WM injury or to GM.

Concerning the relationship between SDMT and NDI, it shows that a decrease in NDI justifies an increase in SDMT. Note that, and this is valid for all tests answered by patients, MS patients can have a good performance in neuropsychological and cognitive tests; they can have compensation mechanisms in terms of functional connectivity that allow them to avoid consequences from structural damage, especially if early diagnosed. This may be a reason as to why a decrease in NDI (seen in patients) can justify an increase in tests' scores. However, there is a need for more context in these situations, and they might raise more questions than give answers.

5.6.4. Correlations between CVLT and diffusion metrics

CVLT is a test that assesses episodic memory, which is known to be deficient in MS (Stegen et al., 2010). Hence, MS patients perform poorly in this test if this cognitive component is impaired, achieving lower scores than healthy controls. So, it means something that FA is positively correlated with this test: a decrease in FA (considered as a sign of myelin and/or axonal damage), which is seen in MS patients as proved in voxel-wise analysis justifies a decrease in CVLT scores, and thus a decrease in memory preservation in MS; still, lower FA values can be due to an increase of bending axons or crossing fibers, which should reflect an increase in ODI and negative correlations between ODI and CVLT.

An increase in ADC is indicative of not only axonal/myelin injury, but also of inflammatory processes, as seen before, and it is natural that it is associated with a decrease in CVLT scores, in MS patients. The ROI that presents a positive correlation is the odd one out, and once again it needs to be carefully interpreted, since it might be a false positive. There is a need for more information to be able to draw meaningful conclusions about this relationship, since, at first sight, it is not what one would expect to see here.

The results from correlations between CVLT and ODI are in line with the SDMT results, where MS patients are expected to achieve lower scores for ODI increases. ODI can increase either due to a true increase in dispersion or can be related to a variation in NDI, where a decrease in neurite density or in axonal size can contribute to a higher ODI value, simply because the number of neurites is lower. So, this parameter alone may not indicate which subtle microstructural alteration is present and related to CVLT, and that is why it is important to take NDI into consideration.

The fact that all corelations between CVLT and NDI were negative emphasises what was discussed in the previous paragraph. NDI is a valuable metric when looking at the underlying processes that drive alterations in ODI. The fact that a loss in neurites correlates with an increase in CVLT may not seem relevant, since what was expected was the opposite. In fact, correlations were found in ROIs such as CSF and lateral ventricles (LLV and RLV), where NDI is not expected to contribute much, since these are the cerebrospinal fluid, and spaces that hold fluid, respectively. Logically, the number of neurites found there is not significant, and thus these correlations may not hold significant in this context; still, neurites are not non-existent – there are dendritic terminals that contact with the CSF (Vigh-Teichmann & Vigh, 1983). Taking this into account, the correlation between ODI and CVLT might be linked to the correlation between NDI and CVLT: a decrease in CVLT scores is associated with an increase in both NDI and ODI; this could be verified by calculating partial correlations or through mediation analysis. Since an increase and not a decrease in NDI is correlated with decreasing CVLT scores, ODI alterations that drive CVLT results can be seen as a true increase in dispersion, and not due to a loss of neurites. Again, the association between decreased NDI and increased tests' scores is not to be discarded without further investigation; the loss in neurites can very well be compensated by functional mechanisms, mainly in early MS, that can justify higher scores.

5.6.5. Correlations between BVMT and diffusion metrics

It has been reported that BVMT is highly correlated with SDMT (in a positive way, with rho=0.6) (de Caneda et al., 2018). Conjugating the fact that BVMT measures cognitive performance in the form of visuospatial learning and memory, its decrease should be related to a decrease in processing speed (decrease in SDMT), and the form of correlations (positive or negative) between BVMT and diffusion metrics should be similar to what was found for SDMT.

Knowing what was explained in the previous paragraph and all that was discussed until now, it is acceptable that a decrease in FA values can be associated with a decrease in BVMT and ultimately, an increase in cognitive impairment.

As was discussed earlier regarding the relationship between BVMT and SDMT, what was expected to be found were negative correlations between BVMT and ADC. This was indeed true for most of the significative ROIs but untrue for 1 ROI. This region is RAA, which has shown controversial results before (EDSS and FA, EDSS and ODI), and it seems coherent that it remains that way. Since this region consistently behaves the same way in more than one analysis, it may no longer be a simple false positive. It could be producing consistent signals or noise, but there might be something in the structure of the accumbens area that leads to these correlations. Making that ROI an exception, these results are concordant with an increase in ADC being related to a decrease in cognitive performance in MS patients. Nonetheless, these apparently odd results must be put in the context of being observed in very early MS patients and of being coherent across metrics/tests, which shows the potential for this type of studies to identify very early alterations that should be investigated further.

The negative correlations found between BVMT and ODI are in line with the FA findings, since FA and ODI seem to be inversely correlated. Here, an increase in ODI is associated to lower BVMT scores, which are associated to MS patients.

The correlations found between BVMT and NDI were all negative, showing that an increase in NDI should lead to a decrease in BVMT. This seems to contradict what was found for other measures, i.e., alterations found in MS patients (decrease in FA, increase in ADC, increase in ODI) should be related to lower BVMT scores. It has been shown that MS patients present a lower NDI value, and thus, for these results to be coherent, the correlations should be positive. Again, the influence of compensatory phenomena in cognitive performance as a way of fighting pathological processes are not to be disregarded.

5.6.6. Correlations between RME and diffusion metrics

It has been shown that social cognition, here evaluated by RME, is impaired in MS (Batista, Alves, et al., 2017; Batista, d'Almeida, et al., 2017). This demonstrates that symptoms are not only physical and supports the concept that psychological and mental abilities may be affected in MS. Hence, RME quantifies how well a person can predict someone else's mental emotional state, and higher scores represent a higher ability to do that (Chalah et al., 2017). Then, it is expected that MS patients reach lower RME scores and

that diffusion metrics correlate with them accordingly. That seems to be true for FA, where a decrease in its values leads to a decrease in RME and thus an increase in impairment of social cognition, a recognised consequence of damage by MS. The outlier observed matches the one from correlations between EDSS and FA, but in this case being the left hemisphere the one implied (Left Accumbens Area, LAA). This seems to follow a tendency, where unexpected correlations for FA appear in these regions (RAA and LAA); it would be interesting to try and assess what might be going on with myelin and what axonal/neurite changes may be occurring with other imaging or contrast techniques, to better determine if we are in fact in the presence of a spurious correlation.

The consistency of negative correlations between RME and ADC is what was anticipated, knowing how ADC is a marker for pathology. Therefore, an increase in ADC may validate a decrease in RME scores, in these regions.

Interestingly, for correlations between RME and ODI, 12 of the statistically significant ROIs showed negative correlations but one showed a positive correlation. This one was LAA. Again, this is aligned with the FA results and with the relationship between FA and ODI; this emphasises the need to carefully handle these results, since this consistency may be an indicative that these correlations might have some significance. For the rest of them, the negative correlation seems adequate: an increase in neurite dispersion leads to a decrease in RME scores, which is patent in MS patients as observed.

Again, the results for NDI were not what one could predict: a decrease in NDI should not justify an increase in RME scores and thus a better social cognition. As was previously discussed for contradictory NDI results, it is important to try to understand what kind of tissue is present in each of these ROIs (either normal appearing or lesions) and if that can lead to some insight into these results. As discussed earlier, we cannot exclude that the better performance of any cognitive test has the effect of compensatory mechanisms, which might surpass the damage provoked by the disease and underly the contradiction with diffusion metrics observed. Moreover, CSF was once again considered as a statistically significant ROI for this correlation, which creates more questions about the meaning of these results.

5.6.7. Final considerations

In total, 136 ROIs from the Neuromorphometrics atlas were considered for this ROI-wise correlation analysis. From both the figures on the Results section and the tables on the Annexes section, it is obvious that NODDI metrics showed (overall) more correlations than

DTI metrics. This is a reinforcement that NODDI is more sensitive to damage caused by MS than DTI, particularly in early disease stages. However, these results call for a more thorough analysis. Some correlations (mainly with NDI) were not what were expected. These contradictory results can have many causes; for example, the fact that Pearson's correlation was used in normally distributed tests (MFIS, SDMT, CVLT, BVMT, and RME) and that it treats the variables as linearly dependent, has a high sensitivity for outliers, and has a known lack of robustness, may have led to some spurious correlations (Pernet et al., 2013). This is further aggravated by the fact that, in each ROI, not all diffusion metrics' values were normally distributed in all tests performed. For each ROI, ten normality tests were applied, and the metric was considered as having a normal distribution if the result of at least one test came out as normal; using this rule, every diffusion metric showed a normal distribution in all ROIs. This could have led to an oversimplification of the method, since in some cases Spearman's correlation might have been a better fit. However, note that the images were previously filtered in the pre-processing steps, precisely to achieve Gaussianity. Hence, any deviation from the normal distribution should not have a major influence in the results. On the other hand, effect size should be calculated in future interpretations of these results since it could be a possible indicator of spuriousness.

Even though NDI seems to show correlations with the performed cognitive and neuropsychological tests that do not resemble what was predicted by conjugating the knowledge of what NDI is and how it behaves in MS, the associations presented were considerable. Further studies are needed to understand why these correlations seem to be opposite from what was expected and if it means something in this context or if they could be treated as false positives; it needs to be revised whether an increase in NDI could be linked to MS patients (maybe as a compensatory mechanism) and justify the increase associated with MS patients in certain cognitive/neuropsychological tests. Note that this increase was seen on the average NDI in MS lesions, so it is not unthinkable to hypothesise that some of these ROIs could present a tissue that behaves in the same manner, especially in the case of abnormal tissue preceding the evidence of lesions, where remyelination could be an attempt to fight an early stage of myelin loss that would lead to axonal damage, namely neurite loss.

Another interesting consideration is that there were correlations in regions that were not statistically significantly different between groups in voxel-wise analysis. This might mean that there are changes in diffusion metrics that are so subtle that are not

considered as significantly altered, but that still influence impairment in MS, in certain regions.

In conclusion, physical and cognitive impairment in MS seems to be described as an increase in ADC and ODI values, a decrease in FA values, and a decrease or increase in NDI values. This means that the processes leading to disability in early MS are demyelination, inflammation, increase in sprawling dendritic processes, neurodegeneration, and axonal/dendritic loss (or neurite gain, in cases where there is an increase in NDI).

6. Limitations

This work is not free of some limitations, which should be considered when interpreting the results. Below is the description of what I consider to be the major contributions for eventual bias in the previously presented results.

The transformation of the NODDI maps into the MNI space was performed via a TBSS script, using an FA template. Although the data used to extract both metrics are the same, the obtained maps were a little blurred when compared to the original images, and this may have meant some information loss, even though the voxels' intensities were similarly distributed.

The lesion map mask was not thresholded; this means that every voxel that was considered as a lesion by the LST toolbox was included in the mask. This may lead to an overestimation in lesions, since it was possible that one voxel was a lesion in only one participant, but it was included as one in all participants, leading to the inclusion of voxels in the voxel-wise statistical analysis that were not representative of the whole group of MS patients. Another drawback in this mask is the fact that the estimation of lesions made by the LST toolbox was not checked by a trained radiologist. This toolbox considered hyperintensities in the T2-weighted image as lesions, and there could have been physiological hyperintensities that were considered as brain injury, which again leads to an overestimation in lesion load. Nonetheless, the LST was specifically developed and validated as a reliable tool for segmentation of MS lesions.

The choice in thresholding for the NAWM and WM masks was arbitrary. It was based on visual inspection of several threshold values, and it is possible that these masks did not cover all WM tissue; it was a compromise between including the most WM tissue possible, while excluding GM and CSF.

The choice of the amount of smoothing of the scans before entering voxel-wise statistics was based solely on trying to preserve the most information possible and at the same time achieving some smoothing degree. Again, it was based on visual inspection, and even though the amount of smoothing was not excessively high, it could still have led to the loss of information. Nonetheless, the smoothing level is similar to many voxel-wise neuroimaging studies in the literature.

The fact that the masks from the Neuromorphometrics Atlas had to be registered into the MNI space and then binarized may have led to an overestimation of the brain

regions. There could have been an overlap to some degree between some regions, and the correlations identified in such regions may extend a little over their borders. However, if occurring, this effect is expected to be very small, and not represent a significant bias in these analyses.

7. Conclusion

DWI has proven to be a valuable tool in assessing microstructural changes in MS. The various ways to analyse these data make this technique a rich source of information that can be used to monitor disease progression and medication effects, understand its mechanisms, and try to predict its outcomes. DTI and NODDI are complementary approaches to DWI data. DTI is widely used in clinical environments and in research facilities; NODDI adds sensitivity to pathology and MS underlying mechanisms and thus opens a window to new discoveries.

The main goal of this work was to understand how DTI and NODDI metrics differed between early MS patients and healthy controls, either voxel-wise or in tissues of interest, and how that variation reflected pathology at a microstructural level. Then, these DTI and NODDI-derived parameters were correlated with cognitive and neuropsychological tests of interest. Studies with early MS patients such as this study's sample are scarce, and not all of them apply statistical analysis in a voxel-wise manner or try to correlate diffusion metrics with the same tests presented here.

Most of the results presented in this thesis are in concordance with previous studies. However, some novel results provide new insights into what was taken as a ground truth for the behaviour of diffusion metrics in MS patients; the best example of it is the higher average NDI found in MS lesions, which is uncommon and almost unheard of. The correlations found are also of importance and may be a window into what might be happening not only in white matter, but also in grey matter in the brain of MS patients. Additionally, the fact that areas such as normal appearing brain tissue also showed differences in this analysis and not on MRI structural imaging indicates that CNS damage happens all over the brain and is not confined to lesions.

Overall, NODDI-derived parameters seemed to better describe the major contributors to early MS pathology; NDI reflects neurite density loss in MS and this work gives a step into considering it a structural biomarker for both cognitive impairment in MS and CNS dysfunction. This further validates NODDI as a novel tool to analyse DWI data and to drive more conclusions about the hidden mechanisms of MS.

Future work in this context should include a longitudinal analysis, to better understand the meaning of the previously mentioned alterations in MS patients; mainly, it would be a way to investigate the hypothesis that higher NDI in MS lesions is a way to try to

compensate for demyelination and CNS insults in early MS. Using other methods for DWI analysis, such as the diffusion kurtosis or T1/T2 ratio as a marker for myelin density could also prove useful in explaining the results found.

With this work, diffusion metrics proved to be valuable in the monitoring of MS. Science evolves a little every day, and one can hope that tools such as NODDI can be implemented in clinical routine in the future, thus giving more information to both clinicians and patients about exactly what is happening, and to the pharmaceutical industry, which can hopefully someday find a cure for MS, or at least greatly improve patient's quality of life.

References

Andersen, K. W., Lasič, S., Lundell, H., Nilsson, M., Topgaard, D., Sellebjerg, F., Szczepankiewicz, F., Siebner, H. R., Blinkenberg, M., & Dyrby, T. B. (2020). Disentangling white-matter damage from physiological fibre orientation dispersion in multiple sclerosis. *Brain Communications*, *2*(2). https://doi.org/10.1093/braincomms/fcaa077

Archibald, R., & Gelb, A. (2002). A Method to Reduce the Gibbs Ringing Artifact in MRI Scans While Keeping Tissue Boundary Integrity. *IEEE Transactions on Medical Imaging*, *21*(4), 305–319.

Aung, W. Y., Mar, S., & Benzinger, T. L. (2013). Diffusion tensor MRI as a biomarker in axonal and myelin damage. In *Imaging in Medicine* (Vol. 5, Issue 5, pp. 427–440). https://doi.org/10.2217/iim.13.49

Baron-Cohen, S., Wheelwright, S., Hill, J., Raste, Y., & Plumb, I. (2001). The ' ' Reading the Mind in the Eyes ' ' Test Revised Version : A Study with Normal Adults, and Adults with Asperger Syndrome or High-functioning Autism. *J. Child Psychol. Psychiat*, *42*(2), 241–251.

Basser, P. J., & Jones, D. K. (2002). Diffusion-tensor MRI: theory, experimental design and data analysis - a technical review. *NMR in Biomedicine*, *15*, 456–467. www.interscience.wiley.com

Batista, S., Alves, C., D'Almeida, O. C., Afonso, A., Félix-Morais, R., Pereira, J., MacÁrio, C., Sousa, L., Castelo-Branco, M., Santana, I., & Cunha, L. (2017a). Disconnection as a mechanism for social cognition impairment in multiple sclerosis. *Neurology*, *89*(1), 38–45. https://doi.org/10.1212/WNL.0000000000004060

Batista, S., Alves, C., D'Almeida, O. C., Afonso, A., Félix-Morais, R., Pereira, J., MacÁrio, C., Sousa, L., Castelo-Branco, M., Santana, I., & Cunha, L. (2017b). Disconnection as a mechanism for social cognition impairment in multiple sclerosis. *Neurology*, *89*(1), 38–45. https://doi.org/10.1212/WNL.0000000000004060

Batista, S., d'Almeida, O. C., Afonso, A., Freitas, S., Macário, C., Sousa, L., Castelo-Branco, M., Santana, I., & Cunha, L. (2017). Impairment of social cognition in multiple sclerosis:

Amygdala atrophy is the main predictor. *Multiple Sclerosis*, *23*(10), 1358–1366. https://doi.org/10.1177/1352458516680750

Benedict, R. H., Tomic, D., Cree, B. A., Fox, R., Giovannoni, G., Bar-Or, A., Gold, R., Vermersch, P., Pohlmann, H., Wright, I., Karlsson, G., Dahlke, F., Wolf, C., Kappos, L., & Online, M. (2020). Siponimod and Cognition in Secondary Progressive Multiple Sclerosis EXPAND Secondary Analyses Siponimod for Cognition in Secondary Progressive Multiple Sclerosis: Thinking Through the Evidence Page 91 Criteria for rating therapeutic and diagnostic studies. *Neurology*, *96*, 376–386. https://doi.org/10.1212/WNL.0000000000011275

Bernabéu-Sanz, Á., Morales, S., Naranjo, V., & Sempere, Á. P. (2021). Contribution of Gray Matter Atrophy and White Matter Damage to Cognitive Impairment in Mildly Disabled Relapsing-Remitting Multiple Sclerosis Patients. *Diagnostics*, *11*(578), 1–17. https://doi.org/10.3390/diagnostics11030578

Bester, M., Lazar, M., Petracca, M., Babb, J. S., Herbert, J., Grossman, R. I., & Inglese, M. (2013). Tract-specific white matter correlates of fatigue and cognitive impairment in Benign Multiple Sclerosis. *Journal of the Neurological Sciences*, *330*(0), 61–66. https://doi.org/10.1016/j.jns.2013.04.005

By, S., Xu, J., Box, B. A., Bagnato, F. R., & Smith, S. A. (2017). Application and evaluation of NODDI in the cervical spinal cord of multiple sclerosis patients. *NeuroImage: Clinical*, *15*, 333–342. https://doi.org/10.1016/j.nicl.2017.05.010

Ceccarelli, A., Bakshi, R., & Neema, M. (2012). MRI in multiple sclerosis: A review of the current literature. In *Current Opinion in Neurology* (Vol. 25, Issue 4, pp. 402–409). https://doi.org/10.1097/WCO.0b013e328354f63f

Cercignani, M., Iannucci, • G, & Filippi, • M. (1999). Diffusion-weighted imaging in multiple sclerosis. *Italian Journal of Neurological Sciences*, *20*, 246–249.

Chalah, M. A., Kauv, P., Lefaucheur, J. P., Hodel, J., Créange, A., & Ayache, S. S. (2017). Theory of mind in multiple sclerosis: A neuropsychological and MRI study. *Neuroscience Letters*, *658*, 108–113. https://doi.org/10.1016/j.neulet.2017.08.055

Chan, R. W., Lau, J. Y. C., Lam, W. W., & Lau, A. Z. (2019). Magnetic resonance imaging. In *Encyclopedia of Biomedical Engineering* (Vols. 1–3, pp. 574–587). Elsevier. https://doi.org/10.1016/B978-0-12-801238-3.99945-8

Chen, A., Wen, S., Lakhani, D. A., Gao, S., Yoon, K., Smith, S. A., Dortch, R., Xu, J., & Bagnato, F. (2021). Assessing brain injury topographically using MR neurite orientation dispersion and density imaging in multiple sclerosis. *Journal of Neuroimaging*, *31*(5), 1003–1013. https://doi.org/10.1111/jon.12876

Chu, S.-H., Parhi, K. K., & Lenglet, C. (2018). Function-specific and Enhanced Brain Structural Connectivity Mapping via Joint Modeling of Diffusion and Functional MRI. *Scientific Reports*, *8*(1), 1–19. https://doi.org/10.1038/s41598-018-23051-9

Cleary, J. O. S. H., & Guimarães, A. R. (2014). Magnetic Resonance Imaging. In *Pathobiology of Human Disease: A Dynamic Encyclopedia of Disease Mechanisms* (pp. 3987–4004). Elsevier Inc. https://doi.org/10.1016/B978-0-12-386456-7.07609-7

Collorone, S., Cawley, N., Grussu, F., Prados, F., Tona, F., Calvi, A., Kanber, B., Schneider, T., Kipp, L., Zhang, H., Alexander, D. C., Thompson, A. J., Toosy, A., Wheeler-Kingshott, C. A. G., & Ciccarelli, O. (2020). Reduced neurite density in the brain and cervical spinal cord in relapsing–remitting multiple sclerosis: A NODDI study. *Multiple Sclerosis Journal*, *26*(13), 1647–1657. https://doi.org/10.1177/1352458519885107

Costa Sousa, F. (2015). *Application of diffusion tensor imaging in multiple sclerosis* [Dissertação de Mestrado]. Universidade de Coimbra.

de Caneda, M. A. G., Cuervo, D. L. M., Marinho, N. E., & de Vecino, M. C. A. (2018). Visuospatial memory test in multiple sclerosis The Reliability of the Brief Visuospatial Memory Test-Revised in Brazilian multiple sclerosis patients. *Dement Neuropsychol*, *12*(2), 205–211. https://doi.org/10.1590/1980-57642018dn12-020014

de Figueiredo, E. H. M. S. G., Borgonovi, A. F. N. G., & Doring, T. M. (2011). Basic concepts of mr imaging, diffusion mr imaging, and diffusion tensor imaging. In *Magnetic Resonance Imaging Clinics of North America* (Vol. 19, Issue 1, pp. 1–22). W.B. Saunders. https://doi.org/10.1016/j.mric.2010.10.005

de Santis, S., Bastiani, M., Droby, A., Kolber, P., Zipp, F., Pracht, E., Stoecker, T., Groppa, S., & Roebroeck, A. (2019). Characterizing Microstructural Tissue Properties in Multiple Sclerosis with Diffusion MRI at 7 T and 3 T: The Impact of the Experimental Design. *Neuroscience*, *403*, 17–26. https://doi.org/10.1016/j.neuroscience.2018.03.048

Descoteaux, M. (2015). High Angular Resolution Diffusion Imaging (HARDI). In *Wiley Encyclopedia of Electrical and Electronics Engineering* (pp. 1–25). John Wiley & Sons, Inc. https://doi.org/10.1002/047134608x.w8258

Dobson, R., & Giovannoni, G. (2019). Multiple sclerosis – a review. In *European Journal of Neurology* (Vol. 26, Issue 1, pp. 27–40). Blackwell Publishing Ltd. https://doi.org/10.1111/ene.13819

ElSayed, M. E. S. K. A., El-Toukhy, M. M. B., Asaad, R. E., & El-Serafy, O. A. (2019). Diffusion tensor imaging for assessment of normally appearing white matter of the brain and spinal cord in cases of multiple sclerosis: a multi-parametric correlation in view of patient's clinical status. *Egyptian Journal of Radiology and Nuclear Medicine*, *50*(30), 1–10. https://doi.org/10.1186/S43055-019-0031-X

Enzinger, C., Barkhof, F., Ciccarelli, O., Filippi, M., Kappos, L., Rocca, M. A., Ropele, S., Rovira, À., Schneider, T., de Stefano, N., Vrenken, H., Wheeler-Kingshott, C., Wuerfel, J., & Fazekas, F. (2015). Nonconventional MRI and microstructural cerebral changes in multiple sclerosis. In *Nature Reviews Neurology* (Vol. 11, Issue 12, pp. 676–686). Nature Publishing Group. https://doi.org/10.1038/nrneurol.2015.194

Enzinger, C., & Fazekas, F. (2015). Measuring gray matter and white matter damage in MS: Why this is not enough. *Frontiers in Neurology*, *6*(56), 1–4. https://doi.org/10.3389/fneur.2015.00056

Filippi, M., & Agosta, F. (2010). Imaging biomarkers in multiple sclerosis. *Journal of Magnetic Resonance Imaging*, *31*(4), 770–788. https://doi.org/10.1002/jmri.22102

Filippi, M., Cercignani, M., Inglese, M., Horsfield, M. A., & Comi, G. (2001). Diffusion tensor magnetic resonance imaging in multiple sclerosis. *Neurology*, *56*, 304–311.

Filippi, M., & Rocca, M. A. (2011). MR Imaging of Multiple Sclerosis. In *Radiology* (Vol. 259, Issue 3, pp. 659–681). https://doi.org/10.1148/radiol.11101362

Fisk, J. D., Pontefract, A., Ritvo, P. G., Archibald, C. J., & Murray, T. J. (1994). The Impact of Fatigue on Patients with Multiple Sclerosis. *Canadian Journal of Neurological Sciences / Journal Canadien Des Sciences Neurologiques*, *21*(1), 9–14. https://doi.org/10.1017/S0317167100048691

Gajamange, S., Raffelt, D., Dhollander, T., Lui, E., van der Walt, A., Kilpatrick, T., Fielding, J., Connelly, A., & Kolbe, S. (2018). Fibre-specific white matter changes in multiple sclerosis patients with optic neuritis. *NeuroImage: Clinical*, *17*, 60–68. https://doi.org/10.1016/j.nicl.2017.09.027

Garg, N., & Smith, T. W. (2015). An update on immunopathogenesis, diagnosis, and treatment of multiple sclerosis. *Brain and Behavior*, *5*(9), 1–13. https://doi.org/10.1002/brb3.362

Goldberg-Zimring, D., Mewes, A. U. J., Maddah, M., & Warfield, S. K. (2005). Diffusion tensor magnetic resonance imaging in multiple sclerosis. *Journal of Neuroimaging*, *15*, 68–81. https://doi.org/10.1177/1051228405283363

Goldenberg, M. M. (2012). Multiple Sclerosis Review. *Pharmacy & Therapeutics*, *37*(3), 175–184.

Gomes, L. dos R. (2011). *Validação da versão portuguesa da Escala de Impacto da Fadiga Modificada e da Escala de Severidade da Fadiga na Esclerose Múltipla* [Universidade do Minho]. http://repositorium.sdum.uminho.pt/handle/1822/17841

Granberg, T., Fan, Q., Treaba, C. A., Ouellette, R., Herranz, E., Mangeat, G., Louapre, C., Cohen-Adad, J., Klawiter, E. C., Sloane, J. A., & Mainero, C. (2017). In vivo characterization of cortical and white matter neuroaxonal pathology in early multiple sclerosis. *Brain*, *140*(11), 2912–2926. https://doi.org/10.1093/brain/awx247

Grussu, F., Schneider, T., Tur, C., Yates, R. L., Tachrount, M., Ianuş, A., Yiannakas, M. C., Newcombe, J., Zhang, H., Alexander, D. C., DeLuca, G. C., & Gandini Wheeler-Kingshott, C. A. M. (2017). Neurite dispersion: a new marker of multiple sclerosis spinal cord pathology? *Annals of Clinical and Translational Neurology*, *4*(9), 663–679. https://doi.org/10.1002/acn3.445

Hagiwara, A., Kamagata, K., Shimoji, K., Yokoyama, K., Andica, C., Hori, M., Fujita, S., Maekawa, T., Irie, R., Akashi, T., Wada, A., Suzuki, M., Abe, O., Hattori, N., & Aoki, S. (2019). White matter abnormalities in multiple sclerosis evaluated by quantitative synthetic MRI, diffusion tensor imaging, and neurite orientation dispersion and density imaging. *American Journal of Neuroradiology*, *40*(10), 1642–1648. https://doi.org/10.3174/ajnr.A6209

Haines, J. D., Inglese, M., & Casaccia, P. (2011). Axonal damage in multiple sclerosis. *Mount Sinai Journal of Medicine*, *78*(2), 231–243. https://doi.org/10.1002/msj.20246

Horbruegger, M., Loewe, K., Kaufmann, J., Wagner, M., Schippling, S., Pawlitzki, M., & Schoenfeld, M. A. (2019). Anatomically constrained tractography facilitates biologically plausible fiber reconstruction of the optic radiation in multiple sclerosis. *NeuroImage: Clinical*, *22*, 1–12. https://doi.org/10.1016/j.nicl.2019.101740

Jehna, M., Langkammer, C., Khalil, M., Fuchs, S., Reishofer, G., Fazekas, F., Ebner, F., & Enzinger, C. (2013). An Exploratory Study on the Spatial Relationship Between Regional Cortical Volume Changes and White Matter Integrity in Multiple Sclerosis. *Brain Connectivity*, *3*(3), 255–264. https://doi.org/10.1089/brain.2012.0108

Jenkinson, M., Pechaud, M., & Smith, S. (2002). BET2-MR-Based Estimation of Brain, Skull and Scalp Surfaces. In *Human Brain Mapping* (Vol. 17, Issue 2). www.fmrib.ox.ac.uk/analysis/research/bet

Jeurissen, B., Descoteaux, M., Mori, S., & Leemans, A. (2018). Tractography. *Proceedings of the International Society for Magnetic Resonance in Medicine*, *32*(4). https://doi.org/10.1002/nbm.3785

Klineova, S., & Lublin, F. D. (2018). Clinical course of multiple sclerosis. *Cold Spring Harbor Perspectives in Medicine*, *8*(9). https://doi.org/10.1101/cshperspect.a028928

Kocsis, J. D., Sasaki, M., Lankford, K. L., & Radtke, C. (2008). MULTIPLE SCLEROSIS: REMYELINATION. *CNS Regeneration*, 413–435. https://doi.org/10.1016/B978-012373994-0.50020-8

Koenig, K. A., Sakaie, K. E., Lowe, M. J., Lin, J., Stone, L., Bermel, R. A., Beall, E. B., Rao, S. M., Trapp, B. D., & Phillips, M. D. (2012). High spatial and angular resolution diffusion-weighted imaging reveals forniceal damage related to memory impairment. *Magnetic Resonance Imaging*, *31*(5), 695–699. https://doi.org/10.1016/j.mri.2012.10.030

Kolasa, M., Hakulinen, U., Brander, A., Hagman, S., Dastidar, P., Elovaara, I., & Sumelahti, M.-L. (2018). Diffusion tensor imaging and disability progression in multiple sclerosis: A 4-year follow-up study. *Brain and Behavior*, *9*, 1–10. https://doi.org/10.1002/brb3.1194

Kurtzke, J. F. (1983). Rating neurologic impairment in multiple sclerosis: An expanded disability status scale (EDSS). *Neurology*, *33*, 1444–1452.

Langdon, D. W., Amato, M. P., Boringa, J., Brochet, B., Foley, F., Fredrikson, S., Hämäläinen, P., Hartung, H. P., Krupp, L., Penner, I. K., Reder, A. T., & Benedict, R. H. B. (2012). Recommendations for a brief international cognitive assessment for multiple sclerosis (BICAMS). In *Multiple Sclerosis Journal* (Vol. 18, Issue 6, pp. 891–898). https://doi.org/10.1177/1352458511431076

Lee, C. Y., Huisinga, J. M., Choi, I. Y., Lynch, S. G., & Lee, P. (2020). Correlation between spinal cord diffusion tensor imaging and postural response latencies in persons with multiple sclerosis: A pilot study. *Magnetic Resonance Imaging*, *66*, 226–231. https://doi.org/10.1016/j.mri.2019.11.004

Lisa. (2017, June 7). *Multiple Sclerosis - Bowen can help many symptoms*. http://simplybowentherapy.com.au/multiple-sclerosis/

Love, S. (2006). Demyelinating diseases. In *Journal of Clinical Pathology* (Vol. 59, Issue 11, pp. 1151–1159). https://doi.org/10.1136/jcp.2005.031195

Margoni, M., Villani, U., Finos, L., Franciotta, S., Rubin, M., Nosadini, M., Sartori, S., Anglani, M. G., Causin, F., Perini, P., Rinaldi, F., Bertoldo, A., & Gallo, P. (2022). Neurite orientation dispersion and density imaging discloses early changes in the normal-appearing white matter in paediatric multiple sclerosis. In *Journal of Neurology, Neurosurgery and Psychiatry* (Vol. 93, Issue 3, pp. 332–334). BMJ Publishing Group. https://doi.org/10.1136/jnnp-2021-326355

Meyer-Moock, S., Feng, Y. S., Maeurer, M., Dippel, F. W., & Kohlmann, T. (2014). Systematic literature review and validity evaluation of the Expanded Disability Status Scale (EDSS) and the Multiple Sclerosis Functional Composite (MSFC) in patients with multiple sclerosis. *BMC Neurology*, *14*(58), 1–10. https://doi.org/10.1186/1471-2377-14-58

Mustafi, S., Harezlak, J., Kodiweera, C., Randolph, J., Ford, J., Wishart, H., & Wu, Y. C. (2019). Detecting white matter alterations in multiple sclerosis using advanced diffusion magnetic resonance imaging. *Neural Regeneration Research*, *14*(1), 114–123. https://doi.org/10.4103/1673-5374.243716

Novo, A. M., Batista, S., Alves, C., Dalmeida, O. C., Marques, I. B., Macario, C., Santana, I., Sousa, L., Castelo-Branco, M., & Cunha, L. (2018). Research the neural basis of fatigue in multiple sclerosis amultimodalmri approach. *Neurology: Clinical Practice*, *8*(6), 492–500. https://doi.org/10.1212/CPJ.0000000000000545

Oh, J., Vidal-Jordana, A., & Montalban, X. (2018). Multiple sclerosis: Clinical aspects. *Current Opinion in Neurology*, *31*(6), 752–759. https://doi.org/10.1097/WCO.0000000000000622

Ontaneda, X. D., Sakaie, X. K., Lin, X. J., Wang, X.-F., Lowe, M. J., Phillips, X. M. D., & Fox, X. R. J. (2017). Measuring Brain Tissue Integrity during 4 Years Using Diffusion Tensor

Imaging. *American Jounral of Neuroradiology*, *38*, 31–38. https://doi.org/10.3174/ajnr.A4946

Pagani, E., Rocca, M. A., de Meo, E., Horsfield, M. A., Colombo, B., Rodegher, M., Comi, G., & Filippi, M. (2020). Structural connectivity in multiple sclerosis and modeling of disconnection. *Multiple Sclerosis Journal*, *26*(2), 220–232. https://doi.org/10.1177/1352458518820759

Patrikios, P., Stadelmann, C., Kutzelnigg, A., Rauschka, H., Schmidbauer, M., Laursen, H., Sorensen, P. S., Brück, W., Lucchinetti, C., & Lassmann, H. (2006). Remyelination is extensive in a subset of multiple sclerosis patients. *Brain*, *129*, 3165–3172. https://doi.org/10.1093/brain/awl217

Pernet, C. R., Wilcox, R., Rousselet, G. A., Finch, H., Budden, J. S., & Smithson, M. (2013). Robust correlation analyses: false positive and power validation using a new open source Matlab toolbox. *Frontiers in Psychology*, *3*, 1–18. https://doi.org/10.3389/fpsyg.2012.00606

Radetz, A., Mladenova, K., Ciolac, D., Gonzalez-Escamilla, G., Fleischer, V., Ellwardt, E., Krämer, J., Bittner, S., Meuth, S. G., Muthuraman, M., Groppa, S., Takeuchi, H., de Meo, E., Raffaele Hospital, S., Emanuele, I. D., & Groppa segroppa, S. (2021). Linking Microstructural Integrity and Motor Cortex Excitability in Multiple Sclerosis microstructure imaging using advanced biophysical models to forecast excitability alterations in neuroinflammation. *Frontiers in Immunology*, *12*, 1–11. https://doi.org/10.3389/fimmu.2021.748357

Rahmanzadeh, R., Lu, P.-J., Barakovic, M., Weigel, M., Maggi, P., Nguyen, T. D., Schiavi, S., Daducci, A., Rosa, F. la, Schaedelin, S., Absinta, M., Reich, D. S., Sati, P., Wang, Y., Cuadra, M. B., Radue, E.-W., Kuhle, J., Kappos, L., & Granziera, C. (2021). Myelin and axon pathology in multiple sclerosis assessed by myelin water and multi-shell diffusion imaging. *Brain*, *144*(6), 1684–1696. https://doi.org/10.1093/brain/awab088/6164965

Rane, S. (2009). *Diffusion tensor imaging at long diffusion time* [Georgia Institute of Technology]. https://www.researchgate.net/publication/27544487

Rashid, W., Hadjiprocopis, A., Davies, G., Griffin, C., Chard, D., Tiberio, M., Altmann, D., Wheeler-Kingshott, C., Tozer, D., Thompson, A., & Miller, D. H. (2008). Longitudinal evaluation of clinically early relapsing-remitting multiple sclerosis with diffusion

tensor imaging. *Journal of Neurology*, *255*(3), 390–397. https://doi.org/10.1007/s00415-008-0678-0

Rovaris, M., & Filippi, M. (2007). Diffusion tensor MRI in multiple sclerosis. *Journal of Neuroimaging*, *17*, 27–30. https://doi.org/10.1111/j.1552-6569.2007.00133.x

Ryan, J., Woods, R. L., Britt, C. J., Murray, A. M., Shah, R. C., Reid, C. M., Wolfe, R., Nelson, M. R., Orchard, S. G., Lockery, J. E., Trevaks, R. E., & Storey, E. (2020). Normative Data for the Symbol Digit Modalities Test in Older White Australians and Americans, African-Americans, and Hispanic/Latinos. *Journal of Alzheimer's Disease Reports*, *4*, 313–323. https://doi.org/10.3233/ADR-200194

Sacco, S., Caverzasi, E., Papinutto, N., Cordano, C., Bischof, A., Gundel, T., Cheng, S., Asteggiano, C., Kirkish, G., Mallott, J., Stern, W. A., Bastianello, S., Bove, R. M., Gelfand, J. M., Goodin, D. S., Green, A. J., Waubant, E., Wilson, M. R., Zamvil, S. S., … Henry, R. G. (2020). Neurite orientation dispersion and density imaging for assessing acute inflammation and lesion evolution in MS. *American Journal of Neuroradiology*, *41*(12), 2219–2226. https://doi.org/10.3174/ajnr.A6862

Sämann, P. G., Knop, M., Golgor, E., Messler, S., Czisch, M., & Weber, F. (2012). Brain Volume and Diffusion Markers as Predictors of Disability and Short-Term Disease Evolution in Multiple Sclerosis. *American Journal of Neuroradiology*, *33*, 1356–1362. https://doi.org/10.3174/ajnr.A2972

Schmierer, K., Altmann, D. R., Kassim, N., Kitzler, H., Kerskens, C. M., Doege, C. A., Aktas, O., Lünemann, J. D., Miller, D. H., Zipp, F., & Villringer, A. (2004). Progressive change in primary progressive multiple sclerosis normal-appearing white matter: A serial diffusion magnetic resonance imaging study. *Multiple Sclerosis*, *10*(2), 182–187. https://doi.org/10.1191/1352458504ms996oa

Schneider, T., Brownlee, W., Zhang, H., Ciccarelli, O., Miller, D. H., & Gandini Wheeler-Kingshott, C. (2017). Sensitivity of multi-shell NODDI to multiple sclerosis white matter changes: a pilot study. *Functional Neurology*, *32*(2), 97–101. http://www.nitrc.org/pro-

Smith, R. E., Tournier, J. D., Calamante, F., & Connelly, A. (2013). SIFT: Spherical-deconvolution informed filtering of tractograms. *NeuroImage*, *67*, 298–312. https://doi.org/10.1016/J.NEUROIMAGE.2012.11.049

Smith, S. M. (2002). Fast Robust Automated Brain Extraction. *Human Brain Mapping*, *17*, 143–155. https://doi.org/10.1002/hbm.10062

Smith, S. M., Jenkinson, M., Johansen-Berg, H., Rueckert, D., Nichols, T. E., Mackay, C. E., Watkins, K. E., Ciccarelli, O., Cader, M. Z., Matthews, P. M., & Behrens, T. E. J. (2006). Tract-based spatial statistics: Voxelwise analysis of multi-subject diffusion data. *NeuroImage*, *31*(4), 1487–1505. https://doi.org/10.1016/J.NEUROIMAGE.2006.02.024

Smith, S. M., Jenkinson, M., Woolrich, M. W., Beckmann, C. F., Behrens, T. E. J., Johansen-Berg, H., Bannister, P. R., de Luca, M., Drobnjak, I., Flitney, D. E., Niazy, R. K., Saunders, J., Vickers, J., Zhang, Y., de Stefano, N., Brady, J. M., & Matthews, P. M. (2004). Advances in functional and structural MR image analysis and implementation as FSL. *NeuroImage*, *23*, 208–219. https://doi.org/10.1016/J.NEUROIMAGE.2004.07.051

Soares, J. M., Marques, P., Alves, V., & Sousa, N. (2013). A hitchhiker's guide to diffusion tensor imaging. *Frontiers in Neuroscience*, *7*, 1–14. https://doi.org/10.3389/fnins.2013.00031

Sousa, C., Rigueiro-Neves, M., Miranda, T., Alegria, P., Vale, J., Passos, A. M., Langdon, D., & Sá, M. J. (2018). Validation of the brief international cognitive assessment for multiple sclerosis (BICAMS) in the Portuguese population with multiple sclerosis 11 Medical and Health Sciences 1109 Neurosciences. *BMC Neurology*, *18*(172), 1–7. https://doi.org/10.1186/s12883-018-1175-4

Spano, B., Giulietti, G., Pisani, V., Morreale, M., Tuzzi, E., Nocentini, U., Francia, A., Caltagirone, C., Bozzali, M., & Cercignani, M. (2018). Disruption of neurite morphology parallels MS progression. *Neurology: Neuroimmunology and NeuroInflammation*, *5*(6), 1–10. https://doi.org/10.1212/NXI.0000000000000502

Stegen, S., Stepanov, I., Cookfair, D., Schwartz, E., Hojnacki, D., Weinstock-Guttman, B., & Benedict, R. H. B. (2010). Validity of the California verbal learning test-II in multiple sclerosis. *Clinical Neuropsychologist*, *24*(2), 189–202. https://doi.org/10.1080/13854040903266910

Tariq, M., Schneider, T., Alexander, D. C., Gandini Wheeler-Kingshott, C. A., & Zhang, H. (2016). Bingham-NODDI: Mapping anisotropic orientation dispersion of neurites using diffusion MRI. *NeuroImage*, *133*, 207–223. https://doi.org/10.1016/j.neuroimage.2016.01.046

Thompson, A. J., Banwell, B. L., Barkhof, F., Carroll, W. M., Coetzee, T., Comi, G., Correale, J., Fazekas, F., Filippi, M., Freedman, M. S., Fujihara, K., Galetta, S. L., Hartung, H. P., Kappos, L., Lublin, F. D., Marrie, R. A., Miller, A. E., Miller, D. H., Montalban, X., … Cohen, J. A. (2018). Diagnosis of multiple sclerosis: 2017 revisions of the McDonald criteria. In *The Lancet Neurology* (Vol. 17, Issue 2, pp. 162–173). Lancet Publishing Group. https://doi.org/10.1016/S1474-4422(17)30470-2

Tournier, J. D., Smith, R., Raffelt, D., Tabbara, R., Dhollander, T., Pietsch, M., Christiaens, D., Jeurissen, B., Yeh, C. H., & Connelly, A. (2019). MRtrix3: A fast, flexible and open software framework for medical image processing and visualisation. *NeuroImage*, *202*, 116137–7. https://doi.org/10.1016/J.NEUROIMAGE.2019.116137

Vigh-Teichmann, I., & Vigh, B. (1983). The System of Cerebrospinal Fluid-Contacting Neurons. *Arch. Histol. Jap*, *46*(4), 427–468.

Walton, C., King, R., Rechtman, L., Kaye, W., Leray, E., Marrie, R. A., Robertson, N., la Rocca, N., Uitdehaag, B., van der Mei, I., Wallin, M., Helme, A., Angood Napier, C., Rijke, N., & Baneke, P. (2020). Rising prevalence of multiple sclerosis worldwide: Insights from the Atlas of MS, third edition. *Multiple Sclerosis Journal*, *26*(14), 1816–1821. https://doi.org/10.1177/1352458520970841

Winkler, A. M., Ridgway, G. R., Webster, M. A., Smith, S. M., & Nichols, T. E. (2014). Permutation inference for the general linear model. *NeuroImage*, *92*, 381–397. https://doi.org/10.1016/J.NEUROIMAGE.2014.01.060

Yeh, C. H., Jones, D. K., Liang, X., Descoteaux, M., & Connelly, A. (2021). Mapping Structural Connectivity Using Diffusion MRI: Challenges and Opportunities. In *Journal of Magnetic Resonance Imaging* (Vol. 53, Issue 6, pp. 1666–1682). John Wiley and Sons Inc. https://doi.org/10.1002/jmri.27188

Yeh, F. C., Zaydan, I. M., Suski, V. R., Lacomis, D., Richardson, R. M., Maroon, J. C., & Barrios-Martinez, J. (2019). Differential tractography as a track-based biomarker for neuronal injury. *NeuroImage*, *202*, 1–12. https://doi.org/10.1016/j.neuroimage.2019.116131

Yu, H. J., Christodoulou, C., Bhise, V., Greenblatt, D., Patel, Y., Serafin, D., Maletic-Savatic, M., Krupp, L. B., & Wagshul, M. E. (2012). Multiple white matter tract abnormalities underlie cognitive impairment in RRMS. *NeuroImage*, *59*(4), 3713–3722. https://doi.org/10.1016/j.neuroimage.2011.10.053

Zhang, H., Hubbard, P. L., Parker, G. J. M., & Alexander, D. C. (2011). Axon diameter mapping in the presence of orientation dispersion with diffusion MRI. *NeuroImage*, *56*(3), 1301–1315. https://doi.org/10.1016/j.neuroimage.2011.01.084

Zhang, H., Schneider, T., Wheeler-Kingshott, C. A., & Alexander, D. C. (2012). NODDI: Practical in vivo neurite orientation dispersion and density imaging of the human brain. *NeuroImage*, *61*(4), 1000–1016. https://doi.org/10.1016/j.neuroimage.2012.03.072

Annexes

A. Tractography Results

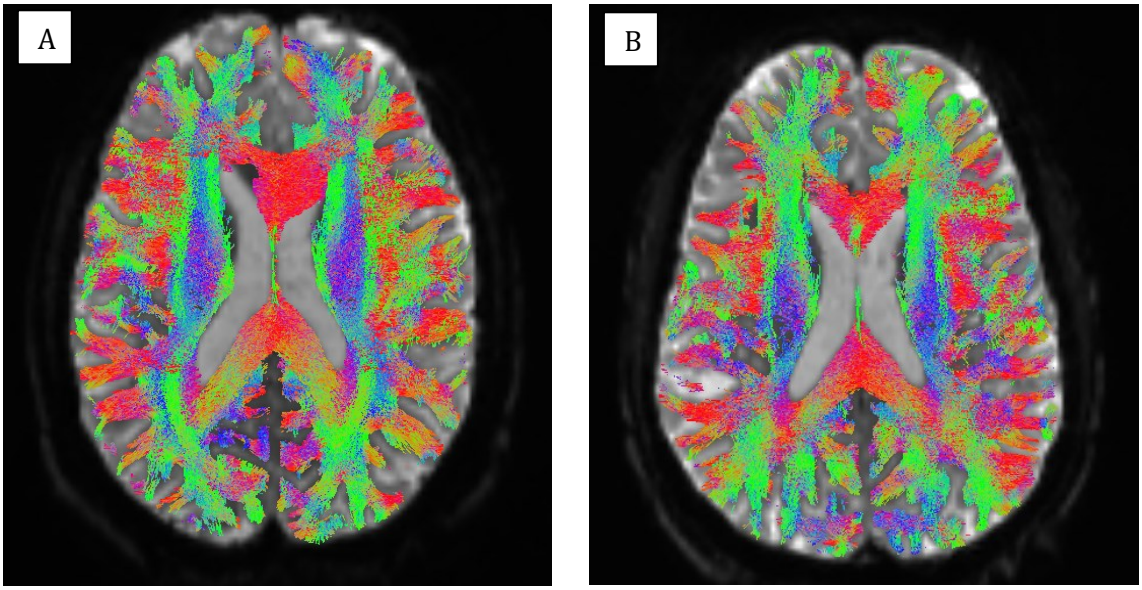

Fig. 40 Tractogram overlaid on a diffusion image from age and gender-matched A) healthy control and B) MS patient. Color code: red is left-to-right orientation, green is posterior-to-anterior orientation and blue is inferior-to-superior orientation.

B. Connectome Results

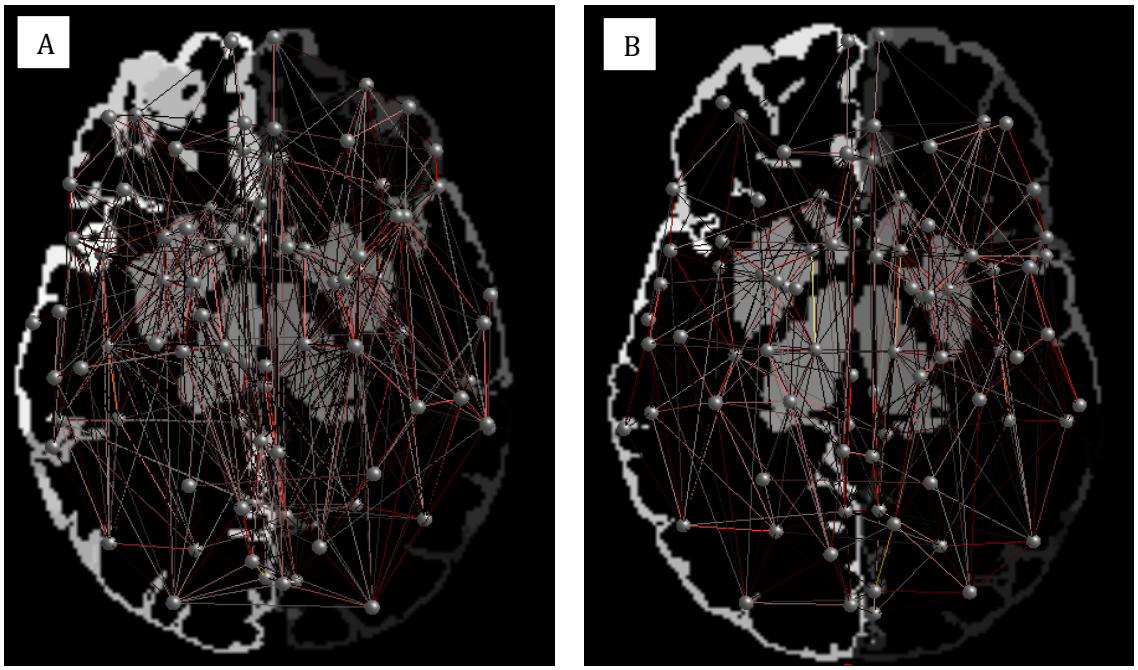

Fig. 41 Connectome overlaid on an axial plane of the parcellation image from age and gender-matched A) healthy control and B) MS patient. The strength threshold is 0.1 (edges with a connection strength which is less than 0.1 are not shown).

C. TBSS results

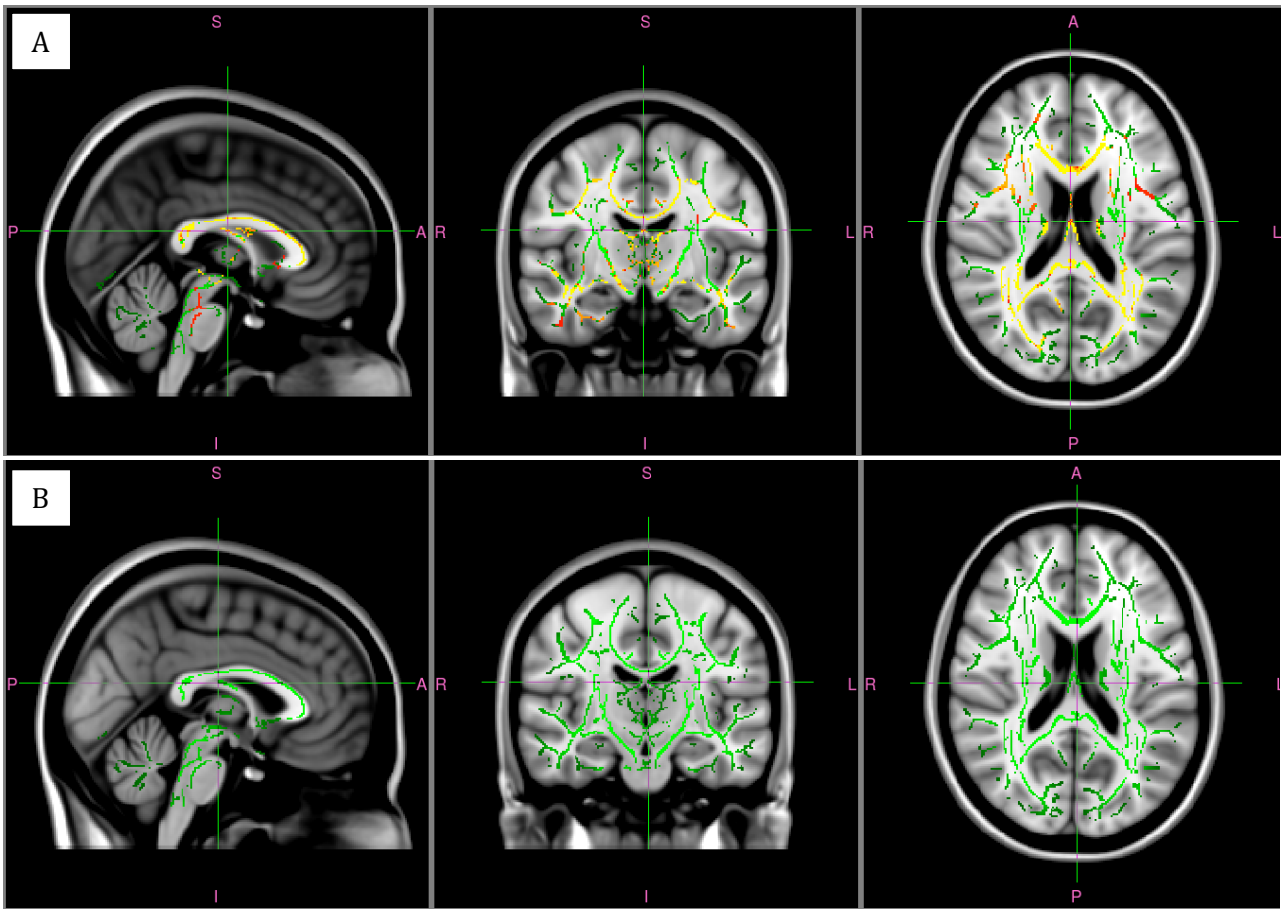

Fig. 42 Sagittal, coronal, and axial view of TBSS results of FA, which show significant differences between MS patients and healthy controls with A) the CNT>MSC contrast and B) the MSC>CNT contrast for p-values corrected for multiple comparisons with Family Wise Error (FWE). In green, is the mean FA skeleton for all participants; in red-yellow are the differences between the two groups. The scale of the red-yellow colourmap is 0.95-1 and the maps are for 1-p-value. Thus, a lower p-value (more statistically significant) is represented in yellow and only statistically significant differences are shown (p-value<0.05). These skeletons are overlaid on a MNI152 T1-weighted template. Note that the MSC>CNT shows no statistically significant differences.

D. Correlations between cognitive and neuropsychological tests and diffusion metrics

Correlations between EDSS and diffusion metrics

FA			ADC			ODI			NDI		
ROI	**rho**	**p_{UNC}**	**ROI**	**rho**	**p_{UNC}**	**ROI**	**rho**	**p_{UNC}**	**ROI**	**rho**	**p_{UNC}**
LAOG	0.516	0.0284	**LCE**	0.666	0.0026	**LC**	-0.666	0.0026	**LCC**	-0.519	0.0273
LCC	-0.565	0.0146	**LCumWM**	0.505	0.0327	**LCC**	0.520	0.0269	**LLV**	-0.551	0.0177
LFP	0.496	0.0364	**LFG**	0.507	0.0318	**LTP**	-0.553	0.0174	**LTP**	-0.525	0.0254
LFG	-0.640	0.0042	**LPhG**	0.545	0.0194	**RAA**	-0.556	0.0166	**RBF**	-0.619	0.0061
LOrPOFIFG	-0.531	0.0232	**RCumWM**	0.475	0.0465	**RC**	-0.628	0.0052	**OC**	-0.577	0.0122
LTmP	-0.489	0.0394	**RLG**	0.480	0.0437	**RTP**	-0.569	0.0137			
RAA*	0.769*	0.0002*	**BS**	0.658	0.0030	**ThirdV**	-0.490	0.0389			
RC	0.469	0.0495									
RLG	-0.471	0.0483									
RPIns	-0.523	0.0261									
RPOrG	-0.484	0.0420									
CVLIV	-0.500	0.0345									
BS	-0.486	0.0410									

Table 14 Statistics for the correlations between EDSS and diffusion metrics (FA, ADC, ODI and NDI). The table only shows statistically significant correlations for uncorrected p-values ($p_{UNC}<0.05$). Asterisks represent ROIs where the correlation is statistically significant for FDR-corrected p-values (* $p<0.05$). In each column, the maximum (negative and/or positive) correlation and its corresponding p-value are the ones underlined. LAOG = Left Anterior Orbital Gyrus; LCC = Left Calcarine Cortex; LFP = Left Frontal Pole; LFG = Left Fusiform Gyrus; LOrPOFIFG = Left Orbital part of the Inferior Frontal Gyrus; LTmP = Left Temporal Pole; RAA = Right Accumbens Area; R/LC = Right/Left Caudate; RLG = Right Lingual Gyrus; RPIns = Right Posterior Insula; RPOrG = Right Posterior Orbital Gyrus; CVLIV = Cerebellar Vermal Lobules I-V; BS = Brain stem; LCE = Left Cerebellum Exterior; R/LCumWM = Right/Left Cerebellum White Matter; LPhG = Left Parahippocampal Gyrus; RCumWM = Right Cerebellum White Matter; R/LTP = Right/Left Thalamus Proper; ThirdV = Third Ventricle; LLV = Left Lateral Ventricle; RBF = Right Basal Forebrain; OC = Optic Chiasm.

Correlations between MFIS and diffusion metrics												
FA			**ADC**			**ODI**			**NDI**			
ROI	**r**	**p_{UNC}**	**ROI**	**r**	**p_{UNC}**	**ROI**	**r**	**p_{UNC}**	**ROI**	**r**	**p_{UNC}**
LAG	-0.523	0.0261	**LPOrG**	0.508	0.0314	**LCC**	0.480	0.0439	**LAOG**	0.549	0.0183
LEA	-0.538	0.0212	**LSA**	0.486	0.0408	**LMFC**	0.496	0.0362	**LCO**	0.491	0.0384
LPT	-0.518	0.0277				**LMOrG**	0.619	0.0061	**RPOrG**	0.517	0.0282
LPG	-0.512	0.0299				**LPCG**	0.492	0.0382	**RTTG**	0.726	0.0006
LPIns	-0.504	0.0330				**LPIns**	0.519	0.0273			
LSA	-0.555	0.0167				**LPO**	0.483	0.0424			
RMTG	-0.526	0.0250				**LPOrG***	0.718*	0.0008*			
RPIns	-0.489	0.0394				**LPT**	0.564	0.0147			
BS	-0.527	0.0246				**LTmP**	0.503	0.0333			
						RCE	0.504	0.0330			
						RCO	0.544	0.0196			
						RFG*	0.721*	0.0007*			
						RMTG*	0.675*	0.0021*			
						ROFG	0.490	0.0389			
						RPIns	0.652	0.0034			
						RPOrG	0.482	0.0428			
						RPP	0.542	0.0201			
						RPT	0.543	0.0200			

Table 15 Statistics for the correlations between MFIS and diffusion metrics (FA, ADC, ODI and NDI). The table only shows statistically significant correlations for uncorrected p-values (p_{UNC}<0.05). Asterisks represent ROIs where the correlation is statistically significant for FDR-corrected p-values (* p<0.05). In each column, the maximum (negative and/or positive) correlation and its corresponding p-value are the ones underlined. LAG = Left Angular Gyrus; LEA = Left Entorhinal Area; R/LPT = Right/Left Planum Temporale; LPG = Left Postcentral Gyrus; LSA = Left Subcallosal Area; RMTG = Left Middle Temporal Gyrus; R/LPIns = Right/Left Posterior Insula; BS = Brain Stem; R/LPOrG = Right/Left Posterior Orbital Gyrus; LCC = Left Calcarine Cortex; LMFC = Left Medial Frontal Cortex; LMOrG = Left Medial Orbital Gyrus; LTmP = Left Temporal pole; RCE = Right Cerebellum Exterior; R/LCO = Right/Left Central Operculum; RFG = Right Fusiform Gyrus; ROFG = Right Occipital Fusiform Gyrus; RPP = Right Planum Polare; LAOG = Left Anterior Orbital Gyrus; RTTG = Right Transverse Temporal Gyrus.

Correlations between SDMT and diffusion metrics												
FA			**ADC**			**ODI**			**NDI**			
ROI	**r**	**p_{UNC}**	**ROI**	**r**	**p_{UNC}**	**ROI**	**r**	**p_{UNC}**	**ROI**	**r**	**p_{UNC}**
LAIns	0.483	0.0421	**LAA**	0.644	0.0040	**LAIns**	-0.631	0.0050	**LAA***	-0.592*	0.0096*
LGR	0.473	0.0477	**LPP**	-0.528	0.0243	**LCE**	-0.522	0.0262	**LACG***	-0.688*	0.0016*
LLOG	0.547	0.0189	**LSMC**	-0.634	0.0048	**LFG**	-0.504	0.0330	**LAOG***	-0.483*	0.0424*
LMFG	0.664	0.0027	**LTmP**	-0.502	0.0337	**LMFG**	-0.600	0.0085	**LCO***	-0.568*	0.0139*
LOPOFIFG	0.580	0.0116	**RAA**	0.562	0.0153	**LMTG**	-0.621	0.0060	**LFO***	-0.576*	0.0123*
LPP	0.498	0.0355	**RACG**	-0.553	0.0173	**LOPOFIFG**	-0.591	0.0098	**LLOG***	-0.474*	0.0471*
LSMC	0.707	0.0010	**RCO**	-0.562	0.0153	**LPOrG**	-0.481	0.0433	**LMCG***	-0.580*	0.0117*
LSPL	0.560	0.0157	**RLOG**	-0.571	0.0133	**LPP**	-0.557	0.0162	**LOrPOFIFG***	-0.616*	0.0065*

LTmP	0.506	0.0321	**RMCG**	-0.520	0.0270	**LSMC**	-0.628	0.0053	**LPC***	-0.489*	0.0396*
RCC	0.542	0.0202	**RMFG**	-0.470	0.0490	**LSTG**	-0.539	0.0210	**LPIns***	-0.498*	0.0353*
RMOG	-0.483	0.0425	**RSFG**	-0.481	0.0436	**RAOG**	-0.491	0.0384	**LPO***	-0.488*	0.0398*
RPO	0.518	0.0278	**RSMC**	-0.553	0.0172	**RCE**	-0.553	0.0173	**LPOrG***	-0.530*	0.0235*
RSMC	0.486	0.0410				**RCumWM**	-0.525	0.0253	**LPreGMS***	-0.635*	0.0046*
RSTG	0.568	0.0139				**RMOrG**	-0.480	0.0440	**LSMC***	-0.542*	0.0202*
RTmP	0.564	0.0149				**RPO**	-0.624	0.0057	**LTmP***	-0.545*	0.0194*
						RSA	-0.510	0.0307	**LTPOFTIFG***	-0.494*	0.0370*
						RSTG	-0.476	0.0458	**LTTG***	-0.569*	0.0136*
									RAA*	-0.542*	0.0202*
									RACG*	-0.744*	0.0004*
									RC*	-0.516*	0.0283*
									RCO*	-0.628*	0.0053*
									RLOG*	-0.547*	0.0188*
									RMCG*	-0.483*	0.0426*
									RMFG*	-0.546*	0.0190*
									ROPOFIFG*	-0.675*	0.0021*
									RPO*	-0.534*	0.0223*
									RPreG*	-0.520*	0.0268*
									RPu*	-0.475*	0.0465*
									RSFG*	-0.548*	0.0186*
									RSFGMS*	-0.501*	0.0342*
									RSMC*	-0.526*	0.0250*
									RTmP*	-0.582*	0.0113*

Table 16 Statistics for the correlations between SDMT and diffusion metrics (FA, ADC, ODI and NDI). The table only shows statistically significant correlations for uncorrected p-values ($p_{UNC}<0.05$). Asterisks represent ROIs where the correlation is statistically significant for FDR-corrected p-values (* $p<0.05$). In each column, the maximum (negative and/or positive) correlation and its corresponding p-value are the ones underlined. LAIns = Left Anterior Insula; LGR = Left Gyrus Rectus; R/LLOG = Right/Left Lateral Orbital Gyrus; R/LMFG = Right/Left Middle Frontal Gyrus; R/LOPOFIFG = Right/Left Opercular part of the Inferior Frontal Gyrus; LPP = Left Planum Polare; R/LSMC = Right/Left Supplementary Motor Cortex; LSPL = Left Superior Parietal Lobule; R/LTmP = Right/Left Temporal Pole; RCC = Right Calcarine Cortex; RMOG = Right Middle Occipital Gyrus; R/LPO = Right/Left Parietal Operculum; R/LSTG = Right/Left Superior Temporal Gyrus; R/LAA = Right/Left Accumbens Area; R/LACG = Right/Left Anterior Cingulate Gyrus; R/LCO = Right/Left Central Operculum; R/LMCG = Right/Left Middle Cingulate Gyrus; RSFG = Right Superior Frontal Gyrus; R/LCE = Right/Left Cerebellum Exterior; LFG = Left Fusiform Gyrus; LMTG = Left Middle Temporal Gyrus; LPOrG = Left Posterior Orbital Gyrus; R/LAOG = Right/Left Anterior Orbital Gyrus; RCumWM = Right Cerebellum White Matter; RMOrG = Right Medial Orbital Gyrus; RSA = Right Subcallosal Area; LFO = Left Frontal Operculum; LOrPOFIFG = Left Orbital part of the Inferior Frontal Gyrus; LPC = Left Precuneus; LPIns = Left Posterior Insula; LPreGMS = Left Precentral Gyrus Medial Segment; LTPOFTIFG = Left Triangular part of the Inferior Frontal Gyrus; LTTG = Left Transverse Temporal Gyrus; RC = Right Caudate; RPreG = Right Precentral Gyrus; RPu = Right Putamen; RSFGMS = Right Superior Frontal Gyrus Medial Segment.

Correlations between CVLT and diffusion metrics

FA			ADC			ODI			NDI		
ROI	**r**	**p_{UNC}**	**ROI**	**r**	**p_{UNC}**	**ROI**	**r**	**p_{UNC}**	**ROI**	**r**	**p_{UNC}**
LGR	0.567	0.0142	**LAm**	0.586	0.0105	**LAIns**	-0.469	0.0495	**LLV**	-0.506	0.0322
RAOG	0.503	0.0334	**LLV**	-0.481	0.0434	**LFO**	-0.527	0.0247	**LMTG**	-0.486	0.0408
CVLVIVII	0.489	0.0397	**LOrPOFIFG**	-0.490	0.0391	**LMOrG**	-0.475	0.0462	**LOrPOFIFG**	-0.627	0.0053
CSF	0.480	0.0437	**RLV**	-0.491	0.0386	**LOPOFIFG**	-0.526	0.0249	**LPT**	-0.503	0.0335
	CSF	-0.557		0.0163		**LOrPOFIFG**	-0.555	0.0168	**LPOrG**	-0.564	0.0148
						LPOrG	-0.553	0.0173	**LTmP**	-0.596	0.0090
						LPP	-0.586	0.0106	**RFO**	-0.539	0.0209
						LPT	-0.515	0.0288	**RLV**	-0.529	0.0239
						REA	-0.476	0.0458	**RLOG**	-0.483	0.0421
						RMOrG	-0.477	0.0453	**ROPOFIFG**	-0.518	0.0277
									ROrPOFIFG	-0.580	0.0116
									RPT	-0.495	0.0368
									RPO	-0.494	0.0370
									RPOrG	-0.472	0.0477
									RSTG	-0.494	0.0373
									CSF	-0.574	0.0128

Table 17 Statistics for the correlations between CVLT and diffusion metrics (FA, ADC, ODI and NDI). The table only shows statistically significant correlations for uncorrected p-values ($p_{UNC}<0.05$). Asterisks represent ROIs where the correlation is statistically significant for FDR-corrected p-values (* $p<0.05$). In each column, the maximum (negative and/or positive) correlation and its corresponding p-value are the ones underlined. LGR = Left Gyrus Rectus; RAOG = Right Anterior Orbital Gyrus; CVLVVIVII = Cerebellar Vermal Lobules VI-VII; CSF = Cerebrospinal Fluid; Lam = Left Amygdala; R/LLV = Right/Left Lateral Ventricle; R/LOrPOFIFG = Right/Left Orbital part of the Inferior Frontal Gyrus; LAIns = Left Anterior Insula; R/LFO = Right/Left Frontal Operculum; R/LMOrG = Right/Left Medial Orbital Gyrus; R/LOPOFIFG = Right/Left Opercular part of the Inferior Frontal Gyrus; R/LPOrG = Right/Left Posterior Orbital Gyrus; LPP = Left Planum Polare; R/LPT = Right/Left Planum Temporale; REA = Right Entorhinal Area; LMTG = Left Middle Temporal Gyrus; LTmP = Left Temporal Pole; RLOG = Right Lateral Orbital Gyrus; RPO = Right Parietal Operculum; RSTG = Right Superior Temporal Gyrus.

Correlations between BVMT and diffusion metrics

FA			ADC			ODI			NDI		
ROI	**r**	**p_{UNC}**	**ROI**	**r**	**p_{UNC}**	**ROI**	**r**	**p_{UNC}**	**ROI**	**r**	**p_{UNC}**
LAIns	0.508	0.0313	**LLOG**	-0.489	0.0396	**LAG**	-0.500	0.0345	**LAA**	-0.509	0.0309
LGR	0.510	0.0305	**LPreGMS**	-0.488	0.0400	**LAIns**	-0.675	0.0021	**LACG***	-0.701*	0.0012*
LPO	0.479	0.0444	**LPP**	-0.522	0.0264	**LCE**	-0.508	0.0316	**LCO***	-0.566*	0.0143*
LSMC	0.723	0.0007	**LSMC**	-0.678	0.0020	**LMFC**	-0.638	0.0044	**LMCG***	-0.580*	0.0117*
LSPL	0.636	0.0046	**LTmP**	-0.577	0.0122	**LMFG**	-0.581	0.0115	**LMFG***	-0.571*	0.0134*
LTmP	0.490	0.0388	**RAA**	0.618	0.0063	**LMTG**	-0.504	0.0331	**LOPOFIFG**	-0.528	0.0242
RPO	0.478	0.0449	**RCO**	-0.503	0.0335	**LOPOFIFG**	-0.543	0.0199	**LOrPOFIFG***	-0.647*	0.0037*

RPreGMS	0.483	0.0421	**RLG**	-0.490	0.0388	**LOrPOFIFG**	-0.490	0.0391	**LPT**	-0.475	0.0463
RSPL	0.524	0.0255	**RLOG**	-0.611	0.0071	**LPO**	-0.545	0.0193	**LPG**	-0.473	0.0475
RTmP	0.584	0.0110	**RSFG**	-0.480	0.0440	**LPOrG**	-0.474	0.0467	**LPGMS**	-0.472	0.0480
CSF	0.490	0.0389	**RTmP**	-0.501	0.0343	**LPP**	-0.603	0.0080	**LPO**	-0.495	0.0366
			CSF	-0.508	0.0314	**LPT**	-0.497	0.0357	**LPreG**	-0.509	0.0311
						LSMC	-0.602	0.0082	**LPreGMS**	-0.546	0.0191
						LSTG	-0.507	0.0319	**LSFG**	-0.503	0.0333
						LTPOFTIFG	-0.549	0.0182	**LSFGMS**	-0.552	0.0175
						LTTG	-0.527	0.0245	**LSMC***	-0.597*	0.0089*
						RMFC	-0.603	0.0081	**LSOG**	-0.494	0.0373
						RMOrG	-0.486	0.0408	**LTmP**	-0.513	0.0294
						RPO	-0.548	0.0185	**LTPOFTIFG**	-0.472	0.0478
						RPOrG	-0.524	0.0258	**LTTG***	-0.567*	0.0142*
						RSFG	-0.504	0.0330	**RAA**	-0.528	0.0244
						RTmP	-0.524	0.0255	**RACG***	-0.677*	0.0020*
									RCO*	-0.589*	0.0101*
									RMFG*	-0.585*	0.0107*
									ROPOFIFG*	-0.628*	0.0052*
									ROrPOFIFG	-0.473	0.0473
									RPT	-0.488	0.0399
									RPG	-0.499	0.0349
									RPO*	-0.623*	0.0057*
									RPreG	-0.498	0.0353
									RSFG*	-0.657*	0.0030*
									RSFGMS*	-0.566*	0.0143*
									RSMC	-0.544	0.0196
									RTmP*	-0.563*	0.0149*

Table 18 Statistics for the correlations between BVMT and diffusion metrics (FA, ADC, ODI and NDI). The table only shows statistically significant correlations for uncorrected p-values (p_{UNC}<0.05). Asterisks represent ROIs where the correlation is statistically significant for FDR-corrected p-values (* p<0.05). In each column, the maximum (negative and/or positive) correlation and its corresponding p-value are the ones underlined. LAIns = Left Anterior Insula; LGR = Left Gyrus Rectus; R/LPO = Right/Left Parietal Operculum; R/LSMC = Right/Left Supplementary Motor Cortex; R/LSPL = Right/Left Superior Parietal Lobule; R/LTmP = Right/Left Temporal Pole; R/LPreGMS = Right/Left Precentral Gyrus Medial Segment; CSF = Cerebrospinal Fluid; R/LLOG = Right/Left Lateral Orbital Gyrus; LPP = Left Planum Polare; R/LAA = Right/Left Accumbens Area; R/LCO = Right/Left Central Operculum; RLG = Right Lingual Gyrus; R/LSFG = Right/Left Superior Frontal Gyrus; LAG = Left Angular Gyrus; LCE = Left Cerebellum Exterior; R/LMFC = Left/Right Medial Frontal Cortex; R/LMFG = Right/Left Middle Frontal Gyrus; LMTG = Left Middle Temporal Gyrus; R/LOPOFIFG = Right/Left Opercular part of the Inferior Frontal Gyrus; R/LOrPOFIFG = Right/Left Orbital part of the Inferior Frontal Gyrus; R/LPOrG = Right/Left Posterior Orbital Gyrus; R/LPT = Right/Left Planum Temporale; LSG = Left Supramarginal Gyrus; LTPOFTIFG = Left Triangular part of the Inferior Frontal Gyrus; LTTG = Left Transverse Temporal Gyrus; RMOrG = Right Medial Orbital Gyrus; R/LACG Right/Left Anterior Cingulate Gyrus; LMCG = Left Middle Cingulate Gyrus; R/LPG = Right/Left Postcentral Gyrus; LPGMS = Left Postcentral Gyrus Medial Segment; R/LPreG = Right/Left Precentral Gyrus; R/LSFGMS = Right/Left Superior Frontal Gyrus Medial Segment; LSOG = Left Superior Occipital Gyrus;

Correlations between RME and diffusion metrics											
	FA			**ADC**			**ODI**			**NDI**	
ROI	**r**	**p_{UNC}**	**ROI**	**r**	**p_{UNC}**	**ROI**	**r**	**p_{UNC}**	**ROI**	**r**	**p_{UNC}**
LAA	-0.559	0.0158	**LAIns***	-0.735*	0.0005*	**LAA**	0.710	0.0010	**LACG**	-0.474	0.0468
LACG	0.515	0.0286	**LCun**	-0.488	0.0397	**LAm**	-0.521	0.0265	**LAIns***	-0.487*	0.0405*
LAIns	0.583	0.0111	**LEA**	-0.505	0.0326	**LCE**	-0.580	0.0117	**LCO***	-0.496*	0.0365*
LCE	0.550	0.0180	**LFO**	-0.568	0.0139	**LGR**	-0.574	0.0128	**LGR***	-0.496*	0.0363*
LCWM	0.491	0.0386	**LLG**	-0.504	0.0328	**LH**	-0.566	0.0144	**LMFG***	-0.615*	0.0066*
LFG	0.573	0.0130	**LMFG**	-0.472	0.0478	**RACG**	-0.644	0.0039	**LOPOFIFG***	-0.577*	0.0122*
LGR	0.521	0.0266	**LOPOFIFG**	-0.574	0.0128	**RGR**	-0.606	0.0077	**LPG***	-0.489*	0.0394*
LH	0.569	0.0137	**LPC**	-0.479	0.0444	**RMFC**	-0.520	0.0270	**LPreG***	-0.515*	0.0287*
LLG	0.555	0.0169	**LPhG**	-0.469	0.0496	**ROFG**	-0.547	0.0189	**LSFG***	-0.518*	0.0276*
LP	0.477	0.0454	**LPGMS**	-0.505	0.0324	**ROPOFIFG**	-0.470	0.0491	**LSG***	-0.536*	0.0220*
LPT	0.542	0.0201	**LPreG**	-0.548	0.0185	**RPOrG**	-0.510	0.0307	**LSPL***	-0.510*	0.0306*
LPhG	0.511	0.0301	**LPP**	-0.499	0.0348	**RSA**	-0.498	0.0354	**LTmP**	-0.471	0.0483
LPreG	0.656	0.0031	**LSMC**	-0.491	0.0384	**RTmP**	-0.525	0.0255	**RAIns***	-0.492*	0.0381*
RACG	0.548	0.0187	**LSPL**	-0.471	0.0486				**RCO***	-0.584*	0.0110*
RCE	0.533	0.0229	**LTmP**	-0.546	0.0192				**RGR***	-0.571*	0.0133*
RCWM	0.478	0.0449	**RAIns**	-0.506	0.0323				**RMFC***	-0.523*	0.0260*
RILV	0.501	0.0344	**RCO**	-0.603	0.0081				**RMFG***	-0.590*	0.0100*
RLG	0.537	0.0216	**RFG**	-0.530	0.0236				**ROPOFIFG***	-0.538*	0.0213*
RMCG	0.583	0.0112	**RLG**	-0.581	0.0114				**RPG***	-0.697*	0.0013*
RMFG	0.472	0.0481	**RMFG**	-0.492	0.0383				**RPIns***	-0.495*	0.0368*
ROFG	0.490	0.0389	**ROPOFIFG**	-0.486	0.0410				**RPO***	-0.582*	0.0112*
RPhG	0.496	0.0365	**RPG**	-0.543	0.0200				**RPreG***	-0.613*	0.0069*
CVLIV	0.581	0.0114	**RPhG***	-0.678*	0.0020*				**RSA***	-0.562*	0.0152*
CVLVIIIX	0.543	0.0199	**RPIns**	-0.633	0.0048				**RSFG***	-0.553*	0.0173*
			RPO	-0.535	0.0222				**RSMC***	-0.494*	0.0373*
			RPreG	-0.516	0.0285				**RSG**	-0.475	0.0463
			RSTG	-0.475	0.0462				**RSPL***	-0.537*	0.0216*
			CVLVIVII	-0.598	0.0087				**RTPOFTIFG***	-0.632*	0.0049*
			CSF	-0.613	0.0068				**CSF***	-0.490*	0.0389*

Table 19 Statistics for the correlations between RME and diffusion metrics (FA, ADC, ODI and NDI). The table only shows statistically significant correlations for uncorrected p-values (p_{UNC}<0.05). Asterisks represent ROIs where the correlation is statistically significant for FDR-corrected p-values (* p<0.05). In each column, the maximum (negative and/or positive) correlation and its corresponding p-value are the ones underlined. LAA = Left Accumbens Area; R/LACG = Right/Left Anterior Cingulate Gyrus; R/LAIns = Right/Left Anterior Insula; R/LCE = Right/Left Cerebellum Exterior; R/LCWM = Right/Left Cerebral White Matter; R/LFG = Right/Left Fusiform Gyrus; R/LGR = Right/Left Gyrus Rectus; LH = Left Hippocampus; R/LLG = Right/Left Lingual Gyrus; LP = Left Pallidum; LPT = Left Planum Temporale; R/LPhG = Right/Left Parahippocampal Gyrus; R/LPreG = Right/Left Precentral Gyrus; RILV = Right Inf Lat Vent; RMCG = Right Middle Cingulate Gyrus; R/LMFG = Right/Left Middle Frontal Gyrus; ROFG = Right Occipital Fusiform Gyrus; CVLIV = Cerebellar Vermal Lobules I-V; CVLVIIIX = Cerebellar Vermal Lobules VIII-X; LCun = Left Cuneus; LEA = Left Entorhinal Area; LFO = Left Frontal Operculum; R/LOPOFIFG = Right/Left Opercular part of the Inferior Frontal Gyrus; LPC = Left Precuneus; LPP = Left Planum Polare; R/LSMC = Right/Left Supplementary Motor Cortex; R/LSPL = Right/Left Superior Parietal Lobule; R/LTmP = Right/Left Temporal Pole; R/LCO = Right/Left Central Operculum; R/LPG = Right/Left Postcentral Gyrus; RPIns = Right Posterior Insula; RPO = Right Parietal Operculum; RSTG = Right Superior Temporal Gyrus; CVLVIVII = Cerebellar Vermal Lobules VI-VII; CSF = Cerebrospinal Fluid; LAm = Left Amygdala; RMFC = Right Medial Frontal Cortex; RPOrG = Right Posterior Orbital Gyrus; RSA = Right Subcallosal Area; R/LSFG = Right/Left Superior Frontal Gyrus; R/LSG = Right/Left Supramarginal Gyrus; RTPOFTIFG = Right Triangular part of the Inferior Frontal Gyrus.